Master Thesis

AE4020

P. Madabhushi

Thermal energy storage in metal-organic framework materials for climate control of Martian buildings
AE4020

TU Delft

Master Thesis

AE4020

by

P. Madabhushi

Student number: 4542894
Thesis committee: Prof. dr. S. Turteltaub, TU Delft, supervisor

TU Delft

Preface

This thesis has really give me the opportunity to take my first steps into the field of sustainable energy solutions. Thanks to my parents for giving me the opportunity and support to delve into a Master's such as this. Yes Aditi, thank you too for your support. Special thanks to Sergio Turteltaub, for being a supervisor during a rather difficult time of my thesis and for taking special efforts to guide me through the demanding process of taking on a novel topic alone.

P. Madabhushi
Delft, January 2023

Abstract

The goal of the thesis is to create a passive-working thermal battery using materials currently available to humans. The thermal management solution must thrive in the extreme Martian environment and must provide heating (and cooling if necessary) to the Martian buildings using no other forms of fuels or control. The first step involved choosing thermochemical storage materials over sensible heat storage and latent heat storage materials; thermochemical storage materials have high reaction enthalpies and relatively low densities. The thermochemical storage materials best suited to Martian applications tended to use the adsorption reaction mechanism, a reversible chemical reaction, that is extremely stable at all points along the reaction process. Adsorption is the process of chemically binding a fluid (CO_2 being abundant in Mars) to the internal surface of the material. The binding process is an exothermic chemical reaction that is passed onto the fluid or the material via conduction. The reverse reaction is endothermic, which removes the bonded CO_2 from the material.

A model was made in ABAQUS to simulate the speed of adsorption in the three thermochemical storage materials chosen (MOF-5, Zeolite-5A, and UiO-66), and to determine the feasibility of the material for the overall ambitious Martian thermal management purpose. Two separate simulations were created in ABAQUS, heat conduction and mass diffusion, to simulate the thermal output of the material and the mass transfer process during the chemical reactions. The challenge was to couple the simulations such that they worked in a staggered approach and simulate in a parallel manner. DFLUX subroutines were used to modify the internal governing equations (heat conduction and mass diffusion equations) while the UEXTERNALDB subroutines were used to transfer the data between the simulations seamlessly.

The model was then used, with the three chosen materials, to simulate six geometry permutations of Martian building walls: circular, square, circular with slots, square with slots, insulated circular with slots, and insulated square with slots. The internal size of the Martian buildings was approximately $19m^2$, while the wall material area was approximately $58m^2$. The circular and square permutations showed wasted material and heat, resulting in heat being lost by the room. The slot iterations gave over six hours of thermal heating capacity to the Martian building; over the full course of the night, the room would still see a net loss of heat to the environment, but the material is able to provide thermal management for over six hours passively. The insulation played no role in the feasibility of the material. Over a 24 hour cycle, the design can be the sole temperature-control solution for the Martian building for up to 15 hours; when compared to conventional concrete homes, the design minimises up to 97% of the energy otherwise needed to heat the building,

Contents

Nomenclature

List of symbols

Symbol	Definition	Unit
A_s	Specific surface area	m^2/grain
c	Concentration	-
c_p	Specific heat capacity	J/(kg K)
$c_{p,l}$	Mean specific heat of liquid phase	J/(kg K)
$c_{p,s}$	Mean specific heat of solid matrix	J/(kg K)
ρ	Density	kg/m^3
ρ_b	Bulk density	grains/cm^3
f	Melt fraction	-
F_t	Textural factor	-
$h_{reaction}$	Reaction enthalpy	J/kg
k	Permeability	-
L	Loading capacity	-
m	Mass	kg
m_{el}	Element mass	kg
$m_{sinkable}$	CO_2 that can sink in the material	kg
m_{sunk}	CO_2 reacted with the material	kg
n	Mass fraction	-
p*	Partial pressure	Pa
phi	Porosity	-
q	Heat flux	W/m^2
Q	Thermal energy	J
Q_s	Sensible heat energy	J
R	Rate of reaction	1/s
S	Sink term	(1/s) or J/s
t_i	Initial temperature	K
t_{inc}	Time increment size	s
t_m	Melting temperature	K
t_f	Final temperature	K
T	Temperature	K
U	Internal energy	J
V	Volume	m^3
V_{el}	Element volume	m^2
X	Sorbate loading	kg

List of abbreviations

Abbreviations	Definition
CAD	Computer-aided design
FEA	Finite element analysis
FEM	Finite element method
HC	Heat conduction
HPC	High performance computing
LHS	Latent heat storage
MD	Mass diffusion
MOF	Metal-organic framework material
PCM	Phase-change material
SHS	Sensible heat stoage
TCM	Thermochemical storage material
TES	Thermal energy storage

List of Figures

List of Tables

1 Introduction

Much like the universe, the human race is dependent on energy, making it a valuable resource. Energy scarcity is not just a future possibility on Earth, but a likely possibility in the near future during inter-planetary travel/colonisation. The storage and distribution of energy, for example thermal energy, is therefore an excellent solution towards combating the issues of energy shortage. Thermal energy storage is a material-based storage method that stores energy in unconventional ways. Conventional ”sustainable” storage methods (i.e. batteries and flywheels) are expensive to manufacture, and difficult to transport in bulk. Thermal energy storage materials use intrinsic material properties to store the energy, in the form of thermal energy, for later use. While efforts are being made to make batteries more efficient and environmentally-friendly, material constraints make it impossible to solve the global energy demand solely with current battery technology. It is for this reason, that diversifying the types of energy (and energy storage) are so important. Thermal energy storage is a valuable feature of space travel and sustainable living. The possibility of passively controlling internal environments, without the use of conventional fuels, is a worthy ambition to have, in order to colonise/inhabit Mars to some extent.

Thermal energy storage systems store energy, in the form of heat exchange, for long periods of time. They are of great interest because of their compatibility with the global vision of renewable energy technologies and sustainable energy. Thermal energy storage technologies can be categorised into three factions: sensible heat storage, latent heat storage, and thermochemical energy storage. Sensible heat storage uses the specific heat capacity of any material to store thermal energy, through changes in medium temperature. Latent heat storage describes phase change materials, which store thermal energy at a constant medium temperature; by changing between phases of matter or crystalline phases. Chemical & thermochemical storage materials uses reversible physio-chemical reactions to store the thermal energy. The exothermic/endothermic reversible reactions store heat in the form of bonds. Adsorption is a form of thermochemical storage, which involves binding a fluid to the surface of a material, in the form of a thin film. The binding process in exothermic, while the debinding process is endothermic. Thermochemical storage materials traditionally have much higher thermal energy storage capacity and and storage longevity, out of the three thermal energy storage factions; nevertheless, this thesis studies the advantages of thermochemical storage materials. With future space applications, optimising thermal energy storage materials can promote the use of thermal energy storage for large-/industrial-scale applications.

Thermochemical storage materials, specifically metal-organic framework materials, were deemed to be appropriate for the task of Martian building climate control due to their high thermal density and relative low mass density. This makes it easier to work with and to transport across planets. Using the materials as a thermal battery requires the development of a chemical reaction model, the core purpose of this thesis. The chemical reaction model would aim to determine the amount of reactants that can be adsorbed, and the heat emanated from the material as a result. The goal is to counter the heat lost by Martian building to the cold ambient environment.

The layout of the thesis can be divided into three portions: description of thermal energy storage materials, the minutia behind the model (simulation method, governing equations, software, coupling meth-

ods), and the results (calibration process, verification, material sensitivity, geometric sensitivity, and next steps).

2

Thermal energy storage

Mars' unforgiving climate among the primary challenges humankind faces in the quest for inter-planetary colonisation. At the equator, the temperatures range from 20°C to -73°C. These extreme changes in temperature makes heating a vital necessity, if humans are to live on Mars. Current heating methods are energy intensive and require a fuel to burn at some stage of the heating process. This proves to be problematic, as current research indicates that no fuels have been found on Mars; the very propellant used for rockets to-and-from Mars will need Earthly fuel stored on-board. This means that a significant amount of future rocket payloads would have to include fuel for heating on Mars. Any way to limit the amount of fuel needed would save billions of Euros in spending, make Mars-bound rocket launches more efficient, and move the Martian colony closer to truly independent living.

Thermal energy storage (TES) materials can aid in the energy independence of Martian colonies. TES materials have the ability to accumulate thermal energy like a thermal battery, such that it can be a heat source for later use. In many cases, the TES material can be used a negative heat sink for cooling applications. Current uses of TES systems act in tandem with other heat exchange applications to enhance their performance (e.g. power plants, industrial processes, climate control). For such industrial applications, "TES systems can help balance energy demand and supply on a daily, weekly, and even seasonal basis" [1]. There are three main types of TES materials: sensible heat storage (SHS), latent heat storage (LHS), and chemical & thermochemical energy.

2.1. Types of TES materials

Sensible heat storage uses a material/medium's specific heat capacity to store energy. The medium is simply heated to raise its temperature; water, rocks, wood, metals, and salts are all good examples of SHS materials [2]. The thermal energy stored by the medium is proportional to the temperature change of the medium, and can be quantified using the specific heat equation seen in Equation 2.1 below.

$$Q = mc_p\Delta T \tag{2.1}$$

Latent heat storage systems operate at a medium's phase-change state to store energy at a constant temperature. The medium is stored at a constant temperature such that the ambient/environmental temperatures do not affect the heat store capacity. These phase-change materials (phase-change material) often use the solid-liquid phase changes. The capacity of heat storage in phase-change materials depend on two material properties: mass and phase-change enthalpy. Water is a popular choice of phase-change materials, with other popular alternatives being salts, metals, and organic compounds. Cabeza mentions that phase-change materials must be uniquely selected to prevent adverse effects such as: corrosion, phase separation, subcooling, low heat conductivity, and long-term instability [2]. Another type of phase-change materials are solid-solid phase-change materials, that use different crystal structures to store energy. Unlike liquid-gas and liquid-solid phase-change materials, that significant changes in material volume, solid-solid phase-change materials often have volume changes of less than 10% [1].

Thermochemical energy storage materials (TCM) use reversible chemical reactions, instead of phase changes or specific heat, to store thermal energy. The reactions in TCMs are often seen as far more effective heat storage options, when compared to SHS materials or phase-change materials. This higher performance is due to increased storage capacity, adaptable storage duration, efficiency chemical reaction and thermal conductivity, and customised charging/discharging rates. Like most reversible reactions, the chemical product must be stored independently to eliminate the effect of equilibrium on the material. This is particularly advantageous for extended storage duration (e.g. seasonal storage).

Sorption processes are a type of chemical reaction that combine chemical reaction kinetics with material-mechanical optimisation. As mentioned before in the literature study, adsorption involves binding a fluid to the inner surface area of porous, which is a process that dispels thermal energy. Heat is needed for the reversed reaction of removing the fluid, through a process called desorption. A sorption system uses a heat exchanger to transfer thermal energy into or out of the closed system.

The most common type of sorption materials are the physiosorption materials like zeolites and silicagel, with metal-organic framework materials making headway in the TES community for their 'ultra-porous' characteristics. Further details on metal-organic framework materials will be discussed later on in section 2.4.

Table 2.1: A comparison between the three main TES methods [1]

TABLE 4.1 Typical Parameters of TES Systems

TES System	Capacity (kWh/t)	Power (MW)	Efficiency (%)	Storage Period	Cost (€/kWh)
Sensible (hot water)	10–50	0.001–10	50–90	days/ months	0.1–10
PCM	50–150	0.001–1	75–90	hours/ months	10–50
Chemical reactions	120–250	0.01–1	75–100	hours/ days	8–100

Table 2.2: A full comparison between the TES materials for SHS, phase-change material, and TCM [2].

Type of storage technology	Material	Energy stored (MJ/m^3)	Energy stored (kJ/kg)	Comments
Sensible heat	Granite	50	17	ΔT = 20°C
	Water	84	84	ΔT = 20°C
Latent heat	Water	306	330	$T_{melting}$ = 0°C
	Paraffins	180	200	$T_{melting}$ = 5–130°C
	Salt hydrates	300	200	$T_{melting}$ = 5–130°C
	Salt	600–1,500	300–700	$T_{melting}$ = 300–800°C
Chemical reactions	H_2 gas (oxidation)	11	120,000	300 K, 1 bar
	H_2 gas (oxidation)	2,160	120,000	300 K, 200 bar
	H_2 liquid (oxidation)	8,400	120,000	20 K, 1 bar
	Fossil gas	32	–	300 K, 1 bar
	Gasoline	33,000	43,200	–
Electrical storage	Zn/Mn oxide battery	–	180	–
	Pb battery	–	70–180	–

Table 2.1 above, found in Sarbu's book [1] shows some real-world parameters that are used to assess the feasibility of TES materials. Depending on the specific case that the TES medium is being designed for, the importance of the parameters are interchangeable. Nevertheless, most systems aim to have the lowest cost and the highest capacity for any given situation. A larger version of this table can be seen in Cabeza's bookTable 2.2. Both figures confirm that (thermo-)chemical storage vastly outperforms SHS and LHS; thermochemical storage materials have long storage durations, high

efficiency of storage, high transfer power, and high specific & volumetric capacity, and high costs. These advantages and disadvantages are even more relevant when one considers their application as a heat storage solution on Mars. Latent heat storage materials are also a potential solution to the Mars heat storage problem and must therefore continue to be investigated. The subsequent sections in this chapter give further detail into the realms of LHS and TCMs, paving way for a choice of one type of material to be used for the Martian application.

2.2. Latent heat storage

Latent heat storage stores thermal energy at a constant temperature, with phase-change materials (PCMs) being the most popular type of latent heat storage media. The basic principle behind phase-change materials can be explained using Equation 2.2 and Equation 2.3, taken from Equation 4.11 and Equation 4.12 from Sarbu's book [1].

$$Q_{\mathrm{s}} = \int_{t_{\mathrm{i}}}^{t_{\mathrm{m}}} mc_{\mathrm{p,s}}\mathrm{d}t + mf\Delta q + \int_{t_{\mathrm{m}}}^{t_{\mathrm{f}}} mc_{\mathrm{p,l}}\mathrm{d}t \tag{2.2}$$

$$Q_{\mathrm{s}} = m\left[c_{\mathrm{p,s}}\left(t_{\mathrm{m}} - t_{\mathrm{i}}\right) + f\Delta q + c_{\mathrm{p,l}}\left(t_{\mathrm{f}} - t_{\mathrm{m}}\right)\right] \tag{2.3}$$

This equations has three components; the two SHS equations for each phase, and the latent heat component. The variable t_m is the melting temperature, m is the mass of the entire PCM specimen, c_{ps} is the mean specific heat capacity of the solid matrix phase between the temperatures t_m and t_i, c_{pl} is the mean specific heat capacity of the liquid phase between the temperatures t_m and t_f, f is the melt fraction, and Δq is the latent heat of fusion.

There are one of three phase changes available to a phase-change material: solid-solid, solid-liquid, and liquid-gas. For the purposes of heat storage, specifically on Mars, the key criteria is the reversible nature of the phase-change material's thermal cycles. During the heat storing process, the temperature of the material initially increases relative to the thermal energy applied to it, identical to a sensible heat storage medium. At the point of phase change, the temperature of the phase-change material stays constant despite the further retention of thermal energy.

Solid-solid phase change pertains to the transitioning between varying crystallisation forms and crystal structures. It has the lowest latent heat capacity out of the three phase change processes, yet it is advantageous for its compactness and leak-proof characteristics at elevated temperatures.

Liquid-gas phase-change materials have very high latent heat capacity, but suffer from engineering and practical issues when used in real-world applications, due to their large fluctuations in volume.

Solid-liquid phase-change materials utilise the freezing/melting process to store thermal energy. The change in volume during this phase change is approximately only 10% [3]. Despite having a lower latent heat capacity, when compared to liquid-gas phase-change materials, the smaller volume variations make them a more attractive solution to thermal energy storage systems. Figure 2.1 shows the classification method of categorising phase-change materials.Figure 2.1a sorts the phase-change material processes into material categories, specifically organic, inorganic, and eutectic phase-change materials. Figure 2.1b contains the overall sorting elements from Figure 2.1a, but includes the phase-transition types for each of the categories materials.

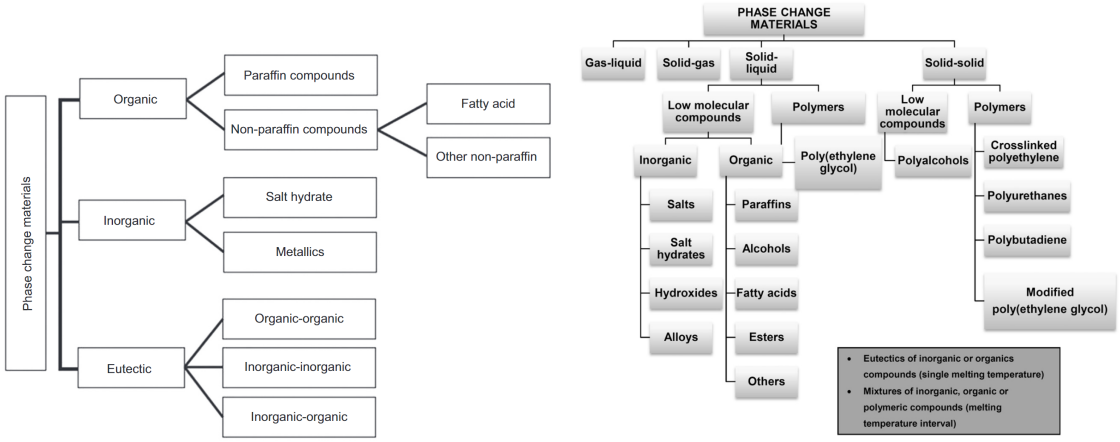

(a) Simplified phase-change material categories [1].

(b) Full classification of phase-change material categories [3].

Figure 2.1: Classification of phase-change material types.

2.2.1. Solid-solid phase-change materials

Solid-solid phase-change materials that currently exist are polyalcohols or polymers. Polyalcohols consist of compounds such as glycerine, neopentylglycol, and 2-Amino-2-methyl-1,3-propanediol. Polyalcohols tend to be heterogeneous at lower temperatures, yet they have an face-centred cubic crystalline structure that can ”absorb the hydrogen bond energy when the temperature rises to the solid-solid phase transition temperature” [3]. This process is a first-order phase transition (solely latent heat), where changes the volume of the phase-change material slightly, and does not cause phase segregation. However, ageing of the polyalcohol phase-change materials due to dehydration, greatly diminishes the thermal properties. Table 2.3 shows a comparison of some well-known solid-solid phase-changing polyalcohols used for thermal energy storage. The table was taken from Table 10 from Pielichowska's journal article [3]. Note that polyalcohols tend to have low thermal conductivity, which can be improved by using them in composites (along with multi-walled carbon nanotubes) [4].

Table 2.3: A comparison of common polyalcohols used for solid-solid phase-changing TES materials [3].

PCM	Phase transition temperature (°C)	Heat of phase transition (J/g)
Polyhydroxy alcohols		
Glycerine	18.2	
Pentaerythritol	185–187	289.0–339.5
Pentaglycerine	82	172.58
Neopentylglycol	42–44	110.4–119.1
tris[Hydroxymethyl]aminomethane	132.4–134.5	285.3–295.6
2-Amino-2-methyl-1,3-propanediol		

Polymers can be used as solid-solid phase-change materials, especially with their easily modifiable chemical and physical properties; they can be tailored to a specific thermal energy storage design. At the phase transition temperature (approximately 50°C) the polyethylene glycol side chains undergo phase changes between their amorphous and (semi-) crystalline phases. Depending on the molecular weight of the side chains, the phase transition temperature can be adapted to suit the user's requirements.

2.2.2. Solid-liquid phase-change materials

Solid-liquid phase-change materials are very popular for thermal energy storage and see a range of possible materials to use in Martian applications. As seen in Table 2.2, the following materials can be used for solid-liquid phase-changing thermal energy storage applications: salts, salt hydrates, alloys, paraffins, fatty acids, and polymers. These can be split into organic, inorganic, and polymer categories. When looking at solid-liquid phase-change materials, melting temperatures and heat of fusion are the key parameters.

Inorganic solid-liquid phase-change materials

The first kind of inorganic solid-liquid phase-change materials are salt hydrates. These are (inorganic) salts that have water of crystallisation. At the transformation temperature, the inorganic salt loses or gains some of the water through the process of hydration or dehydration respectively. The hydrated salt either melts and transforms into a a dehydrated salt (lower amount of water of crystallisation) or reverts back to its anhydrous form [1]. Salt hydrates are one of the most preferred phase-change materials due to their high latent heat of fusion (per unit volume), high thermal conductivity, small variations to the volume when melted, non-corrosive characteristics, are low-cost to store, and have low levels of toxicity [5]. Table 2.4, taken from Table 2 of Pielichowska's article, shows the list of salt hydrates that have the potential to be used for TES as a phase-change material.

Table 2.4: A list of salt hydrates that have the potential to be used as a phase-change material [3].

Compound	Melting temperature (°C)	Heat of fusion (J/g)	Thermal conductivity (W/mK)		Density (solid) (10^3 kg/m^3)
			Liquid	Solid	
$LiClO_3 \cdot 3H_2O$	8	253			
$KF \cdot 4H_2O$	18.5–19	231			1.45
$Mn(NO_3)_2 \cdot 6H_2O$	25.3	125.9			
$CaCl_2 \cdot 6H_2O$	28.0–30.0	190–200	0.540	1.088	1.80
$LiNO_3 \cdot 3H_2O$	30	256			
$Na_2SO_4 \cdot 10H_2O$	34	256			
$Na_2CO_3 \cdot 10H_2O$	33	247			
$NaCH_3COO \cdot 3H_2O$	55.6–56.5	237–243			
$CaBr_2 \cdot 6H_2O$	34	115.5			2.19
$Na_2HPO_4 \cdot 12H_2O$	35–45	279.6	0.476	0.514	1.52
$Zn(NO_3)_2 \cdot 6H_2O$	36	146.9	0.464		
$Zn(NO_3)_2 \cdot 4H_2O$	45.5				
$Zn(NO_3)_2 \cdot 2H_2O$	54				
$Na_2S_2O_3 \cdot 5H_2O$	48–55	201			1.75
$Na(CH_3COO) \cdot 3H_2O$	58	226			1.45
$Cd(NO_3)_2 \cdot 4H_2O$	59.5				
$Na_2B_4O_7 \cdot 10H_2O$	68.1				
$Na_3PO_4 \cdot 12H_2O$	69.0				
$Na_2P_2O_7 \cdot 10H_2O$	70	184			
$Ba(OH)_2 \cdot 8H_2O$	78	266			
$(NH_4)Al(SO_4)_2 \cdot 12H_2O$	95	269			
$MgCl_2 \cdot 6H_2O$	117	169			
$Mg(NO_3)_2 \cdot 6H_2O$	89.3	150			

An issue with hydrated salts are the non-uniform melting of the material, due to the fact that the water obtained from the dehydration cannot dissolve the entirety of the salt; this is called incongruent melting. Incongruent melting leads to differences in densities because the undissolved salts collect at the bottom of the system/container. This sedimentation, along with phase separation, causes a reduced thermal energy storage performance and limits the full extent of the reversible reaction; reversible reactions are a key aspect of a thermal energy storage system on Mars.

Metal alloys are another type of inorganic solid-liquid phase-change materials. Alloys are used in high-temperature TES applications due to their high thermal stability, resistance to thermal fatigue cycle effects, high latent heat per unit volume, and high thermal conductivity. However, the high density (i.e. low specific latent heat) deters its usage for a lot of applications, such as space exploration.

Organic solid-liquid phase-change materials

Organic phase-change materials are mostly paraffins, fatty acids and alcohols. Paraffin waxes are often alkenes that release heat when crystallised. Crystallisation of paraffins occur as microscopic needles and plates; bonds form between the organic chains when cooled, thus creating needle-like and plate-like crystals that interconnect the organic chains. Organic phase-change materials do not see phase segregation when changing phases repeatedly and see very little undercooling/supercooling. The latent heat of fusion can be tuned by changing the length of the hydrocarbon chain and they have a large latent heat of fusion over a small temperature range. Paraffins are relatively safe to handle, are not corrosive, chemically inert, and are not toxic to dispose of [5]. Another key advantage to paraffins are the long melting-freezing cycle times. Some drawbacks to paraffins used in thermal energy storage systems are low thermal conductivity and flammability. They have a moderate amount of thermal energy storage density, but the low thermal conductivity demands a larger exposed surface area for the heating/cooling cycles. Additives such as conductive particles, can aid with the low thermal conductivity properties yet will reduce the thermal energy storage capacity of the paraffins [3].

Fatty acids are another type of organic phase-change materials with high latent heat of fusion characteristics, especially at lower temperatures. Not only do fatty acids outperform paraffins when it comes to latent heat of fusion, but the fully reversible meting/freezing processes do not see supercooling. Fatty acids are relatively expensive, can have a pungent smell and can be corrosive. Like paraffins, increasing the hydrocarbon chain length increases the melting point and latent heat of fusion, and the degree of crystallinity. Table 2.5 was taken from Table 4 of Sharma's article, and it list the fatty acids that have the potential to be used as a phase-change material. For low temperature applications, acetic acid and polyethylene glycol (PEG) are promising.

Table 2.5: A list of fatty acids that have the potential to be used as a phase-change material [5].

Material	Formula	Melting point (°C)	Latent heat (kJ/kg)
Acetic acid	CH_3COOH	16.7	184
Polyethylene glycol 600	$H(OC_2H_2)_n$·OH	20–25	146
Capric acid	$CH_3(CH_2)_8$·COOH	36	152
Eladic acid	$C_8H_7C_9H_{16}$·COOH	47	218
Lauric acid	$CH_3(CH_2)_{10}$·COOH	49	178
Pentadecanoic acid	$CH_3(CH_2)_{13}$·COOH	52.5	178
Tristearin	$(C_{17}H_{35}COO)C_3H_5$	56	191
Myristic acid	$CH_3(CH_2)_{12}$·COOH	58	199
Palmatic acid	$CH_3(CH_2)_{14}$·COOH	55	163
Stearic acid	$CH_3(CH_2)_{16}$·COOH	69.4	199
Acetamide	CH_3CONH_2	81	241
Methyl fumarate	$(CHCO_2NH_3)_2$	102	242

Figure 2.2 below shows the storage capacity of common phase changing materials (phase-change materials) and thermochemical storage materials (TCMs). phase-change materials have lower capacities, and see a marginally larger material-temeprature range. Salt hydrates are the most interesting phase-change material mentioned in the figure, due to its relatively high capacity (for phase-change materials) at low temperatures. The challenges of phase-change materials are clearly the storage capacity, which is critical if it is to be used for Martian thermal energy storage systems.

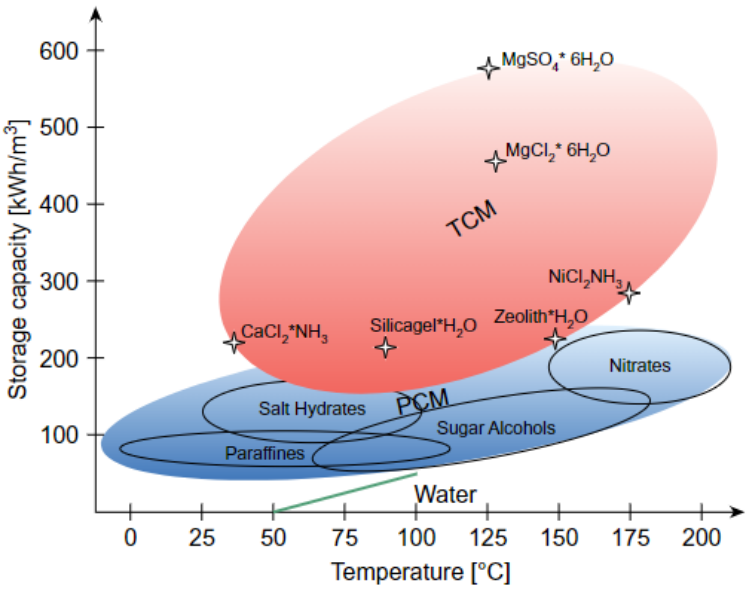

Figure 2.2: Ashby plot of TES materials

2.3. Types of (thermo-)chemical energy storage

Thermochemical materials store thermal energy through a reversible chemical reaction. Thermochemical energy storage can be split into two categories: chemical storage and thermochemical storage. This can be seen in Figure 2.3 shows the thermal energy storage material classifications available at the moment.

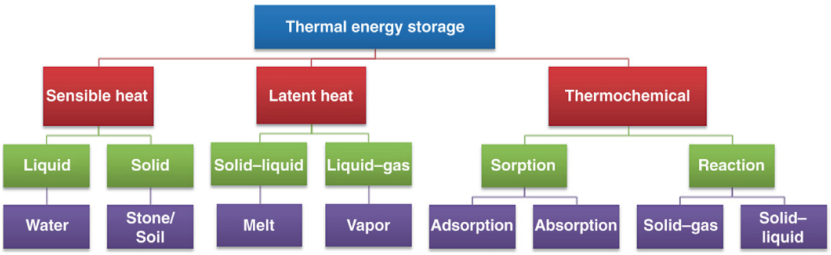

Figure 2.3: Flowchart representation of thermal energy storage categories [6].

Any chemical reaction is either exothermic (reduction of enthalpy during the reaction) or endothermic (increase of enthalpy during the reaction). Thermochemical materials are reversible, therefore the backward reaction is always the opposite of the forward reaction, when it comes down to chemical reactions. During the charging period, where heat must be stored by the material, the reaction must be endothermic. Atomic bond breakage requires thermal energy. This implies that the endothermic charging process often reverts a chemical product back into reactants. These reactants can be stored individually until there is a need for discharging. The storage of the reactants are not immune to thermal losses, but they are considered negligible compared to the reaction enthalpy being stored. Chemical storage can be in the following forms: electrochemical, photochemical, and chemisorption.

Table 2.6: A list of chemical reactions that can be used for TES [1].

Reaction		Temperature (°C)	Energy Density (kJ/kg)
Methane steam reforming	$CH_4 + H_2O = CO + 3H_2$	480–1195	6053
Ammonia dissociation	$2NH_3 = N_2 + 3H_2$	400–500	3940
Thermal dehydrogenation of metal hydrides	$MgH_2 = Mg + H_2$	200–500	3079 (heat) 9000 (H_2)
Dehydration of metal hydroxides	$CA(OH)_2 = CAO + H_2O$	402–572	1415
Catalytic dissociation	$SO_3 = SO_2 + {}^1/_2\ O_2$	520–960	1235

Table 2.6 shows a few of the prominent chemical reactions used for thermal energy storage solutions. The reactions in Table 2.6 are solid-gas reactions, which occur at elevated temperatures. Another example of chemical reactions is the thermal decomposition seen in metal oxides. For example, potassium superoxideoxide undergoes thermal decomposition in Equation 2.4 to produce potassium oxide and oxygen gas. The disadvantage of this process is that oxygen is scarce on Mars. For the reverse reaction, simply heat and exposure to air will trigger the reaction.

$$4KO_2 \leftrightarrow 2\ K_2O + 3O_2 \tag{2.4}$$

An article written by *Fuji et al.* investigated the thermal decomposition of calcium hydroxide into calcium oxide and water [7]. The calcium oxide is stored in a container without the presence of water, and the reaction takes place at elevated temperatures as well. Once again, the scarcity of water on Mars makes this solution infeasible.

In addition to thermal decomposition, photochemical decomposition is an effective method to store energy. Nitrosyl chloride (NOCl) undergoes photochemical decomposition, in the presence of photons, to produce nitric oxide (NO) and chlorine gas (Cl_2) [1]. These products can be stored separately, then combined again to derive the photon energy from the initial reaction.

In general, chemical storage can be used in higher temperature applications, when compared to thermochemical storage applications (i.e. sorption processes). Chemical storage has its benefits for its

wide range of reaction mechanisms, as well as having high energy storage density. Chemical storage does need independent storage facilities for the separated reactants/products, in order to fully utilise the long-term storage advantages. The products tend to be in a liquid and/or gaseous state, which makes storage and containment a potential issue for certain applications. Example of such applications where containment can be an issue are: water-scarce climates, highly reactive reactants, and thermal ageing. Water is a reactant for numerous chemical storage systems, which has to be kept in sealed container in order to prevent evaporation losses to the environment. Highly reactive reactants could react with the ambient environment, but could also react the inner lining of the containment unit. Gas-proof sealing and wall coatings can help prevent the unwanted reactions. Thermal ageing can involve shifting the equilibrium in a chemical reaction, to favour the decomposition of the reactants into their base elements/compounds. Many systems require constant pressure and temperature conditions to be present during the storage process.

2.4. Thermochemical storage

Thermochemical storage is a broad term used to describe sorption processes. As seen in Figure 2.3, sorption processes can be split into adsorption and absorption mechanisms. In general, adsorption refers to binding a gas/vapour to a substrate's surface. The gas/vapour is denoted as the sorbate, while the substrate is referred to as the sorbent. Furthermore, the sorbent can be in either a solid or liquid form. Similarly, absorption involves capturing the sorbate within the sorbent. Sorption utilises both thermochemical and thermophysical phenomenon [8].

Adsorption is primarily a gas-liquid or gas-solid surface interaction, hence surface phenomenon play the primary role in the binding process. If the surface binding occurs with van der Waals forces, the interaction is referred to as physisorption (physical adsorption); surface binding due to valency forces are referred to as chemisorption (chemical adsorption). The latter tends to storage larger amounts of thermal energy than the former. Thermochemical storage methods are extremely desirable due to their high energy storage density. According to *Kalaiselvam et al.*, thermochemical storage has an energy storage density of 1000 MJ/m^3, while SHS and LHS have thermal energy storage densities of 100 MJ/m^3 and 300-500 MJ/m^3 respectively [8]. Thus, thermochemical storage requires a tenth of the volume needed for SHS systems, and less than half of the volume needed for LHS systems. They continue to mention that thermochemical storage materials not only have high thermal energy storage densities, but they can also provide a large increase in temperature and the possibility of long-term storage in an ambient environment without the undesirable effect of self-discharge. Sorption can also be used with a secondary purpose of being a humidity controller.

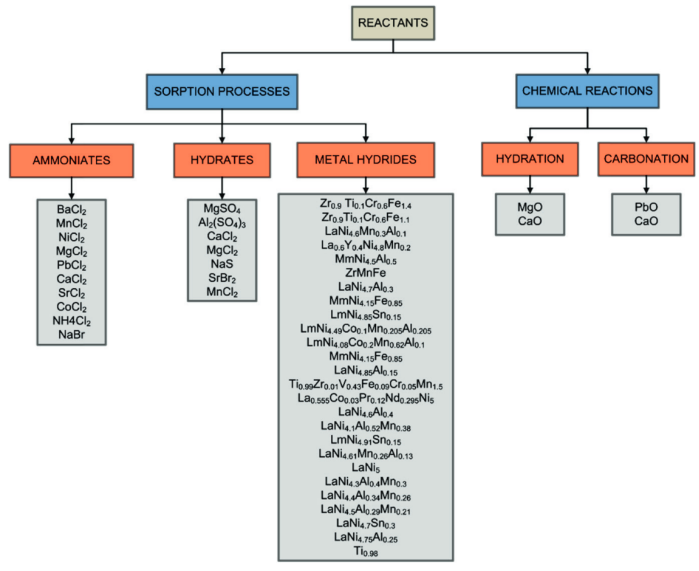

Figure 2.4: A series of tested materials used as TCMs in Kalaiselvam's article [8].

The fundamental principle of sorption involves binding a sorbate (e.g. water vapour) to a sorbent. During the binding process, thermal energy is released, due to bonds being formed between the sorbent and the sorbate. Providing heat energy would unbind the sorbate from the sorbent. Kalaiselvam explains that "the purpose of the sorption material is that it facilitates a shift from the vapor-liquid phase equilibrium of pure working fluid to the other vapor-condensed phase equilibrium of the same working fluid, but in the presence of the sorption material" [8]. A visual depiction of the sorption process can be seen in Figure 2.5. Adsorption is considered a phase transfer process, for which the sorbent offers and energy-rich active site for the sorbate [6]. The adsorption process reduces the energy level of the energy-rich active site and makes it thermodynamically more stable with the release of energy.

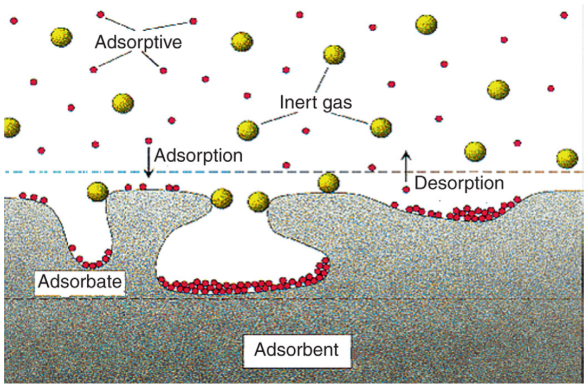

Figure 2.5: A visual depiction of the reversible sorption process using a solid sorbent and a gaseous sorbate [6].

The reversible sorption mechanism is dictated by the equilibrium process. The amount of sorbate adsorbed by the sorbent, as a fraction of the overall sorbent mass is called the loading *X*. Equation 2.5 shows that the loading is a function of temperature, in the form of partial pressure of the gaseous sorbate (p^*). Usually, the loading is characterised by evaluating it as a function of the partial pressure, in isothermal conditions.

$$X = f\,(p^*)_T \tag{2.5}$$

For isothermal adsorption conditions, the adsorbed amount of the gaseous phase increases as the pressure of the gas increases. Likewise, a higher temperature lowers the equilibrium at a constant pressure, thereby allowing a lesser amount of adsorbed gas. These key characteristics allow sorption to be used as TES as a thermochemical storage mechanism. As seen in Figure 2.6, the desorption process (discharge/exothermic process) benefits from lower temperatures and higher partial pressure. Likewise, the desorption (charging/endothermic process) needs higher temperatures and low partial pressures.

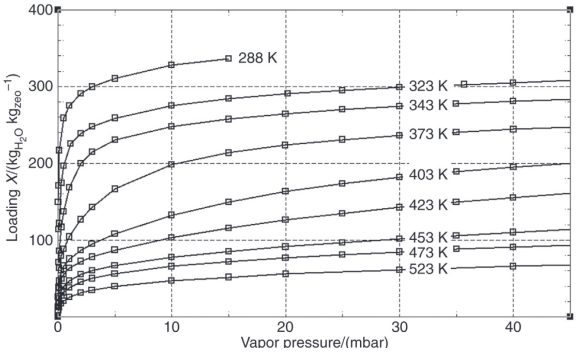

Figure 2.6: Loading values for isothermal adsorption using zeolite at varying vapour pressures and temperatures [6].

In addition to temperature and partial pressure, enthalpy plays a major role in sorption processes. *Kerskes et al.* defines the enthalpy of adsorption as the energy difference between the adsorption

and desorption processes [6]. The adsorption enthalpy is the heat dispelled by the system due to gas condensation and bonding forces (i.e. van der Waals forces or valence/electrostatic forces). The enthalpy value seen is greatly affected by the sorbent properties; zoelites, a type of porous aluminosilicate material, have high bonding forces and therefore have higher thermal energy storage densities. Note that for practical applications, adsorption does not occur uniformly. The surface energy of certain activated zones can create inhomogeneity in the adsorption process. Since adsorption first takes place at energy-rich active regions, and are the last regions to desorb, it is prudent to ensure the entirety of the material undergoes the full desorption process. To achieve full desorption, high temperatures and extremely low gaseous pressures are often needed. The adsorption enthalpy is related to the loading X, which in turn is a function of partial pressure and temperature. This gives an indication as to the manner in which material design can take place for sorption systems.

Even within sorption systems, there are two categories: open systems and closed systems. The following paragraphs will discuss the principles behind the two categories, following with an explanation of an absorption system.

2.4.1. Open systems

An open system allows the flow of the heat transfer fluid to leave the system and expose itself to the environment. The enthalpy and entropy is released to the environment. Current applications for open systems are for climate control of buildings. The interaction with the environment is sufficient to meet the demands. Note that these systems are seasonal heat systems, which entails having extended periods of stored thermal energy before an environment-driven discharge. Self-discharging is not an issue unless the heat-transfer fluid is allowed to freely flow; open systems can isolate the sorbent from the environment and heat-transfer fluids until the charge/discharge cycle is necessary.

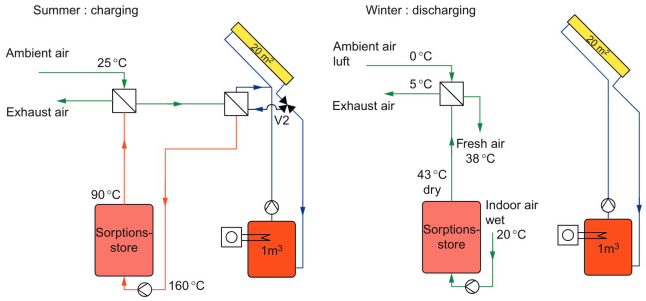

Figure 2.7: An open- sorption system that uses a zeolite and a solar array as the heat source [8].

Figure 2.7 shows an open-system used for storing heat absorbed by a solar panel (labelled yellow). During the charging process, heat from the solar panel raises the temperature of the heat-transfer fluid to approximately 160°C. This heat-transfer fluid flows through the thermochemical material (zeolite 4A) and triggers the desorption process of the water vapour phase. Upon desorption, the water remains within the thermochemical material due to the flow effects of the heat-transfer fluid. The warm heat-transfer fluid (relatively cooler than the inlet heat-transfer fluid) can be used for regular heating demands. Conversely during the discharge process, the cooler inlet heat-transfer fluid conditions trigger the exothermic adsorption process and heat the heat-transfer fluid. This can be subsequently used for the general heating demands. The reason that this is an open system is that the zeolite 4A interacts with the environment directly, in order to exchange thermal energy. The conditions of the sorption equilibrium are entirely dictated by the ambient and inlet heat-transfer fluid conditions. The zeolite 4A uses a honeycomb internal micro-structure, thus allowing a larger surface area for adsorption and a larger amount of thermal energy to be stored. Furthermore, the honeycomb-like structure reduces the pressure drop across material and aids with the rate of the reaction [8].

2.4.2. Closed systems

A closed system does not allow the heat-transfer fluid to leave the system. It is only exposed to the adsorption material. In this case, enthalpy and entropy is transferred to the environment through an intermediary system, such as a heat exchanger. The choice of sub-systems are generally the same,

with two exceptions: the heat exchanging method and a storage tank. Assuming that the sorbate is water vapour again, and the sorbent is a type of zeolite, the storage tank is equipped to contain the water after the desorption process. This can be seen in Figure 2.8.

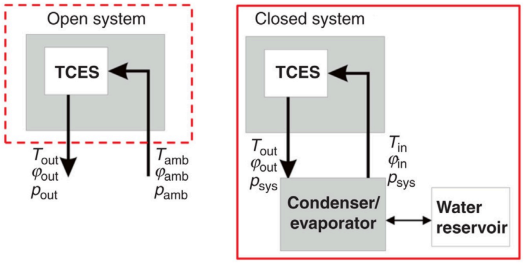

Figure 2.8: The difference between closed- and open-systems for the sorption process [6].

During the charging process (desorption/endothermic), the heat-transfer fluid (i.e. humid air) is heated to a point that will almost entirely desorb the zeolite sorbent. The thermal energy is used in the desorption process, resulting a in cooler and more humid air that leaves the sorbent. The water vapour can be separated from the air with the aid of a condenser/evaporator (which acts as a humidifier/dehumidifier). Heat is generated when the vapour is cooled to its liquid phase, which can either be used as part of an auxiliary heating element or it can be dispelled to the ambient environment. The liquid water is kept in the water reservoir. Higher desorption occurs at higher inlet temperatures for the sorbent, as well as lower condenser temperatures. The desired condenser temperature can be calculated using the dew point of the vapour at the operating pressure. For water vapour, these are standard relations; for non-conventional heat-transfer fluids, this requires a full characterisation before implementation. Finally, the zeolite sorbent is left to cool till the ambient temperature. Once it reaches the ambient temperature, there would be no further losses in the thermal energy storage.

Discharging (adsoption/exothemrmic) the thermochemical material requires an initial heating step. A low-level heating source is needed to provide the condenser/evaporator with additional heat for the evaporation of the liquid water in the reservoir. The water vapour is sent towards the thermochemical material and is adsorbed, thereby releasing thermal energy during the reaction. This heat is transferred to the heat-transfer fluid for the desired heating purposes. As the sorption cycle is fully reversible, the total heat stored during the charging phase (including the heat potentially lost in the exchanger) is equal to the heat generated during the discharging phase (including the heat needed to evaporate the water in the reservoir).

In closed systems, such as the one just mentioned, the key is to be able to extract as much thermal energy from the sorbent as possible. And while the overall conditions (i.e. temperature and partial pressure) are regulated for optimal sorption cycles, the heat released from the sorbent must be easily extractable. For this, thermal conductivity is necessary, as conduction is the primary heat transfer mechanism. However zeolite materials have low thermal conductivity characteristics (0.1-0.5 W m^{-1} K^{-1}) [6]. Therefore, an active heat exchanger is necessary to drive the heat to/away from the sorbent. *Kersekes et al.* also mentions that the limitation to the thermal power is the evaporator.

2.4.3. Absorption system

Having discussed adsorption, absorption may now be considered for thermochemical storage. Absorption is rather similar to adsorption, in the sense that the sorbate is extracted from the heat-transfer fluid in order to exchange thermal energy with the heat-transfer fluid. Consider the setup shown in Figure 2.9. In the case of this system, water is the sorbate and sodium hydroxide acts as a liquid sorbent. Adsorption is a surface phenomenon, whereas absorption is considered a bulk phenomenon.

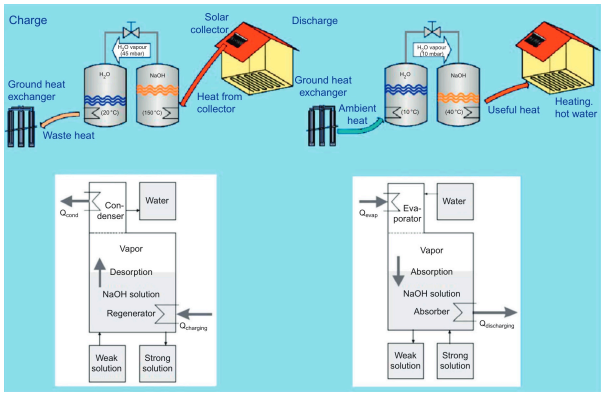

Figure 2.9: An example of an absorption system (closed-storage) used to store a solar thermal energy [8].

When heat is added to the system by the solar panels, the water separates from the sodium hydroxide (due to differences in evaporation temperatures) and is desorbed from the sodium hydroxide. The sodium hydroxide is concentrated by the end of the desorption process and can be stored independently for later use. Furthermore, the water vapour is cooled to liquid form and stored separately as well. During the discharging phase, the reversed process occurs. The two stored compounds are brought together, after a small amount of thermal energy is needed to evaporate the liquid water, and heat is released when the water is absorbed by the concentrated sodium hydroxide.

2.5. Materials for thermal energy storage systems

This chapter has introduced sensible heat storage, latent heat storage, and chemical & thermochemical storage. Common materials used for each of the storage systems were briefly mentioned in the individual sections, however this section will compile a more complete list of materials for each storage type. This section will discuss three main material types: adsorption materials and salt hydrates (i.e. latent heat storage). Adsorption materials are investigated due to their high thermal capacity, storage density, and power. They have the best characteristics for high-performance thermal energy storage applications. Salt hydrates are the also investigated because of how their relatively high thermal capacity and storage density; furthermore, they are a well-established material with simple charging/discharging processes.

2.5.1. Materials for adsorption

In general, all thermal energy storage materials aim to have the following properties:

- Substantial capacity to adsorb a sorbate, in combination with a high thermal energy captured during the adsorption process.
- Quick charge/discharge cycles to ensure immediate response to external thermal demands.
- A desporption temperature that corresponds to operating conditions.

Unlike chemical storage, where the rate of reaction plays the dominant role in the storage performance, thermochemical materials also benefit from specific surface kinetics and reactant-storage capabilities (including heat exchangers). The drawback is that there are more parameters to control and optimise; conversely, it allows the material to be tuned more specifically to the application. For example, without being constrained fully by chemical reaction kinetics, adsorption processes can even allow fast charging/discharging cycles at lower temperatures. Adsorption materials must have crevices/holes with energy-rich active regions, in order to promote the adsorption process.

Pores, seen in porous materials used for adsorption, can be categorised into three size classes, denoted by the pore diameters d: micropores (d<2nm), mesopores (2<d<50nm), and macropores (d>50nm). Conversely, the inner surface area per unit mass is highest for micropores and lowest for macropores. Materials rarely feature a single type of pore, as the three size classes have different functions. The sorbate diffuses towards the inner regions of the sorbent via the mesopores and macropores. The adsorption process, however, mostly occurs in the pores. This is because they significantly

add to the effective surface area of the material, as seen in Equation 2.6. The equation is an adaptation of the Carman–Kozeny surface area equation, where A_s is the specific surface area (m^2/grain), ρ_b is the bulk density (grains/cm^3), ϕ is the porosity, k is the permeability (mD), and F_t is the textural factor [9].

$$A_{\mathrm{s}} = 31.8\rho_{\mathrm{b}}^{-1}\left(\frac{\emptyset^3}{kF_{\mathrm{t}}}\right)^{1/2} \tag{2.6}$$

The three current most popular adsorption sorbent materials are zeolites, active carbon, and silica gel. The properties for each are shown in Table 2.7 below. Active carbon tends to have low thermal storage capacity, low reaction enthalpy, and irreversible reactions; yet active carbon is relatively inexpensive and reliable. The current uses of active carbon using the sorption process are gas purification (e.g. air purifiers) and cooling. The other two materials have better thermal capacities and reaction enthalpies, making them more attractive to as materials for the sorption process.

Table 2.7: An assessment of adorption-stroage properties of popular sorption materials [6].

Characteristic values	Active carbon	Silica gel	Zeolite
Inner surface/(m^2 g^{-1})			650–750
Mean adsorption enthalpy/(kJ $kg^{-1}H_2O$)	~2400	~2600	~3500
Specific heat capacity c_p/(kJ K^{-1} kg^{-1})	0.709	0.9–1.0	0.8–0.9
Heat conductivity/(W m^{-1} K^{-1})	1.2–1.6	0.14–0.2	0.58

The material examples given in section 2.4 have been mostly zeolites for this reason. Zeolites see a higher desorption temperature, due to the higher adsorption enthalpy (seen in Table 2.7), and faster adsorption kinetics when compared to silica gels. Furthermore, the increase in temperature that silica gel can provide, reduces with additional loading, according to *Jaehnig et al.* [10]. The optimal mass loading was found to be between 2-12%, despite the capability of the material to load up to 35% of the sorbent's mass; in short, the effective material density is lower.

Fast reaction kinetics seen in zeolite materials favours adsorption at even low sorbate concentrations. The most common zeolite types are classified using the following letters: A, X, or Y. A-type zeolites (often referred to as 4A or 5A) are relatively cheap and reliable, especially when paired with water vapour as the sorbate. X-type and Y-type zeolites have higher thermal energy storage capacity and are considered a better version to the A-type zeolites.

Materials like aluminophosphates (AlPOs) and silicoaluminophosphates (SAPOs) aim to replicate the porous crystalline structure seen in zeolites. They have lesser hydrophilic characteristics, thus allowing better adsorption at lower temperatures. This can help combine the advantages of both zeolites and silica gels, thereby allowing high adsorption enthalpy capacity and low-temperature desorption; ALPOs and SAPOs have higher sorbate uptakes compared to zeolites, as well as at lower temperatures. [6]. Currently, ALPOs and SAPOs are expensive to manufacture, excluding them from serious consideration for current existing applications.

Another such type of expensive porous materials are metal-organic framework materials (MOFs). According to *Berger*, "MOFs are organic-inorganic hybrid crystalline porous materials that consist of a regular array of positively charged metal ions surrounded by organic 'linker' molecules" [11]. The use for these materials/structures in thermal energy storage systems was first postulated by *Li et al.* in 1999 [12]. An example of one such MOF is seen in Figure 2.10 below. ZNO_4 tetrahedral molecules form organic links to create a cage-like structure. The full compound is called $Zn_4(O)(BDC)_3$, where BDC stands for benzenedicarboxylate. The yellow structure (cavity) represents a region of extremely high internal surface area. They estimate that the MOFs could see an inner surface area of at least 7800 m^2g^{-1}; a teaspoon of an MOF of this sort would have the working surface area of a football field (approximately >700m^2). MOFs have uniform pore patterns, modifiable pores, interchangeable network topology, shapes, sizes, and functional characteristics. With such large surface areas accessible, MOFs are extremely potent as a sorbent; MOF-5 is identified as a compound with excellent adsorption characteristics and hydrothermal stability [6]. Costs still remain a limitation for MOFs.

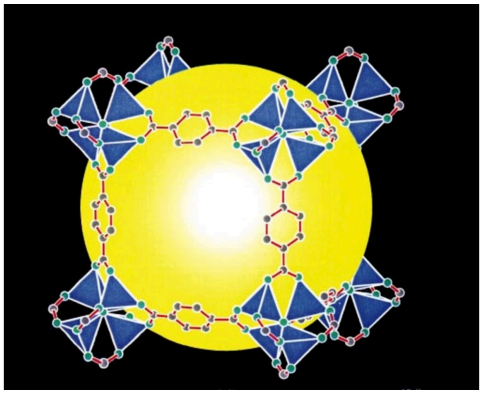

Figure 2.10: A MOF-5 framework of $Zn_4(O)(BDC)_3$ with a large cavity (yellow) in the middle [12].

2.5.2. Salt hydrates

Latent heat storage systems often use salt hydrates as phase-change materials, as seen in Table 2.4. Salt hydrates have high thermal energy storage densities, with solid-liquid reactions. Easily available salts, such as hydrated magnesium sulfate (or calcium chloride), has a high thermal energy storage capacity; it has an order of magnitude greater capacity when compared to sensible heat storage materials, but falls short to MOFs.

Salt hydrates have some specific advantages and limitations, when used as a thermal energy storage material. Salt hydration reactions are an equilibrium reaction, for which hydration becomes less efficient as more water is added to it. Consider magnesium sulfate as a salt hydrate phase-change materials. It sees better hydration at higher temperatures, for magnesium sulfate monohydrate (single mol of water), when compared to magnesium sulfate hexahydrate. Furthermore, magnesium sulfate heptahydrate (7mol of water) does not dehydrate as expected; it dissolves as an aqueous solution and melts/boils instead. This creates unwanted inter-species bonding and crystal growth, preventing the desired hydration/dehydration cycle. Therefore, *Kerskes et al.* recommend using a more thermodynamically stable form of the salt, e.g. strontium bromide.

2.6. TES conclusion

Thermal energy storage has many applications on Mars, such as (but are not limited to): climate control in buildings, heating/cooling of water, energy storage for electricity grid providers and solar farms, and temperature control in agricultural greenhouses.

Although phase-change materials are often the first choice for these sort of systems, salt hydrates, fatty acids and paraffins have high storage densities, but they need higher temperatures to operate optimally. They also are difficult to tune via geometric/mechanical modifications (e.g., porosity) as their micro- and macro-structure tends to change during the phase transitions. Porosity can be used to optimise the hydration kinetics of the anhydrous salts, but these modifications are unlikely to remain after repeated cycles. The primary driver behind the phase changes are: grains (for metals), crystallisation (for polymers), and hydration kinetics (for salts).

Thermochemical storage can be done through simple equilibrium chemical reactions, but see a lot more advantages when utilising the sorption mechanism. High thermal storage density, with numerous tunable parameters, give the opportunity to create a material for specific purposes. Zeolites and silica gels are common adsorption materials used in the thermal energy storage community, but new research into metal-organic framework materials provide exciting opportunities to maximise thermal density properties. Creating a model for the inherently nano-porous material can help take the first steps into developing the materials for Martian thermal management solutions.

3

Modelling

The previous chapters discussed the relevance of TES materials in scope of sustainable energy transition and Martian colonisation, as well as the purpose of investigating material optimisation for TES applications. This chapter elaborates on the manner in which the simulations were conducted: the simulation method, materials chosen for the design, software used, the governing equations, and implementation in ABAQUS.

3.1. Simulation method

The goal is to simulate the metal-organic framework material's sorption process, to best design the geometry for the maximisation of thermal energy storage at Martian climate conditions. To simulate the sorption mechanism, the analysis must feature three components: mass diffusion of the heat transfer fluid (sorbate), exothermic/endothermic enthalpy of reaction (local heat source/sink), and heat conduction of thermal energy through the MOF sorbent. Both mass diffusion and heat conduction analyses use Fick's law of diffusion, which is a partial differential equation that describes any diffusion. Therefore, there must be two simulations running in parallel: a mass diffusion simulation and a heat conduction simulation. Both simulations must interchange mass and heat data constantly during the simulation to determine whether the conditions for the sorption reaction has been met (i.e., concentration of the heat transfer fluid, temperature of the material and fluid, and the amount of sorbate that has already been adsorbed). For the desorption reaction (thermal charging process), heat is provided to the loaded MOF material via the hot heat transfer fluid (CO_2), to break the bonds of the CO_2 attached to the material; this cools the fluid and stores the heat in the form of an unloaded MOF material. Conversely, the adsorption reaction (thermal discharging process) uses cold CO_2 gas, which binds to the surface of the unloaded MOF bulk material; the formation of the chemical bonds are exothermic, thus releasing the heat to the CO_2 gas and heating it. When the soprtion/desorption conditions are met, the reversible chemical reaction takes place, leading to an endothermic/exothermic reaction; this will be added as a heat source/sink to the heat conduction simulation, and a mass source/sink to the mass diffusion simulation simultaneously.

3.2. Materials

The purpose of this study is to determine the optimum material and configuration for Martian applications. The chosen materials determine the intrinsic capabilities of the thermal battery, while the geometric shape helps optimise the full capacity of the material and attempts to tune it to the unforgiving Martian climate. Two types of geometries will be used in this study: a circular wall, and a conventional square/rectangular wall.

The initial materials search began with lists procured in existing scientific research journals, as seen in Table 3.1 and Table 3.2. Note that some of the materials are common in both tables, but with different uptake values. This is usually the result of different testing conditions; different temperatures, different pressure gradients, different macro-shape. It is for this reason that the promising materials had to be investigated separately to find the material characteristics at the same/similar operating conditions. These materials were chosen for the following reasons:

- Experimental data regarding material properties are readily available.

- Material properties have been corroborated by multiple sources.

- High uptake of of CO_2 as a percentage of bulk weight.

- High mass diffusivity (key for concentration gradient-driven diffusion).

- High reaction enthalpy.

Table 3.1: Another list of MOFs feasible for CO_2 adsorption [13]

MOF	CO_2 Uptake	T (°C)	P
Zn(adc) $(4,4_0\text{-bpe})_{0.5}$	130 mmol g^{-1}	−78.15	1p/p
(MIL-53)	7.5 mmol g^{-1}	30.85	20 bar
Cu(fam) $(4,40\text{-bpe})_{0.5}$	100 mL g^{-1}	−78.15	760 torr
$Ni_2(cyclam)_2(mtb)$	57 mL g^{-1}	−78.15	1 atm
MIL-53 M = Al, Cr	10 mmol g^{-1}	30.85	30 bar
(PCN-5)	210 mg g^{-1}	−78.15	760 torr
$Cu(dhbc)_2$ (4,40-bpy)	70 mL g^{-1}	24.85	0.4~8 atm
Cu(bdc) $(4,40\text{-bpy})_{0.5}$	70 mL g^{-1}	24.85	0.1~0.2 MPa
(ZIF-20)	70 mL g^{-1}	0	760 torr
$[Ni(bpe)_2$ $(N(CN)_2)]$ $(N(CN)_2)$	35 mL g^{-1}	−78.15	1p/p
Zn_2(tcom) (4,40-bpy)	5 wt%	24.85	1 bar
Cu(pyrdc)(bpp)	Differed adsorption capacity	−78.15	Different pressure
$Ni_3(BTC)_2$	3.0 mmol g^{-1}	40	1 bar
SNU-110	6.0 mmol g^{-1}	78	1 bar
1D-MOF	4.0 mmol g^{-1}	78	1 bar
2D-MOF	2.9 mmol g^{-1}	0	1 bar
A core–shell MOF	41 mmol g^{-1}	0	1 bar
NJU-Bai12	23.8 mmol g^{-1}	0	20 bar
PCN-124	9.1 mmol g^{-1}	0	1 bar
MOF-5/graphite oxide	1.1 mmol g^{-1}	25	4 bar
HCM-$Cu_3(BTC)_2$-3	2.8 mmol g^{-1}	25	1 bar
Zn doped Ni-ZIF-8	4.3 mmol g^{-1}	0	1 bar
Zn(II)-based MOFs	9.2 mmol g^{-1}	25	1 bar
MOF with PEI	4.2 mmol g^{-1}	78	0.15 bar
MIL-53 with BNH_x	4.5 mmol g^{-1}	0	1 bar
Mg-MOF-74	8.0 mmol g^{-1}	23	1 bar
UMCM-1-NH_2-MA	19.8 mmol g^{-1}	25	18 bar

Table 3.2: Another list of MOFs feasible for CO_2 adsorption [14]

Sample name	Original material	CO_2 uptake experiment parameters	Result (mmol g^{-1})
BM-900	bio-MOF-1	273 K and 1 bar	4.62
		298 K and 1 bar	3.55
KBM-700	bio-MOF-1	273 K and 1 bar	4.75
		298 K and 1 bar	3.29
MUC600	MOF-5	0 °C and 1 bar	3.55
		25 °C and 1 bar	2.44
		25 °C and 0.15 bar	0.73
MUC900	MOF-5	0 °C and 1 bar	3.71
		25 °C and 1 bar	2.31
		25 °C and 0.15 bar	0.43
AAC-2W	MIL-100(Al)	273 K and 1 bar	6.5
		298 K and 1 bar	4.8
		298 K and 0.2 bar	1.74
C800	MIL-100(Al)	273 K and 1 atm	4.1
		298 K and 1 atm	2.6
NC800	MIL-100(Al)	273 K and 1 atm	5.7
		273 K and 0.15 atm	2.3
		298 K and 1 atm	3.8
N-HPCMs-5-0.6-973	Al-based composite	273 K and 780 mmHg	2.35
		298 K and 780 mmHg	1.82
C700	ZIF-8	273 K and 1 bar	3.70
		298 K and 1 bar	2.76
C1000	ZIF-8	273 K and 1 bar	4.64
		298 K and 1 bar	3.39
C700W	ZIF-8	273 K and 1 bar	5.51
		298 K and 1 bar	3.80
NC900	ZIF-8	273 K and 1 atm	5.1
		298 K and 1 atm	3.9
AC-CB700	ZIF-8	25 °C and 1 bar	2.0
1000	ZIF-8	25 °C and 0.15 bar	0.99
		25 °C and 1 bar	3.22
		25 °C and 20 bar	10.21
C68	ZIF-68 + FA	273 K and 1 atm	4.76
C69	ZIF-69 + FA		4.54
C70	ZIF-70 + FA		5.45
C68	ZIF-68 + FA	298 K and 1 atm	4.00
C69	ZIF-69 + FA		3.86
C70	ZIF-70 + FA		4.49
CZIF8a	ZIF-68 + FA	273 K and 1 atm	4.04
CZIF68a	ZIF-69 + FA		4.49
CZIF69a	ZIF-70 + FA		4.76
Pristine MOF	MOF-5	25 °C and 0.15 bar	0.26
		25 °C and 1 bar	1.30
Carbonized MOF	**CMOF-5**	25 °C and 0.15 bar	**0.57**
		25 °C and 1 bar	**2.43**
		25 °C and 10 bar	**9.73**
		25 °C and 20 bar	**13.55**
		25 °C and 40 bar	**18.56**
		40 °C and 0.15 bar	**0.39**
		40 °C and 1 bar	**1.95**
		40 °C and 10 bar	**8.09**
		40 °C and 20 bar	**11.76**
		40 °C and 40 bar	**16.27**
		100 °C and 0.15 bar	**0.12**
		100 °C and 1 bar	**0.66**
		100 °C and 10 bar	**3.86**
		100 °C and 20 bar	**6.15**
		100 °C and 40 bar	**9.18**

The materials investigated in this thesis are: MOF-5, Zeolite-5A, and UiO-66(Zr). Zeolite is the only material among the three that is not a metal-organic framework material, but is the current benchmark, and is what the metal-organic framework materials aim to outperform. The full list of properties for each material can be seen in Table 3.3 and Table 3.4 below. Note that all three materials operate at the required Martian temperatures of 144-323K.

Table 3.3: Material properties of the three materials investigated in this thesis used in the mass diffusion simulation.

Material	Mass Density [kg/m^3]	Mass diffusivity [10^{-5} m^2/s]	CO_2 uptake [$kg_{CO_2}/kg_{material}$]
Zeolite-5A [13][15]	1161	1.50	0.30
MOF-5 [15][16]	300	1.15	0.44
UiO-66 [17][18]	1201	1.70	0.12

Table 3.4: Material properties of the three materials investigated in this thesis used in the heat conduction simulation.

Material	Thermal conductivity [W/(m K)]	Specific heat capacity [J/(kg K)]	Enthalpy of adsorption [10^6 J/kg_{CO_2}]
Zeolite-5A [19] [15]	0.10	935	1.484
MOF-5 [20][21]	0.32	730	1.020
UiO-66 [20][21]	0.11	758	0.682

The two tables detail six material characteristics deemed important for the simulation. Mass density mass diffusivity, thermal conductivity, and specific heat capacity are all required by ABAQUS for to run the individual diffusion/conduction simulations. They have to be provided as inputs in the input file. The CO_2 uptake is the amount of fluid that can be adsorbed to the material. There is a finite area of active sites for the reactions to take place, leading to a finite amount of CO_2 adsorbed to the material at any given volume. As the material density remains unchanged after the reactions have taken place, the finite volume can be interpreted as a finite mass. This parameter is usually measured in mmol/g, but for the convenience of calculations, it was used as a dimensionless parameter. A dimensionless parameter ($kg_{CO_2}/kg_{material}$) was used instead of the traditional mmol/g because most of the reaction enthalpies used mass of CO_2; to avoid the additional conversion of mmol to kg during the simulations, mass was used universally. In the mass diffusion user-subroutines, the uptake is what is used to determine whether full saturation in the material has occurred; by creating a term ”mass fraction”, a normalised value based on the uptake, the DFLUX user-subroutines changes the rate of adsorption based on how ”filled” the material is at that position in the material.

The enthalpy of adsorption is used in the heat conduction simulation to determine whether the magnitude of heat flux based on the amount of CO_2 adsorbed.

Finally, a parameter not mentioned in the tables is the maximum mobile concentration. This is the maximum amount of mobile/unreacted CO_2 that can reside in the material, much like water in a sponge. This parameter was found to be approximately 0.57 for all three materials[16]. This is because the nano-porosity of the three materials is rather similar, especially the nano-pore diameters.

3.3. Software

The sorption mechanism requires a combination of heat transfer and mass transfer simulations to accurately depict the effects of the chemical reactions. The exothermic/endothermic nature of the reactions are depicted using heat conduction methods, while the fluid propagation and surface bonding are best depicted using mass diffusion methods. Therefore, the model must feature a dual-simulated material. The simulations were done using commercial software, as supposed to Python or Matlab, for numerous reasons: built-in parallel processing, intuitive user-interface, easier CAD modelling, and simpler post-processing tools. Among the available commercial software the university had access to, ABAQUS was chosen due to its high modifiable user-subroutine integration. The subroutines allow the user to make changed to the conventional solving methods and algorithms, to best tailor the simulation experience to the user’s project.

3.4. Governing equations

This section outlines the inner workings of the ABAQUS simulation, specifically: assumptions made for the model, heat/mass diffusion equations, time discretisation, and sink/source term addition.

3.4.1. Diffusion equations

The diffusion equation can be summarised using Equation 3.1 below [22]. The adsorption of CO_2 in the material is governed by the availability of the sorbate and sorbent, i.e., the free (mobile) CO_2 and metal-organic framework material respectively. Much like Hille’s work on alumina formation, the distribution of concentration of free CO_2 is governed by the following diffusion–reaction equation[22]:

$$\frac{\partial c}{\partial t} - \nabla \cdot (D \nabla c) = -S \tag{3.1}$$

where *D* is the carbon dioxide diffusion coefficient (diffusivity) and *S* is a sink term. This sink term represents the restriction in space of mobile CO_2 due to the adsorption process. In short, the CO_2 does not diffuse further through the material once it has reacted with the bulk material. The sink term *S* can be defined using another one of *Hille et al.*'s equations. The rate of CO_2 that reacts to the surface of the MOF material (i.e.,$\partial n/\partial t$) is proportional to the product of the rate of reaction and the amount of CO_2 already reacted in that region:

$$\frac{\partial n}{\partial t} = R(1 - n) \tag{3.2}$$

for which the sink term can be defined as $S = \frac{\partial n}{\partial t}$.

3.4.2. Diffusion equations used in ABQUS

Abaqus solves the heat conduction problem using Green & Naghdi's energy balance (Equation 3.3), Fourier's law (Equation 3.4), and the Galerkin spacial discretization approach.

$$\int_V \rho \dot{U} dV = \int_S q dS + \int_V r dV \tag{3.3}$$

where V is the volume of the MOF material, S is the surface area, ρ is the density of the material, $\dot{U}$ is the time rate of the internal energy within the MOF material; q is the normal heat flux per unit surface on the external boundary, and r is the heat supplied externally into the body per unit volume. This is the uncoupled analysis ($U = U(\theta)$, for temperature θ), which means that the temperature, q and r do not affect and are not affected by mechanical stresses and strains. The equations use the same reference coordinate system as the volume and surface of the material body; the Lagrangian description is assumed.

$$\mathbf{f} = -\mathbf{k} \frac{\partial \theta}{\partial \mathbf{x}} \tag{3.4}$$

where $\mathbf{k}$ is the thermal conductivity of the material, $\mathbf{f}$ is the heat flux vector, and $\mathbf{x}$ is the spatial position vector. For this analysis, the thermal conductivity was considered to be constant and isotropic. The change of material thermal conductivity is negligible for the limited operational temperature range. MOF does conduct and diffuse in an homogeneous manner with free-flowing gas; when the fluid is forced/pumped into the material, it becomes highly inhomogeneous.

The two equations combine to create Equation 3.5, for which $\delta\theta$ is a variational field that is arbitrary in nature (i.e., it can be given any value).

$$\int_V \rho \dot{U} \delta\theta dV + \int_V \frac{\partial \delta\theta}{\partial \mathbf{x}} \cdot \mathbf{k} \cdot \frac{\partial \theta}{\partial \mathbf{x}} dV = \int_V \delta\theta r dV + \int_{S_q} \delta\theta q d \tag{3.5}$$

The temperature θ and the variational field is interpolated using the following relations by ABAQUS, where θ^N are the nodal temperatures. As seen below, the variational field is interpolated in the same way as the temperature.

$$\theta = N^N(\mathbf{x})\theta^N, \quad N = 1, 2, \ldots$$

$$\delta\theta = N^N \delta\theta^N$$

One can substitute the interpolation equations into Equation 3.5 to get the updated energy balance.

$$\delta\theta^N \left\{ \int_V N^N \rho \dot{U} dV + \int_V \frac{\partial N^N}{\partial \mathbf{x}} \cdot \mathbf{k} \cdot \frac{\partial \theta}{\partial \mathbf{x}} dV = \int_V N^N r dV + \int_{S_q} N^N q dS \right\} \tag{3.6}$$

With $\delta\theta^N$ being arbitrary, the energy balance is simplified its continuous time description.

$$\int_V N^N \rho \dot{U} dV + \int_V \frac{\partial N^N}{\partial \mathbf{x}} \cdot \mathbf{k} \cdot \frac{\partial \theta}{\partial \mathbf{x}} dV = \int_V N^N r dV + \int_{S_q} N^N q dS \tag{3.7}$$

3.4.3. Time discretisation

ABAQUS uses a backwards Euler time discretisation method seen in Equation 3.8.

$$\dot{U}_{t+\Delta t} = \frac{U_{t+\Delta t} - U_t}{\Delta t} \tag{3.8}$$

When substituted into $\rho \dot{U}$ in Equation 3.7, the energy balance equation becomes

$$\frac{1}{\Delta t} \int_V N^N \rho \left(U_{t+\Delta t} - U_t\right) dV + \int_V \frac{\partial N^N}{\partial \mathbf{x}} \cdot \mathbf{k} \cdot \frac{\partial \theta}{\partial \mathbf{x}} dV - \int_V N^N r dV - \int_{S_q} N^N q dS = 0 \tag{3.9}$$

This is now a non-linear system that is solved using the modified Newton method. The conventional Newtonian method uses a tangential matrix (a Jacobian matrix) to solve the equation, but the time rate of change of the variables in the left-hand-side of the equation with respect to the $\theta^N_{t+\Delta t}$ does not easily form within the standard Newton tangential matrix. Thus the internal energy, seen as the first integral in Equation 3.9, must contribute to the Jacobian in the following way:

$$\frac{1}{\Delta t} \int_V N^N \rho \left.\frac{dU}{d\theta}\right|_{t+\Delta t} N^M dV \tag{3.10}$$

Similarly, the conduction term (second term in Equation 3.9) is written as

$$\int_V \frac{\partial N^N}{\partial \mathbf{x}} \cdot \mathbf{k}\Big|_{t+\Delta t} \cdot \frac{\partial N^M}{\partial \mathbf{x}} dV + \int_V \frac{\partial N^N}{\partial \mathbf{x}} \cdot \left.\frac{\partial \mathbf{k}}{\partial \theta}\right|_{t+\Delta t} \cdot \left.\frac{\partial \theta}{\partial \mathbf{x}}\right|_{t+\Delta t} N^M dV \tag{3.11}$$

ABAQUS does the same thing for film conditions and radiation, but these are outside the scope of this project and are therefore neglected.

3.4.4. Model assumptions

Radiation

Most engineering solutions rely on assumptions to ease the computational burden or development time of the project; these simulations are no different. The first assumption was that the material is fully insulated from thermal radiation. Mars is well known to have a less effective atmosphere, when compared to Earth, thereby leading to rapidly changing temperatures during the days. This also means that solar radiation is significantly more than that observed on the Earth's surface. This can affect the reaction mechanisms of the material, and are neglected from the analysis due to the sheltering the material will receive from its housing in Martian buildings and homes.

Material constants

ABAQUS and the user-subroutines use numerous material characteristics to compute the simulation, with some being used as material constants. The four material characteristics that were assumed to be constants are:

- Mass density
- Specific heat capacity
- Thermal conductivity
- Mass diffusivity

The specific heat capacity and mass density of a virgin material was taken for each simulation (i.e., no reaction had taken place) and was assumed to be constant throughout the simulation of that material. In real life, the mass density changes when more CO_2 is adsorbed into the material.

This means that the specific heat capacity should also be variable in real life, as the specific heat capacity would change depending on how much the material was loaded. For a fully loaded material, the specific heat capacity would be higher than the assumed value.

The thermal conductivity of the material would theoretically increase as the material is loaded with CO_2, but is kept constant in this model. The difference in conductivity values should not be drastically different, as CO_2 is a poor conductor of heat.

The mass diffusivity of the material is an indication of how easily the CO_2 can diffuse through the material. As the material is loaded, the diffusivity should decrease in real life. Unlike thermal conductivity, the driving force behind mass diffusivity changes when one looks at different length scales. At the macro-scale, the diffusivity is determined by the macro-pore/bulk diffusion. When examined at the molecular scale, the diffusivity is determined by the spaces created by the metal-organic-framework (as seen in an example shown in Figure 3.1). However for the purpose of this thesis, the mass diffusivity is said to be constant because only the macro-porosity is taken into consideration. The diffusivity is taken as a material constant and treated as a bulk material characteristic, an assumption that exaggerates the mass diffusion for a loaded material. According to numerous experts, this variation in mass diffusion plateaus quickly and can indeed be taken as a material constant [23][15].

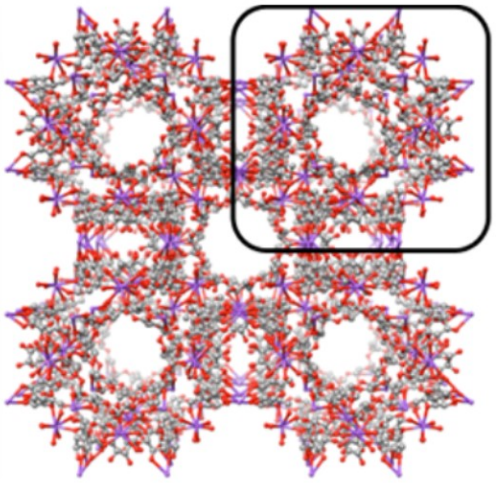

Figure 3.1: Nano-porosity of CD-MOF-2 [16]

Homogeneous material characteristics

Numerous existing papers preform experimental adsorption tests to determine the possible use-case of metal-organic framework materials for applications such as filtration and capture technology. In theory, the adsorption kinetics for thermal energy storage applications are almost identical, with the only difference being the parameters the metal-organic framework materials are designed for. The papers see a mix of bulk metal-organic framework materials and granular metal-organic framework materials. Granular metal-organic framework beads/powder are an attractive proposition for their macro-porous geometry, leading to as high surface-to-volume contact ratio. The simulation also tends to be simpler, with finite element analysis replaced by granular media simulation methods. However, this method is highly fluid dependent and does not fully evaluate the capabilities of the material for Martian applications. Furthermore, the surrounding auxiliary systems used in granular metal-organic framework material systems all require active control, which is less desirable for an extra-terrestrial thermal battery. It is for these reasons that the metal-organic framework materials used in this study are treated as bulk materials with bulk material properties.

The bulk metal-organic framework materials can be seen as homogeneous when operated in a passive manner. *Salles et al.* further elaborates that the directional properties of diffusion and conduction in the material are only significant if the heat transfer fluid (e.g., CO_2) is pumped into the material using a

pressure gradient [24]. As the metal-organic framework materials used in this thesis aim to be passively operated, the diffusion of CO_2 would happen with a simple concentration gradient. For this conventional diffusion, the metal-organic framework materials' diffusion and heat conduction characteristics are constant for all directions and for most of the operating temperatures.

Reaction constants

The ABAQUS diffusion simulations focus entirely on the conductivity/diffusion constants, the specific heat capacity, and the mass density; almost none of these parameters are relevant when modelling chemical reactions in metal-organic framework materials. The chemical reactions are dictated by the the rate of reaction, the reaction enthalpy, the activation energy, and the available active site.

The activation energy is the "reaction floor" cumulative energy exerted at the active site, which must be breached before any reaction takes place. For the case of metal-organic framework materials, the activation energy can be simplified to a simple temperature condition. Existing research into adsoprtion within metal-organic framework materials have been relatively limited, with very little information pertaining to the molecular dynamics behind the reaction. Current research tests the reaction kinetics for the bulk material. This makes it highly boundary condition dependent. It is for this reason that a simple temperature condition was chosen. Most metal-organic framework materials have temperature regions for which the adosrption and desorption processes begin. Buy assuming that adsorption is triggered at a certain temperature, while desoprtion is triggered at another set temperature, the need for activation energies is unnecessary.

The reaction enthalpy is constant for each metal-organic framework material and their corresponding heat-transfer fluid. This study looks at three different types of materials: MOF-5, UiO-666, and Zeolite-5A. The rate of reactions, measured in units $kg_{CO_2}/(kg_{material}\ s)$, could be tuned to match experimental data. The rate of reactions quantified as percentages of the total loading capacity; a ratio of 1.0 would imply that the element can be fully saturated in a single second, while a ratio of 0.5 leads to the element fully saturating with CO_2 in two seconds. Note that the time dependent saturation requires sufficient mobile CO_2 diffused in the material, thus leading to different actual rates of adsorption in the simulation.

The reaction ratios for MOF-5, UiO-666, and Zeolite-5A are: 0.1, 0.2, 0.1. This calibration method is further elaborated in section 4.1.

3.5. Implementation in ABAQUS

ABAQUS CAE (complete abaqus environment) is the graphical interface on Windows, that allows the user to setup and run simulations using in an interactive input style. A screenshot of this program can be seen in Figure 3.2. This section gives further insight into how the input files and subroutines were created for the purpose of the simulation.

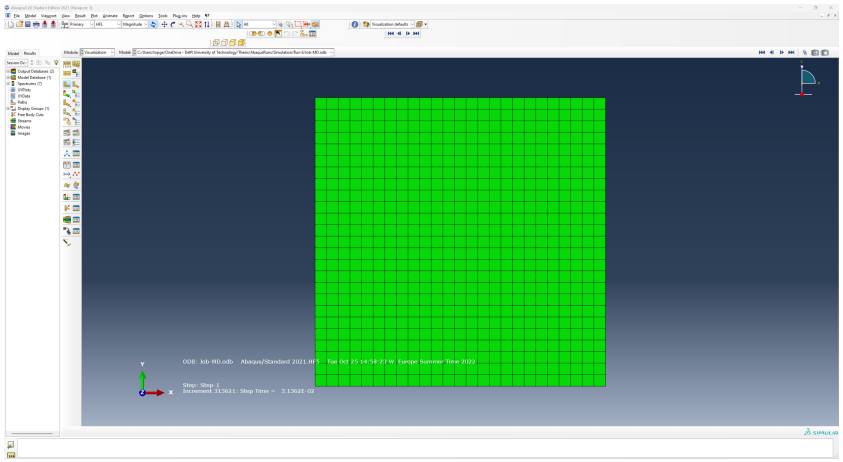

Figure 3.2: A screenshot of the user interface ABAQUS CAE provides

3.5.1. Creation of the input files

ABAQUS uses input files to run simulations. Despite CAE having a graphical interface, the software creates input files from the choices the user makes in CAE. The structure of the input file closely resembles the work flow of the user in CAE. There are six key steps in ABAQUS, needed to create a simple simulation: part design, material allocation, step creation, mesh generation, load application, and creation of input files.

Part design is about creating a CAD (computer-aided design) model of the geometry the user is trying to model; a block of a metal-organic framework material in this case. A 2D geometry was used for the simulations, as it provided sufficient understanding of the adsorption process without requiring long computational times. Therefore, a 2D planar shell geometry was created. The geometry is a 5x5m square.

The second step is to assign material properties to the newly created part. This simulation uses three key material properties: density, specific heat capacity, and thermal conductivity. The density determines the amount of material available for the sorption process. The thermal conductivity is used to track the rate of heat dispersion through the material due to the heat transfer fluid and the sorption reactions. The specific heat limits the amount of thermal energy conducted through the material, as the material has some innate thermal storage properties (sensible heat storage).

Step loads are the primary way the loads are applied to the simulations. A step load in CAE was defined by the time scales and increments. In order to accommodate two simulations running simultaneously, the time scale for each increment must be identical. This requires a fixed time increment, as supposed to the standard 'automatic' settings CAE provides. The time increment step gave the most issues during the making of these simulations, and the issues will be outlines in subsection 3.5.3. The fixed time increments were 0.1 seconds, with a total simulation time of 8 hours (288000 total increments).

The mesh generation was done via the CAE interface. Mesh elements had to be changed to DC2D4 elements, which is used by ABAQUS for heat transfer problems. The actual mesh is created by assigning the space between seeds. Seeds help create the points along the edges which are used to create the first elements. Therefore, the spaces between the seeds determine how small the mesh elements are in the model. Exactly 10000 elements were used for the square geometry, resulting in 0.05x0.05m sized elements. Mesh quality can be determined by element size, orthogonality, aspect ratio, and skewness:

- Average orthogonality >0.95
- Minimum orthogonality > 0.2
- Average aspect ratio < 10
- Maximum aspect ratio < 35
- Average skewness < 0.33
- Maximum skewness < 0.95

The list above are the quality checks that were done to ensure the mesh was adequate for the simulation. The element size was determined in conjunction with the desired time increment size; larger time increments often require smaller element sizes.

The loads applied to the material were applied using the same set of tools. The initial temperature (and initial concentration of gas) were added to CAE using the 'Predefined Field' load conditions. The temperature and concentration at the boundaries of the material edges were applied using 'Boundary Condition' loads, withthe option to use zero-flux and/or zero-gradient boundary conditions. Finally, the sink term for heat and mass was applied using the 'Body Heat Flux' load, coupled to a User-Defined value. This user-defined value is not fixed by CAE, thus allowing ABAQUS's DFLUX subroutine to customise the conditions for which the sink term is applied. The input files could then be generated by ABAQUS and stored as *.inp* for later use on TU Delft's high-performance computing (HPC) cluster. The user subroutines were written using FORTRAN77, a fixed-form type of the FORTRAN programming language. As someone with prior Python programming experience (a free-form language without a separate compiler), there was a steep learning curve.

3.5.2. Coupling of simulations

The simulations both individually have an input file (containing the geometry and basic boundary conditions) as well as user-subroutines to customise the source term in the form of a heat flux (using DFLUX). The purpose of the coupling is to simulate the chemical reaction using mass and heat sinks, for which both simulation user-subroutines must be able to read the other simulation's data to ascertain the status of the reaction at a certain point in the material. For the convenience, the coupling method has can be seen in Figure 3.3.

Both simulations have the same geometries with the same nodes, elements, and integration points. This is to ensure that all data can be directly translated to the other simulation without needing any numerical conversion/transformation. To solve the simulation, it can be done explicitly or implicitly. An inplicit solution tends to be more stable and relatively simple to do for a single simulation. However when two simultaneous simulations have to solve the diffusion equation, the implicit method would require a re-configured version of the diffusion equation which takes all the variables into account in one equation. This is a full re-write of the conventional diffusion equation, and is therefore the reason the explicit method was used.

The coupling of the simulation uses the staggered approach to solve the combined set of simulations in an explicit manner. The staggered approach involves running a each simulation for one increment, keeping the other simulation's state fixed/frozen in time, before doing the same for the other simulation. Consider HC as the ”heat conduction simulation” and MD as the ”mass diffusion simulation”. When both simulations are run initially, only the predefined fields and boundary conditions are active. The HC would then undergo a single time increment with the assumption that the mass concentration field and sink term are constant according to the initial conditions. After completing the first HC increment and pausing, the MD simulation would undergo its first increment with the assumption that the temperature field and heat flux are constant, and are taken from the results file of the HC's first time increment. This can continue increment by increment until the simulation is completed. The detailed framework can be seen in Figure 3.3.

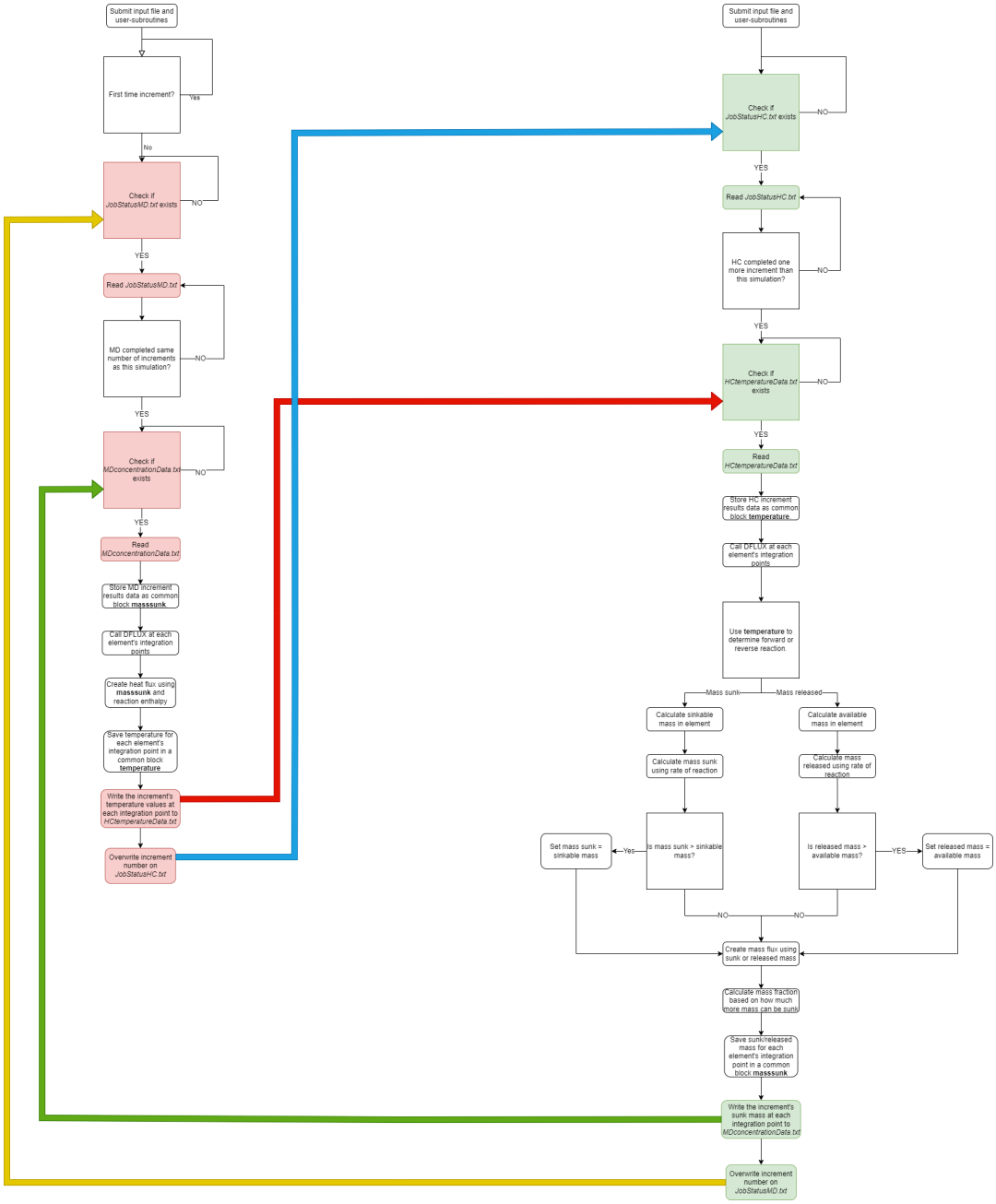

Figure 3.3: A flowchart depicting the coupling process of the heat conduction (HC) and mass diffsuin (MD) simulations.

Starting the simulations
The entire process starts with a single increment of the heat conduction simulation. In its first increment, no source term in used (DFLUX is not called), hence it pure conducts heat based on the initial field and the boundary conditions. After the first increment, the temperature field of the material is stored in a text file named *HCtemperatureData.txt*. The simulation is then paused until the mas diffusion equation completed its increment and passes on the data via *MDconcentrationData.txt*.

Adsorption configuration in DFLUX
The mass diffusion simulation begins by reading the *JobStatusHC.txt* to determine whether the heat conduction simulation has completed its increment, and *HCtemperatureData.txt* to read the temperature field. The user-subroutine that accesses this information before DFLUX is called is named UEXTERNALDB. The temperature field is stored in a common block, marked by its increment number, element number, and integration point.

DFLUX is then called by ABAQUS, along with the common blocks defined/updated in the UEXTERNALDB user-subroutine. Some of the intial constants are defined: number of elements, time increment size, total number of increments, total material volume, element volume, material mass density, total material mass, element mass, loading capacity (CO_2 uptake), and maximum mobile concentration.

DFLUX then looks at the temperature (provided by the common block at that element and integration point for the increment) and assesses if adsorption or desorption will take place. At low temperatures until 273K, the adsorption reactions will take place; mass is sunk/bonded into the material and an exothermic reaction is observed. At this temperature, the mobile concentration should be above zero (else no CO_2 is available to react) and the mass fraction at the element should be under 1.0 (which signifies that there are active sites remaining to react with). A mass fraction of 1.0 means that the material is fully saturated with bonded CO_2 at that element in the material. The rate of reaction is then defined, after the calibration process explained in section 4.1. The sinkable mass is calculated based on the amount of CO_2 that can be bonded to the element; this number is calculated using the mass fraction *n*, mass density ρ, element volume V_{el}, and the loading capacity *L* (as seen in Equation 3.12). Then the calculated sunk mass is calculated using the Equation 3.13.

$$m_{sinkable} = (1 - n) \cdot \rho \cdot V_{el} \cdot L \tag{3.12}$$

$$m_{sunk} = R \cdot (1 - n) \cdot m_{el} \cdot t_{inc} \tag{3.13}$$

where *R* is the rate of reaction, m_{el} is the mass of the element, and t_{inc} is the increment size of the simulation. As long as $m_{sunk} < m_{sinkable}$, m_{sunk} is used as the amount of CO_2 sunk at the element for that increment. If $m_{sunk} > m_{sinkable}$, then $m_{sunk} = m_{sinkable}$.

At temperatures above 300K, the reverse reaction should take place; mass should be released in an endothermic process. At this temperature, the mobile concentration should be above less than the maximum mobile concentration (else no CO_2 could re-enter the mobile fluid) and the mass fraction at the element should be greater than 0. A mass fraction greater than 0.0 means that the material has bonded CO_2 at that element in the material to release. The same equations in Equation 3.12 and Equation 3.13 can be used after being multiplied by -1. As long as $m_{sunk} > m_{sinkable}$, m_{sunk} is used as the amount of CO_2 released at the element for that increment. If $m_{sunk} < m_{sinkable}$ (a greater negative number), then $m_{sunk} = m_{sinkable}$. All other conditions see a zero mass sunk value and a zero rate of reaction.

The flux is calculated by using Equation 3.14, which has the units s^{-1} (the same units used in Equation 3.1.

$$S = -\frac{m_{sunk}}{m_{el} \cdot t_{inc}} \tag{3.14}$$

The mass sunk, used in the sink term, is stored in a common block and exported to a text file (titled *MDconcentrationData.txt*) at the end of the increment.

The heat conduction simulation begins reads *JobStatusMD.txt* to determine whether the mass diffusion simulation has completed its increment, and *MDconcentrationData.txt* to read the temperature field.

The mass sunk field is stored in a common block, marked by its increment number, element number, and integration point.

DFLUX is then called by ABAQUS, along with the common blocks defined/updated in the UEXTERNALDB user-subroutine. Some of the initial constants are defined: number of elements, time increment size, total number of increments, total material volume, material mass density, and reaction enthalpy. The flux; the latter two defined using the data in Table 3.3 and Table 3.4. The heat flux, with units J/s, is provided to DFLUX using Equation 3.15

$$S = \frac{m_{sunk} \cdot h_{reaction}}{t_{inc} \cdot V_{el}} \tag{3.15}$$

where $h_{reaction}$ is the enthalpy of adsorption (taken from Table 3.4). The updated temperature field is stored in a common block and exported to a text file (titled *HCtemperatureData.txt*) at the end of the increment.

3.5.3. Resolved issues

To replicate the findings of the report, one must also consider the concessions made when resolving common, yet significant, issues. These primary issues were: time step size, mesh refinement, choice of user-subroutines, and method of coupling simulations.

Increment step size and mesh refinement

For a true staggered approach, the small time steps are used to ensure both simulations do not progress too much without feeding and updating information to the other simulation. The aforementioned materials are estimated to take hours of reaction time, in order to sink a significant amount of CO_2. This requires relatively large time increment sizes, within the limit of mesh tolerance. During the course of creating the simulations, the mesh had to be refined significantly to allow the solution to converge. Large heat and mass fluxes led to heat flux residuals that did not meet the set solution criterion ABAQUS set. By refining the mesh down to a mesh count of 300,000 - 500,000 elements, an increment size of 50 seconds could be achieved.

Choice of user-subroutines

ABAQUS has numerous user-subroutines available for heat transfer and mass diffusion simulations, namely the following user-subroutines: DFLUX, HETVAL, and UMATHT. According to the ABAQUS manual, "*DFLUX is can be used to define a nonuniform distributed flux as a function of position, time, temperature, element number, integration point number, etc. in a heat transfer or mass diffusion analysis. DLUX will be called at each flux integration point for each element-based or surface-based (heat transfer only) nonuniform distributed flux definition in the analysis, and uses the nodes as flux integration points for first-order heat transfer*. This is the simplest form of adding a heat/mass source to an object, in the form of a surface flux or a body flux (which was what was chosen for this simulation). This heat flux is the thermal energy per unit time at the material point.

HETVAL was the obvious initial choice, ahead of DFLUX, due to its specialisation in internal heat generation: *"HETVAL can be used to define a heat flux due to internal heat generation in a material, for example, as might be associated with phase changes occurring during the solution"*. Unlike DFLUX however, HETVAL is not called at each element and therefore acts in unison for the entire material body. In practice, HETVAL would not isolate regions of heat generation, but would instead apply an average heat flux over the entire body. It is for this reason that HETVAL was not chosen.

UMATHT is one of the most powerful user-subroutines that ABAQUS offers, with flexibility to change every body's characteristics at each point. Like DFLUX, it is called at each element's integration point. The disdvantage of using UMATHT's heat flux method is its effect on the solution. The heat flux UMATHT is not the thermal energy per unit time at the material point (like DFLUX and HETVAL), but instead a heat flux vector that must be further defined before being used as a sink term in the diffusion equation. This inconvenience was the reason why UMATHT was not chosen.

Method of coupling simulations

ABAQUS stores solution data in the form of *.odb* and *.fil* files, the former used for data visualisation in ABAQUS CAE and the latter written in binary text. ABAQUS provides the user with a subroutine named

DBFILE to access the results database. It is conventionally used to track the solution and stop when a certain criterion is met. For example, one can use DBFILE to read the results files and determine when the average temperature of the material is above 500K. THe subroutines can then use this as a flag to terminate the simulation.

The initial approach taken was to use DBFILE to view the results file of the other simulations, thereby getting immediate access to the temperature fields, concentration fields, and other stored data. Despite a lot of attempts to use this built-in method, ABAQUS was not designed to be used this way; when the other simulation detected the opening and reading of its results file, it terminated the simulation as a fail-safe to avoid memory leaks.

A ”brute-forced” method had to be used to transfer the necessary data from one simulation to another. Ordinary text files (*.txt*) were used to store temperature field and mass sunk field of the latest time increments. Only the latest increment was stored, overwriting the previous increments, due to the size of the files that would result from the practice of storing all increments' data. For most cases this is the bottleneck that limits the speed of ABAQUS simulations, as reading and writing text files is a relatively slow process.

Reading and writing data in text files

To be able to read the other simulation's text file at the start of the increment (before DFLUX is called) and write into a text file at the end of the increment (after DFLUX has completed) requires the use of a user-subroutine UEXTERNALDB; *”It is called once each at the beginning of the analysis, at the beginning of each increment, at the end of each increment, and at the end of the analysis”*.

4

Results

With the model built, simulations could run on the HPC clusters. This chapter outlines the mesh sensitivity analysis, reaction calibration process, verification steps, the nature of simulations conducted and their results, followed by the validation of data.

4.1. Reaction calibration process

As mentioned in subsection 3.4.4, the rates of reactions for MOF-5, UiO-66, and Zeolite-5A needed to be found. This was done by comparing the model to experimental data, and matching them to experimental data. The materials have been predominantly studied by material scientists for material properties, thus conducting experiments on very small samples of the material; all three papers used crystal forms of the material (2.35mm x 2.35mm).

4.1.1. MOF-5 calibration

The rate of reaction was calibrated using the data taken from *Zhao et al.*'s paper of MOF-5 [15]. As seen in the Figure 4.1, the uptake mass fraction is a function of time, yet is also temperature dependent.

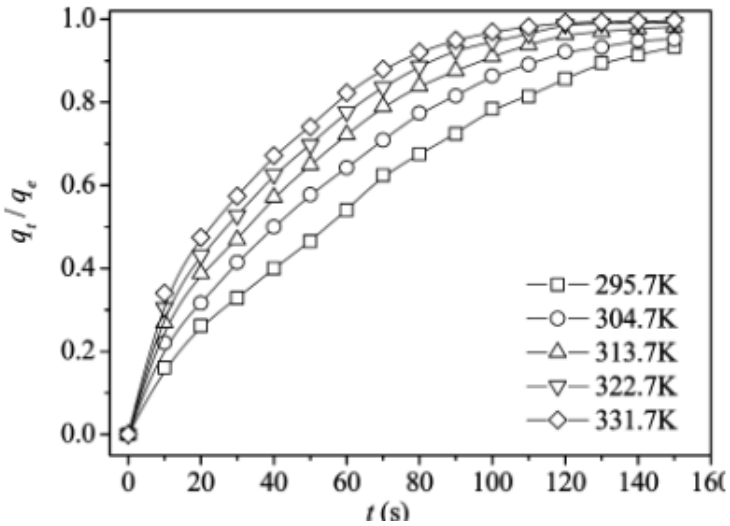

Figure 4.1: Experimental data of CO_2 uptake for MOF-5 [15].

Figure 4.2 shows that the reaction ratio of 0.1 closest resembles the experimental data. Note that the boundary conditions used in this paper were readily available, making the curve-fitting method possible. The aim of the calibration is not to match the data exact data set, but to replicate the same curve. Note that the maximum loading capacity is 0.44 $kg_{CO_2}/kg_{MOF\text{-}5}$. Thus the rate of reaction used for MOF-5 is 0.044 $kg_{CO_2}/(kg_{MOF\text{-}5}$ s)

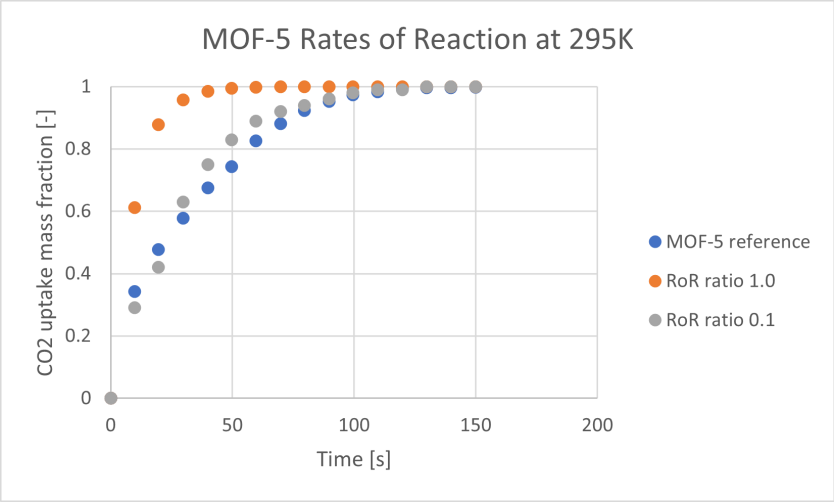

Figure 4.2: The calibration of the rate of reaction (RoR) for MOF-5 using (orange) reaction ratio 1.0, (grey) reaction ratio 0.1.

4.1.2. UiO-66 calibration

In the same way, a paper by *Zhuang et al.* was used to calibrate the RoR for the UiO-66 material during CO_2 adsorption. The green line in Figure 4.3 was used for the comparative analysis.

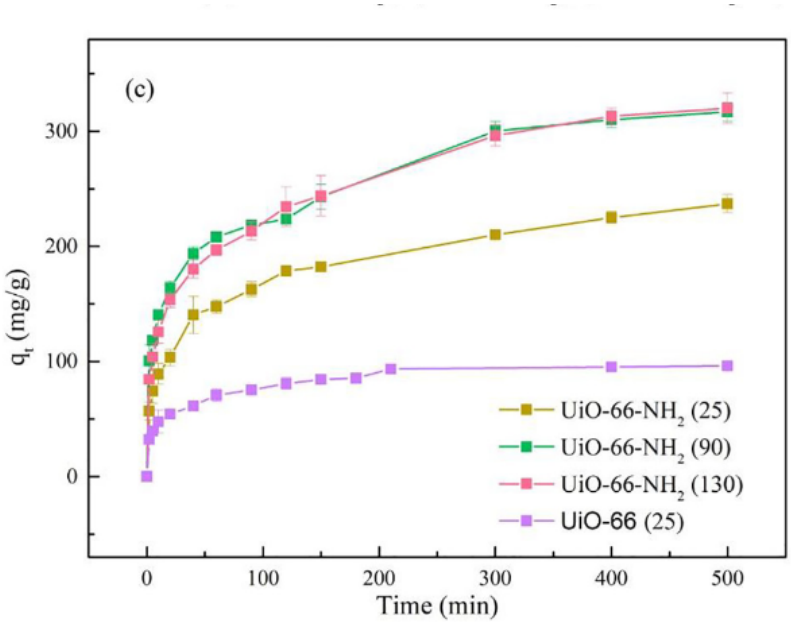

Figure 4.3: Experimental data of CO_2 uptake for UiO-66 [25]

Figure 4.4 shows that the reaction ratio of 0.2 closest resembles the curve found in experimental data. Note that the boundary conditions used in this paper were not readily available, making the curve-fitting method difficult. The aim of the calibration was to replicate the characteristics of the curve, namely the flattened section between 80-150 seconds, before increasingly rapidly again to above 0.9 mass fraction. The ratios above 0.2 lead to faster initial spikes in CO_2 uptake (such as the grey data points) and smoother plateaus above 0.9 mass fraction. Ratios below 0.2 lead to very slow uptake speeds that do not reach material saturation within 500 seconds. Note that the maximum loading capacity is 0.11748 $kg_{CO_2}/kg_{UiO\text{-}66}$. Thus the rate of reaction used for UiO-66 is 0.0235 $kg_{CO_2}/(kg_{UiO\text{-}66}$ s)

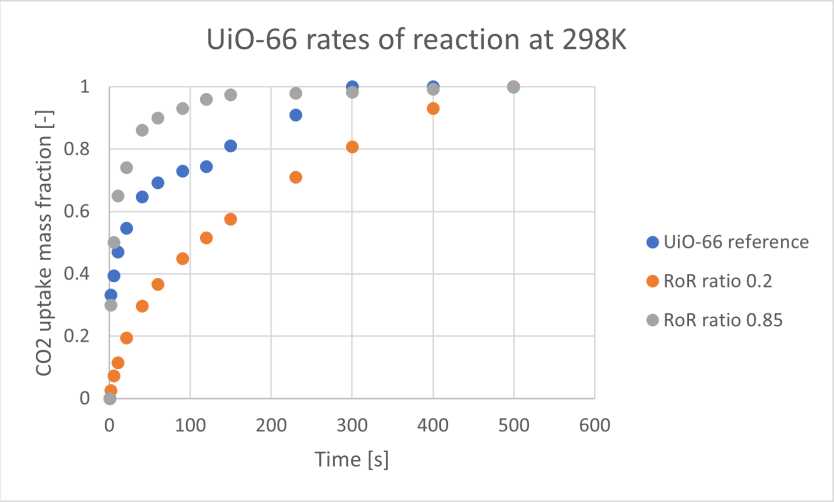

Figure 4.4: The calibration of the rate of reaction (RoR) for UiO-66 using (orange) reaction ratio 0.2, (grey) reaction ratio 0.85.

4.1.3. Zeolite-5A

Much like the first two materials, a paper by *Sami et al.* was used to calibrate the RoR for the Zeolite-5A material during CO_2 adsorption. The solid black line (labelled 1st ref BC) in Figure 4.5 was used for the comparative analysis.

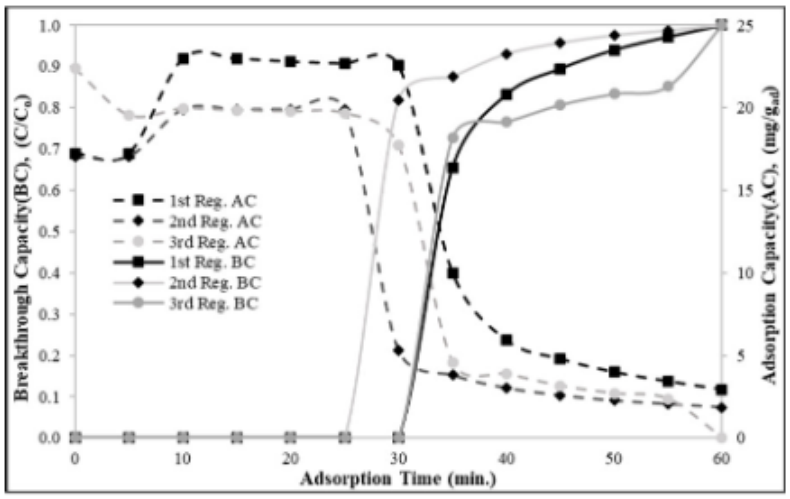

Figure 4.5: Experimental data of CO_2 uptake for Zeolite-5A [26]

Figure 4.6 shows that the reaction ratio of 0.1 closest resembles the curve found in experimental data. Note that the boundary conditions used in this paper were not readily available, making the curve-fitting method difficult. The aim of the calibration was to replicate the characteristics of the curve, namely the flattened section between 10-18 minutes, before increasingly rapidly again to above 0.9 mass fraction. The ratios above 0.2 lead to faster initial spikes in CO_2 uptake (such as the grey data points) and smoother plateaus above 0.9 mass fraction. Ratios below 0.2 lead to very slow uptake speeds that do not reach material saturation within 30 minutes. Note that the maximum loading capacity is 0.3 $kg_{CO_2}/kg_{Zeolite\text{-}5A}$. Thus the rate of reaction used for UiO-66 is 0.03 $kg_{CO_2}/(kg_{Zeolite\text{-}5A}\ s)$

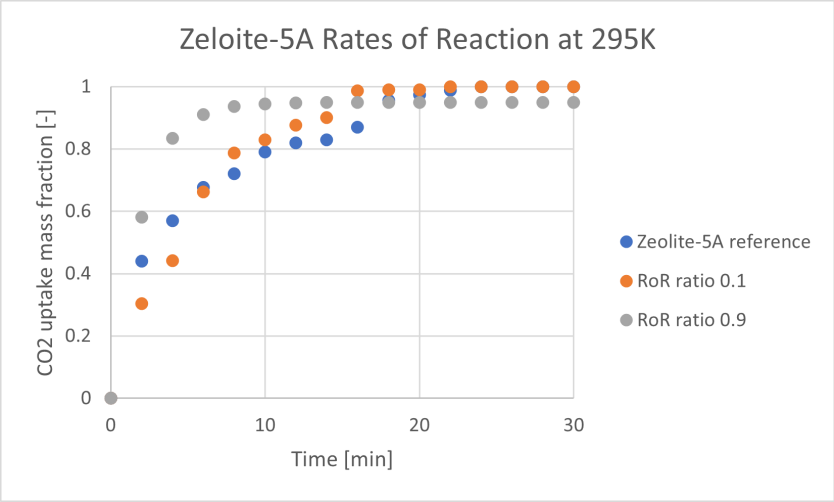

Figure 4.6: The calibration of the rate of reaction (RoR) for Zeolite-5A using (orange) reaction ratio 0.1, (grey) reaction ratio 0.9.

4.2. Verification

The verification of a model such as this, involves determining whether the model works as intended to. Before one can produce results to validate and conclude, the verification process ensures that the model works correctly based on the boundary conditions and material parameters that have been provided to it. Furthermore, it is essential to verify the coupling process, where the reading and writing of text files (in often non-fixed text formats) dictate the outcome of the simulation.

The first step is the zero-input verification. When zero mass is available at the material boundary, or when the material's temperature is at equilibrium (with no reactions taking place), the diffusion and conduction simulations should see zero flux over every element in the material. This verification step was done by forcing the flux values to be zero in the DFLUX user-subroutine, and changing the predefined material fields to be 200K (same as ambient temperature) and 0.57 (same as the ambient CO_2 concentration). After the simulation was run for a time increment size of one second, for a duration of 60 increments, the total internal flux at each time step was integrated in ABAQUS and was found to be zero for each increment. This successfully completed the zero-input verification.

The second verification step was to see whether the coupling method worked as intended. This was done by keeping one simulation fixed (e.g., constant temperature field gradient) and feeding the data to the other simulation (i.e., the mass diffusion simulation). The simulation was run for just three increments during which the *HCtemperatureData.txt* was logged for the temperature field at each increment. The mass diffusion equation was set up to print the temperature field (read from the *HCtemperatureData.txt* text file) onto another text file. Then the data was then confirmed to be correct in magnitude, precision (number of values after the decimal point), and a real number (not a string). This completed the coupling verification method.

The final verification step was to see if the DFLUX sub-routines were configured to react in the correct way. The first step was to trigger pure diffusion/conduction in the simulations. By setting the rate of reactions to zero, the amount of mass sunk (and therefore heat generated) would be zero after calculations. This would lead to pure conduction at the boundary conditions, as well as un-modified CO_2 diffusion. To verify the results of these simulations, two separate simulations were created on ABAQUS CAE (uncoupled pure conduction/diffusion with no user-subroutines). The temperature gradient and concentration gradient were then compared to the two separate simulations and were found to be equal.

The verification of the model, with non-zero values of flux in both simulations, was deemed trivial. The method for which the sink term was derived in DFLUX was detailed in subsection 3.5.2. With only ABAQUS's implementation of the sink term yet to be verified in this study (ABAQUS has been verified by Dassault Systèmes), the model was deemed as verified.

4.3. Material analysis

With the model verified, the simulations could begin for Martian conquest. The first set of simulations conducted were material-based analysis. A 2m x 0.5m 2D geometry was created, with insulated (zero-gradient) boundary conditions on three of the four sides of the rectangular geometry (as seen in Figure 4.7. The geometry had 40,000 quadrilateral elements, and ran for 500 increments (with a time increment size of 50 seconds).

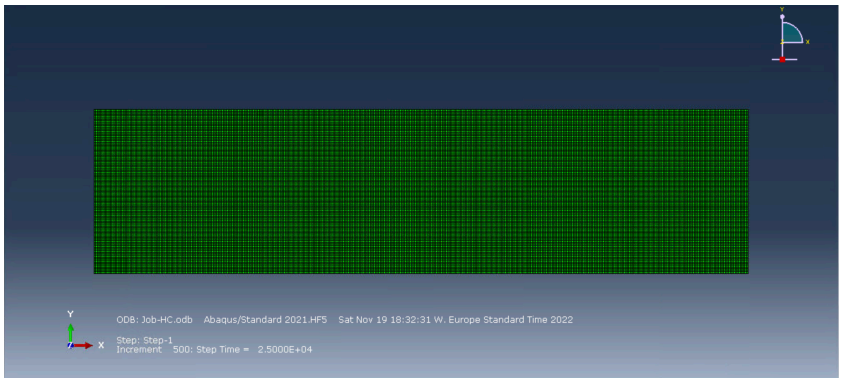

Figure 4.7: 2m x 0.5m bulk 2D shape used for quasi-1D mass sink simulations

The purpose was to run a quasi-1D mass diffusion simulation using each of the three materials separately, to determine how effective the the material is at adsorbing Co_2. The simulations are run with a single concentration boundary condition normalised at 1.0 (at the left vertical boundary). All three materials have different rates of reaction, loading capacity, and mass diffusivity. The average sunk mass fraction (zero throughout the material at the start of the analysis) is averaged to determine the efficiency of CO_2 loading for each material.

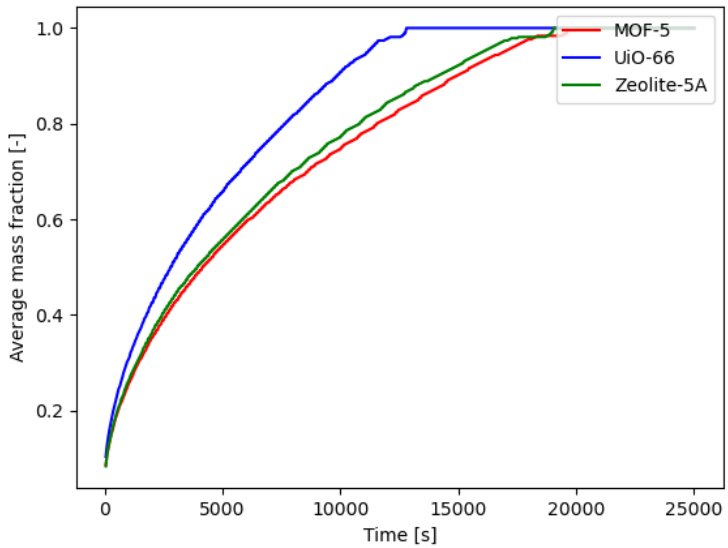

Figure 4.8: The average mass fraction of bulk material during CO_2 adsorption.

The results can be seen in Figure 4.8 and Figure 4.9. Figure 4.8 shows that while MOF-5 indeed has the lowest mass diffusivity coefficient out of the three materials, UiO-66 has the highest by far. As shown in Table 3.3, the difference in diffusivity is small and should not be the sole reason for the faster saturation of UiO-66. The most important aspect in this case is the loading capacity. As mentioned above in section 4.1, UiO-66 has the lowest loading capacity, requiring less Co_2 to fully saturate the

material.

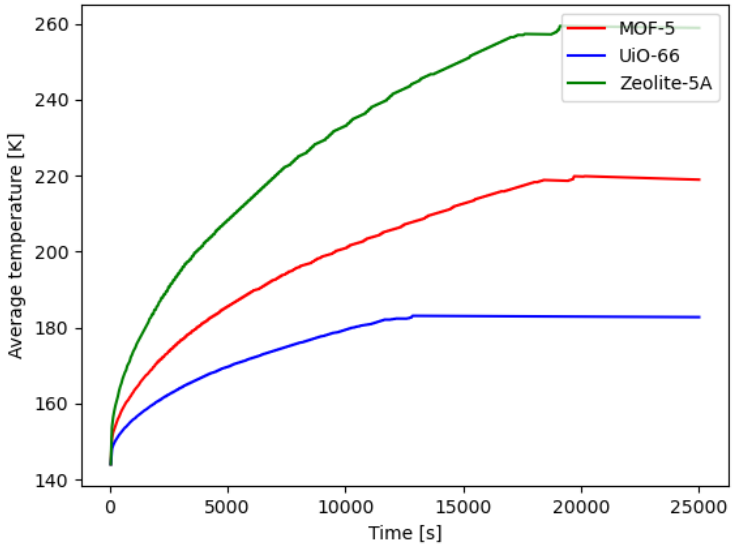

Figure 4.9: The average temperature of bulk material during CO_2 adsorption.

The differences in material properties are more prominent in Figure 4.9. Here, it is clear that the Zeolite-5A outputs significantly higher thermal energy; the UiO-66 has the lowest average temperature. As stated before, the MOF-5 and Zeolite-5A have almost triple to quadruple the loading capacity of UiO-66, leading to a significantly larger amount of CO_2 sunk by the material. MOF-5 and Zeolite-5A have similar CO_2 adsorption kinetics but have drastically different average temperatures; in fact, MOF-5 has a higher enthalpy of adsorption. This can be explained by the higher material density in Zeolite-5A, which is more than four times that of MOF-5. In addition to affecting the specific heat capacity, it results in a significantly heavier bulk material. The loading capacity of Zeolite-5A is approximately 75% that of MOF-5 (as seen in Table 3.3), but will therefore react with nearly three times the amount of CO_2 than MOF-5 does. It is for this reason that Zeolite-5A is seemingly the best option to use for Martian homes.

4.4. Proof of concept

The geometry analysis is the key to understanding the possibility of Martian applications. The material is to act as the wall for stand-alone Martian structures that self-regulate the internal temperature for humans within the Martian structures/buildings. The three materials will be tested with **two???** geometries to determine whether adsorption is a viable option for Martian colonisation.

4.4.1. Geometries

There were two main geometries considered for the martian homes, a square-based and and circular-based geometry. The geometry of the two homes can be summaries in Table 4.1.

Table 4.1: Dimensions of the Marian buildings that use adsorptive materials.

Shape	Inner area dimensions [m]	Inner temperature [K]	Outer area dimensions [m]	Outer temperature [K]	Outer area CO_2 concentration
Circular	Radius = 2.5	291	Radius = 5.0	200	0.57
Square	Square length = 4.43	291	Square length = 8.86	200	0.57

The visual depictions of the geometries can be seen in Figure 4.10 and Figure 4.11 below. Both geometries have approxmately 19.63m^2 of inner liveable space and 58.90m^2 of material (shaded grey in the figures).

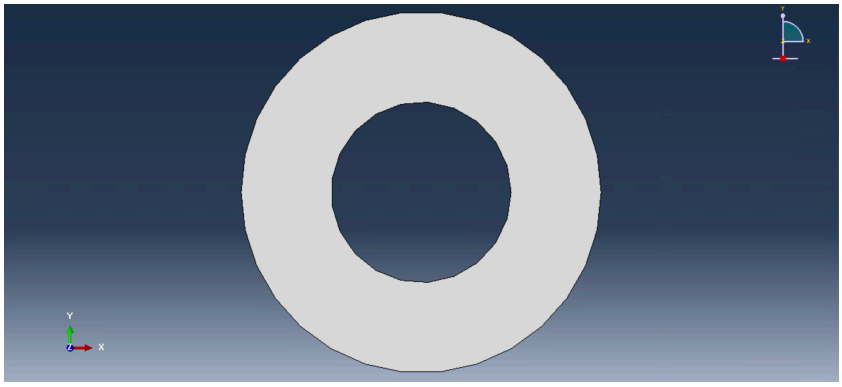

Figure 4.10: The circular building geometry depicting only the adsorptive walls.

For simulation purposes, there were only locations to apply boundary conditions: the inner circle/square and the outer circle/square. The inner boundary conditions reflect the living conditions humans will face when residing in the buildings, namely a temperature boundary conditions of 291K (18 degrees celcius). For the mass diffusion analysis this boundary was considered fully insulated, thereby not allowing any CO_2 to cross-over from the material to the room (or vice versa).

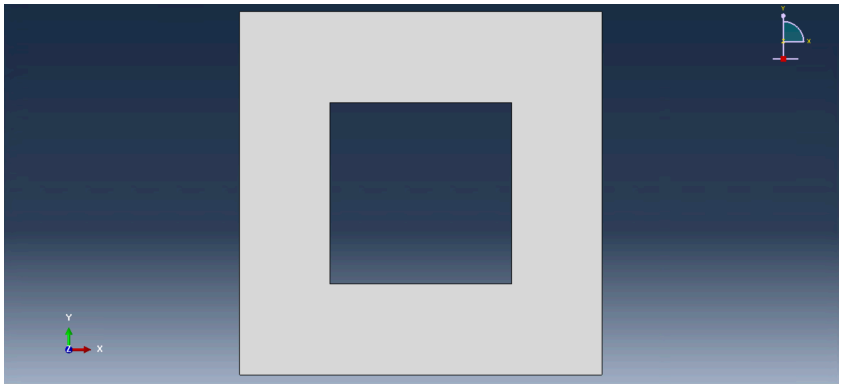

Figure 4.11: The aquare building geometry depicting only the adsorptive walls.

The outer boundary condition must reflect the ambient unforgiving Martian climate, namely a 144-200K temperature boundary condition, and a CO_2 concentration of 0.57. In this simulation the concentration in not normalised, and is therefore the maximum mobile CO_2 concentration allowed in the material.

The inner and outer boundary conditions were configured to be integrated surfaces with history output tracking; the amount of heat entering/leaving the inner boundary (human home) can be measured and integrated, the amount of CO_2 entering the material from the outer boundary can also be measured.

4.4.2. Mesh sensitivity

When relying on simulations, it is vital to understand that the simulation output is a numerical solution; this solution is simply the output result of the problem that posed by the user, and is defined by the mesh and boundary conditions. The mesh is a finite spatial discretisation approximation of a continuous material. The more refined the mesh is, and the more accurate the boundary conditions are, the closer to the true material it will behave when the solutions has converged.

In reality, computational limitations mean that that extremely high refinement leads to long computational times and enormous data file sizes. In most cases, the marginal utility of further mesh refinement diminishes, leaving it up to the user to approve the validity of the solution. This approval is done by conducting mesh convergence. This is a sensitivity analysis done to determine at what level of mesh refinement are the change in results of the model is relatively negligible.

There are two main ways a mesh is refined in finite element analysis: p-refinement and h-refinement

(both seen in Figure 4.12. The p-refinement method refines the same mesh but ”increases the displacement field accuracy in each element” [27]. It increases the degree of the highest complete polynomial (hence called the p-refinement), but maintains the same number of total elements used in the mesh.

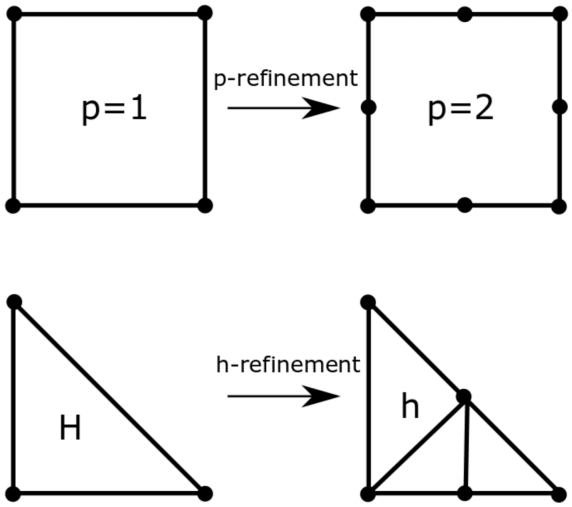

Figure 4.12: Difference between p-refinement (top) and h-refinement (bottom) [27].

The h-refinement method simply make the elements smaller, requiring a larger number of elements in the mesh. The refinement is done by reducing the characteristic length (h) of each element (hence called the h-refinement), dividing element into smaller versions of the same element, much like a tessellation.The key aspect of h-refinement is that the new elements have the same shape as the previous elements they were created from.

The h-refinement method was used due to its simplicity of application. The increase in accuracy for the p-refinement method relies heavily on the increase in complexity of the governing shape functions. The h-refinement is simply a geometric property that is refined using ABAQUS’s built-in meshing software. The two geometries were used with MOF-5, enforced by the dimensions stated in Table 4.1. Quadrilateral elements were used, each with identical mesh parameters other than element characteristic length.

The mesh refinement was done with eight different versions of the mesh, each with a different number of elements: 65,025, 140,625, 267,289, 407,044, 549081, 692,224, 772,641. The goal is measure the average temperature of the material after 35,000 seconds (with a time increment size of 175 seconds). Meshes coarser than 65,000 were not used, due to ABAQUS occasionally failing to converge to a solution as all. The convergence criterion is to see less than 3% change in average temperature values when compared to the previously meshes. The results can be seen in Figure 4.13 and Figure 4.14 below.

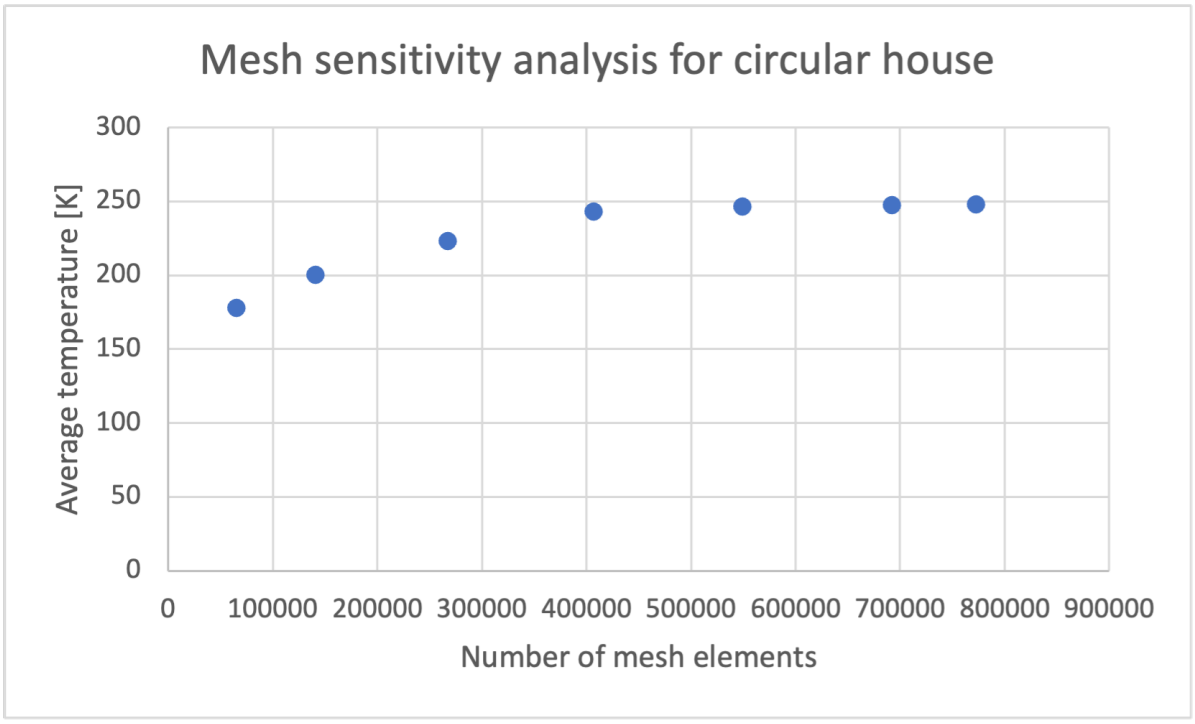

Figure 4.13: Mesh sensitivity of circular walls with MOF-5.

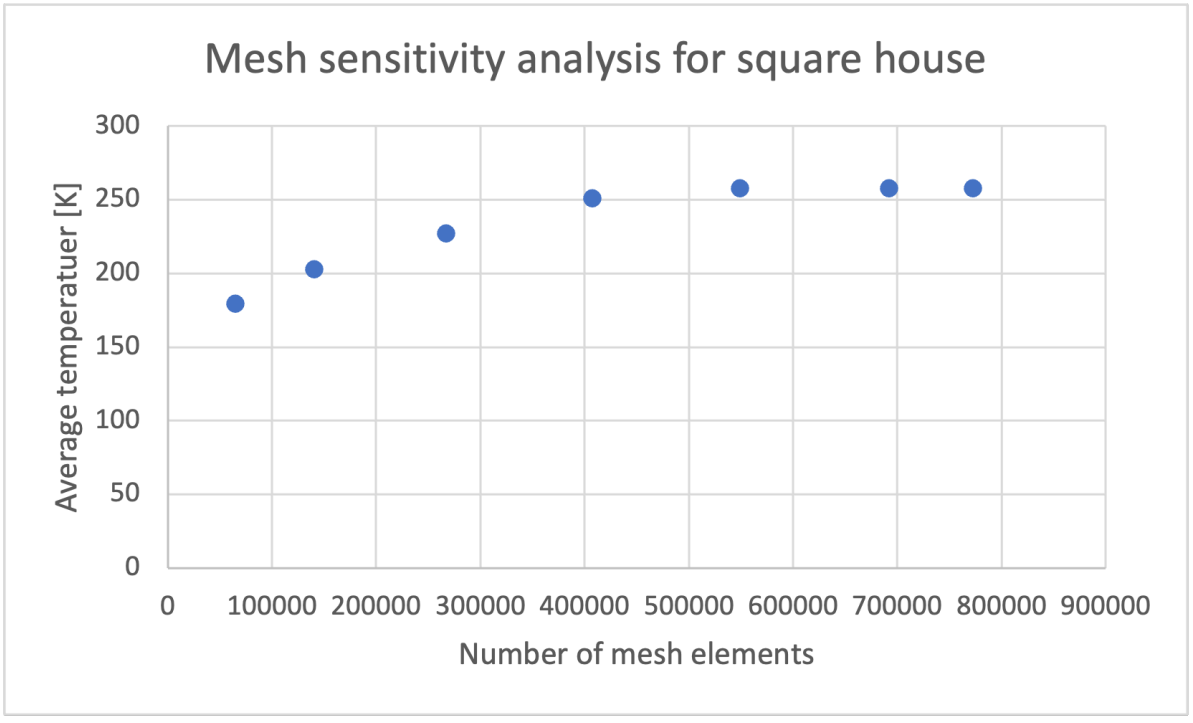

Figure 4.14: Mesh sensitivity of square walls with MOF-5.

The mesh sensitivity analysis showed that the optimal amount elements were found to be approximately 500,000 elements, as it matched the 3% requirement.

4.4.3. Circular house

All three materials showed net negative heat flux through the inner boundary (i.e., heat was lost in the Martian home).

MOF-5

Figure 4.15 shows that the majority of heat generated by the adsorption process is released into the ambient Martian atmosphere rather than into the room, almost an order of magnitude more. When the two curves are integrated (area under the curve) and divided by the total simulation time, the thermal power over both boundaries was found to be approximately -42kW/m and 350kW/m for inner and outer boundaries respectively.

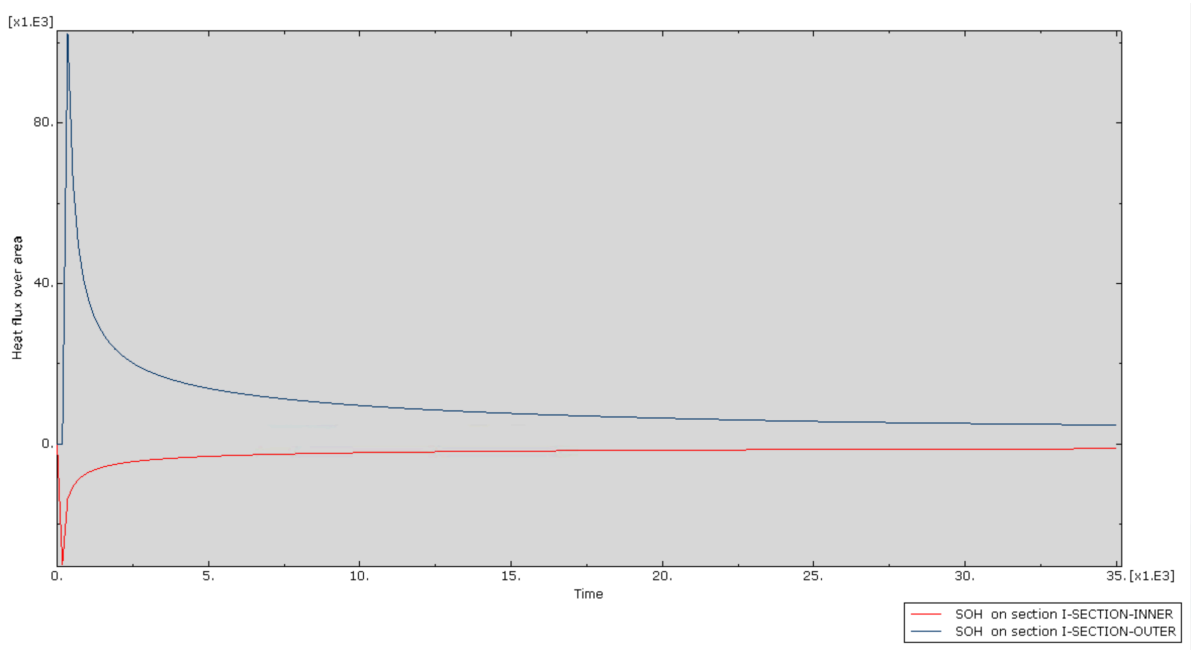

Figure 4.15: Total heat flux leaving the MOF-5 from the inner section, and leaving the material from the outer section (positive values are exothermic).

The contours in Figure 4.16 and Figure 4.17 show the main reason why heat is being drained from the room. The average temperatures reached 245K, and the average mass fraction of the 500,000+ elements were merely 0.258. Given that the room is 291K, this temperature is unsatisfactory. Furthermore, the elements at the midsection-ring in Figure 4.17 are close to 200K (initial temperature). Both heat and mass have not diffused through the material sufficiently quick enough to cause heat generation near the inner boundary.

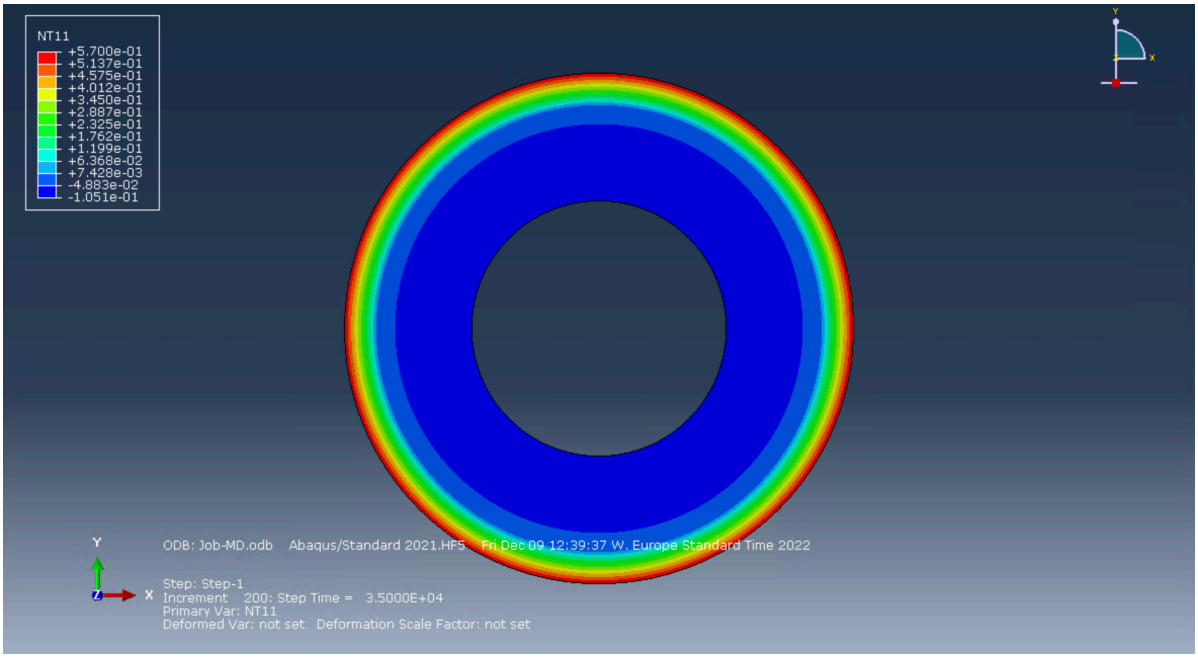

Figure 4.16: Concentration of mobile CO_2 in circular MOF-5 walls

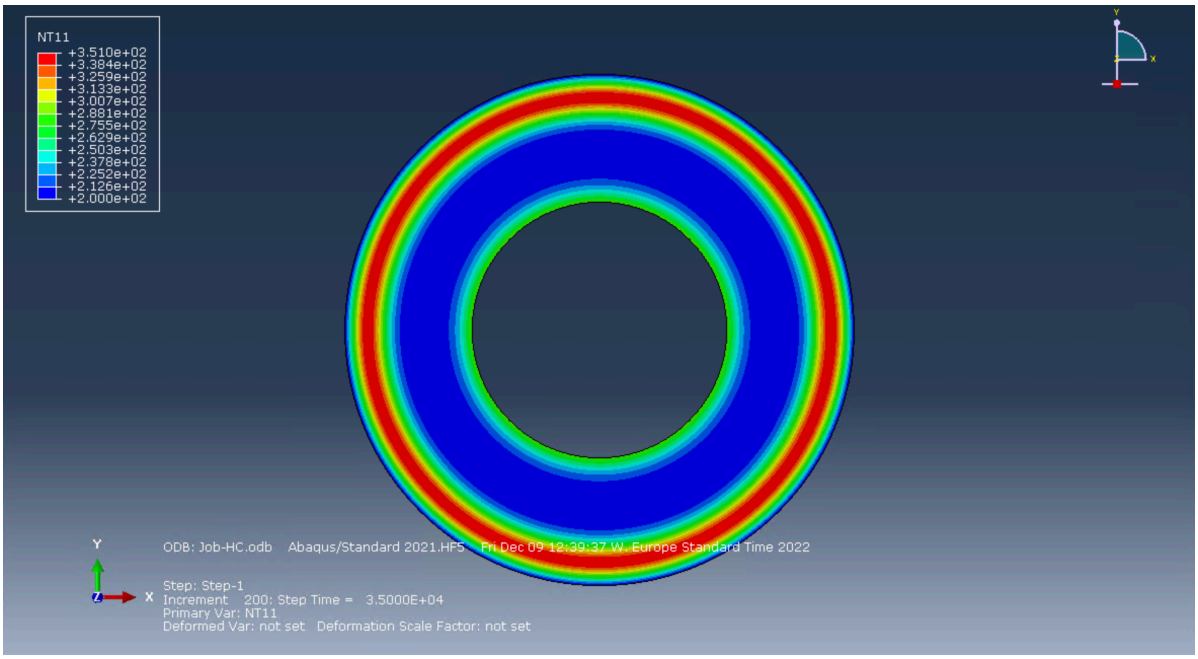

Figure 4.17: Temperature of circular MOF-5 walls

The total thermal power generated by the chemical reaction was found to be approximately 86kW/m, but this was not concentrated near the inner boundary and was thus lost to the environment.

UiO-66

Figure 4.18 shows negative heat flux at the inner boundary, thereby making the room colder. When the two curves are integrated (area under the curve) and divided by the total simulation time, the thermal power over both boundaries was found to be -49kW/m and 52kW/m for inner and outer boundaries respectively.

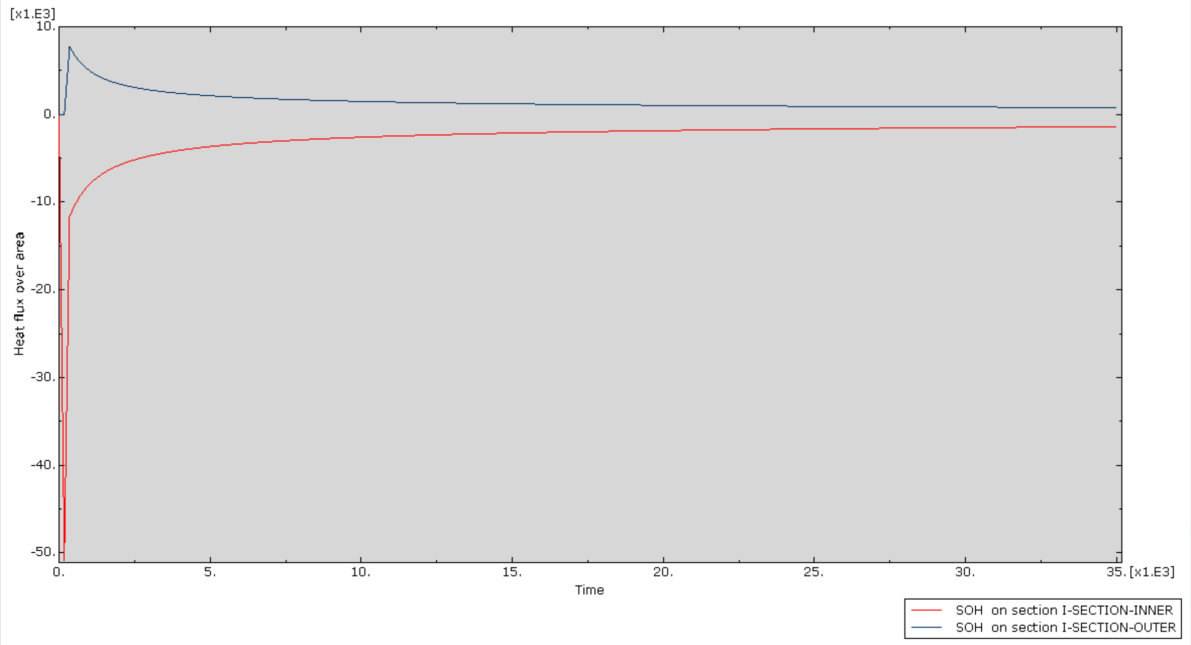

Figure 4.18: Total heat flux leaving UiO66 from the inner section, and leaving the material from the outer section (positive values are exothermic).

The contours in Figure 4.19 and Figure 4.20 also show the main reason why heat is being drained from the room despite over 111kW/m of power being generated by the adsorption reactions. The average temperatures reach only 218K, while the average mass fraction was 0.678. However, the low loading capacity and higher thermal conductivity, as seen in Figure 4.9, are the reasons why the local heat generation is promising, but continues to draw a lot of heat out of the room. As before, the elements at the midsection are close to 200K (initial temperature). Both heat and mass have not diffused through the material sufficiently quick enough to cause heat generation near the inner boundary.

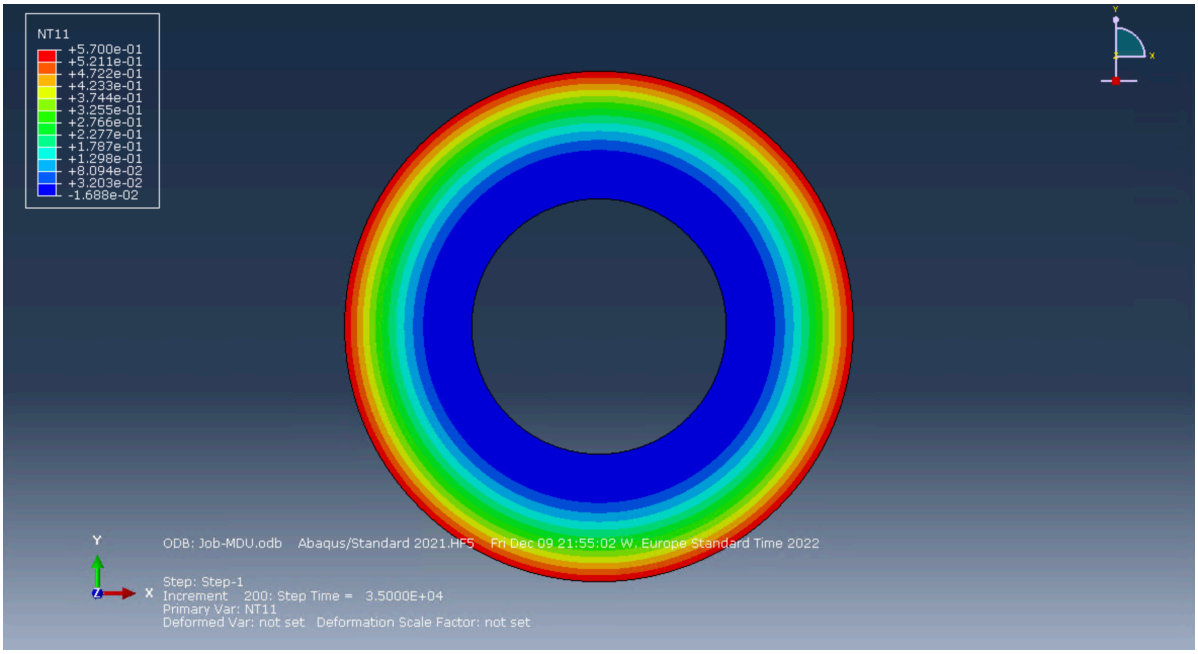

Figure 4.19: Concentration of mobile CO_2 in circular UiO-66 walls

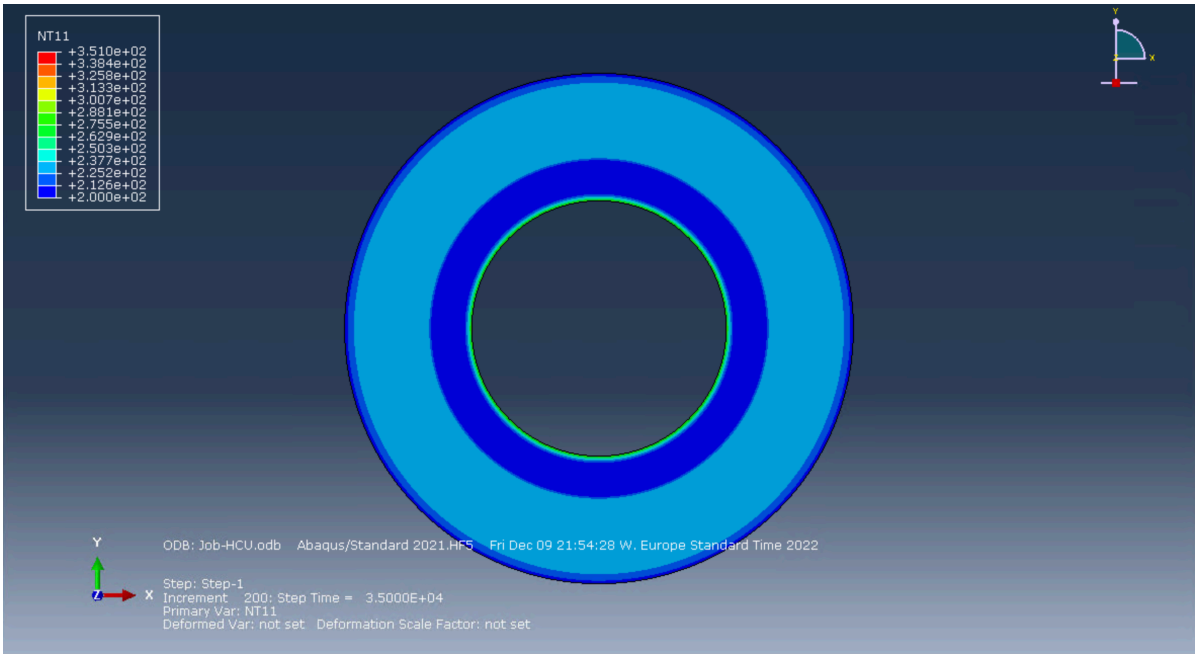

Figure 4.20: Temperature of circular UiO-66 walls

Zeolite-5A

Figure 4.21 shows the heat loss the room sees yet again with this circular configuration. When the two curves are integrated (area under the curve) and divided by the total simulation time, the thermal power over both boundaries was found to be -63kW/m and 207kW/m for inner and outer boundaries respectively.

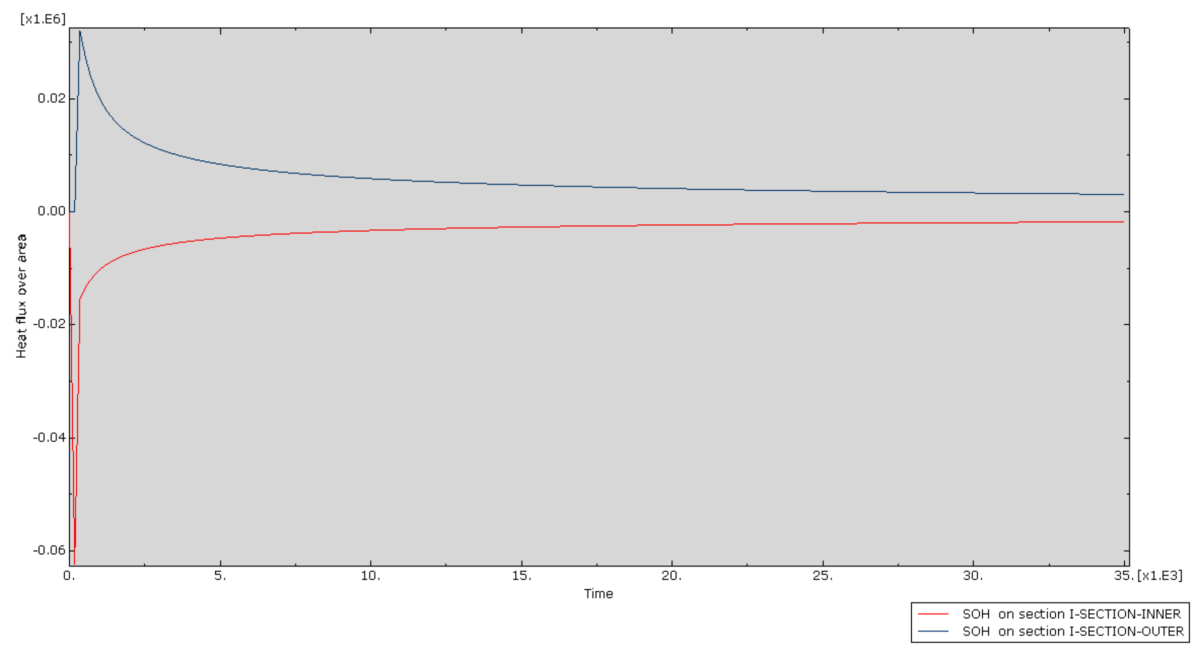

Figure 4.21: Total heat flux leaving Zeolite from the inner section, and leaving the material from the outer section (positive values are exothermic).

The contours in Figure 4.22 and Figure 4.23 also show the main reason why heat is being drained from the room despite over 22W of power being generated by the adsorption process. The average temperatures reaching 229K, while the average mass fraction of 0.374. Unlike early predictions of

Zeolite-5A being the superior choice, seen in Figure 4.9, the Zeolite had the poorest performance due to its low mass fraction and reaction enthalpy combination. The prominence of the mid-section temperatures (close to 200K (initial temperature)) meant that the majority of heat was occurring at the surface. Both heat and mass have not diffused through the material sufficiently quick enough to cause heat generation near the inner boundary.

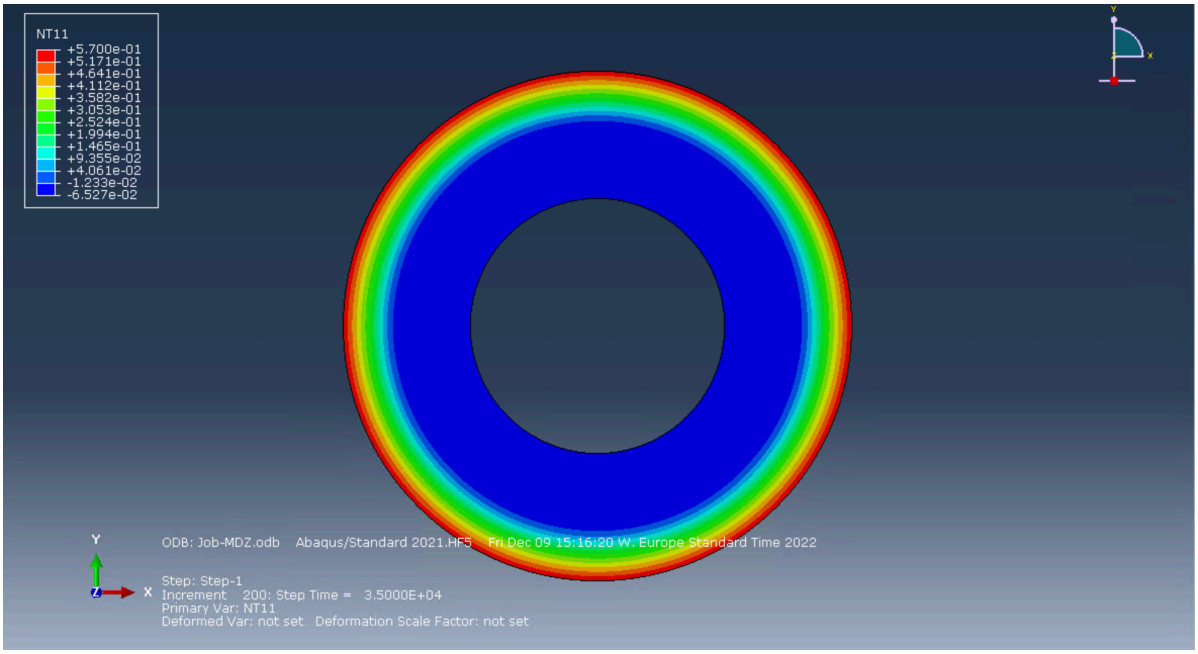

Figure 4.22: Concentration of mobile CO_2 in circular Zeolite-5A walls

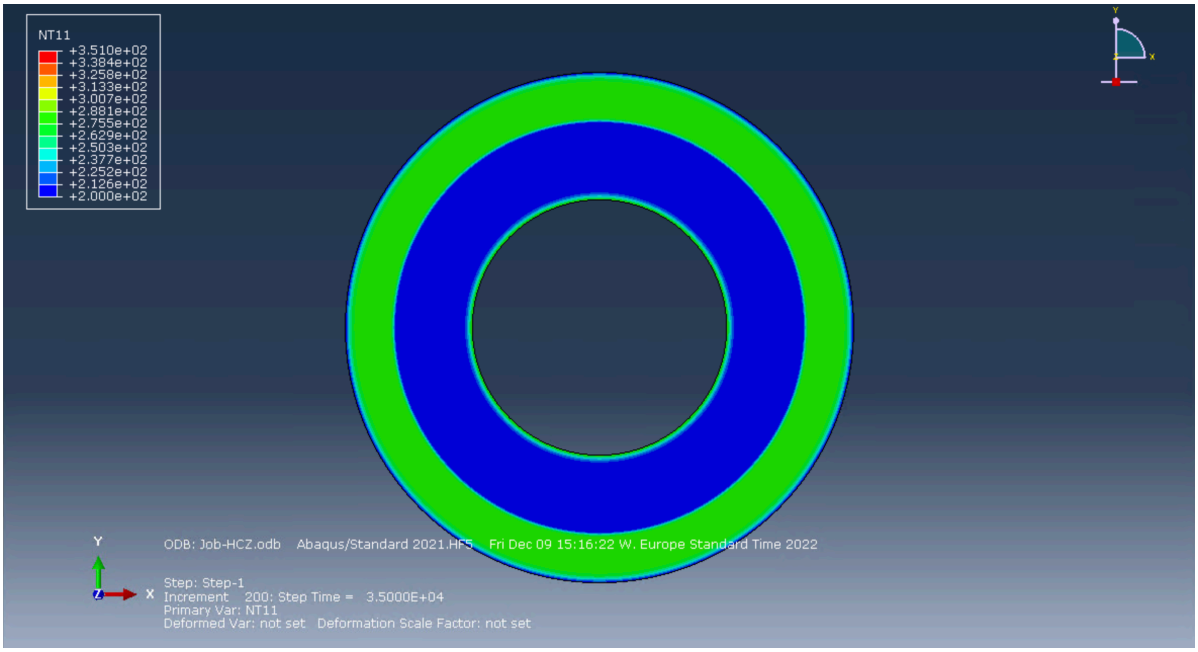

Figure 4.23: Temperature of circular Zeolite-5A walls

4.4.4. Square House

The square geometry showed the same issues the circular geometry had: heat loss from the room and minimal reactions happening close the the inner boundary.

MOF-5

Figure 4.24 shows that the majority of heat generated by the adsorption process is released into the ambient Martian atmosphere rather than into the room. When the two curves are integrated (area under the curve) and divided by the total simulation time, the thermal power over both boundaries was found to be approximately -53kW/m and 441kW/m for inner and outer boundaries respectively.

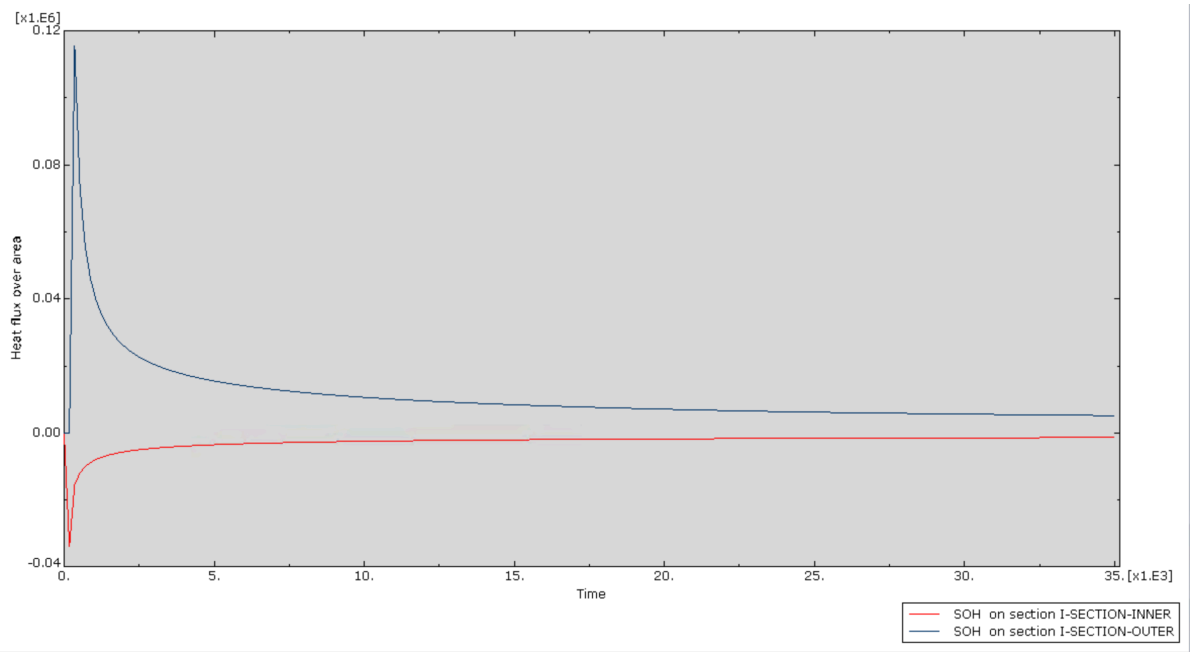

Figure 4.24: Total heat flux leaving the MOF-5 from the inner section, and leaving the material from the outer section (positive values are exothermic).

The contours in Figure 4.25 and Figure 4.26 show the main reason why heat is being drained from the room despite over 118kW/m of power being generated by the adsorption process. Despite the average temperatures reaching 257K, the average mass fraction was merely 0.359, albeit higher than the circular geometry. Like the circular geometry, the midsection elements close to the inner boundary are still at 200K (initial temperature). Both heat and mass have not diffused through the material sufficiently quick enough to cause heat generation near the inner boundary.

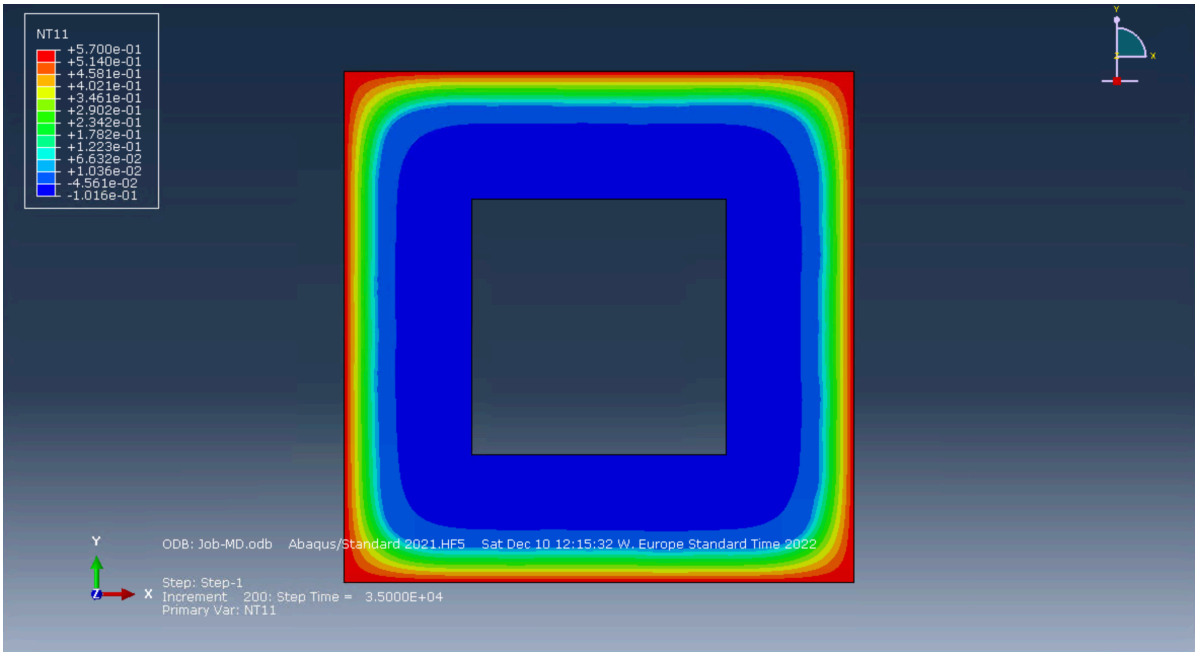

Figure 4.25: Concentration of mobile CO_2 in square MOF-5 walls

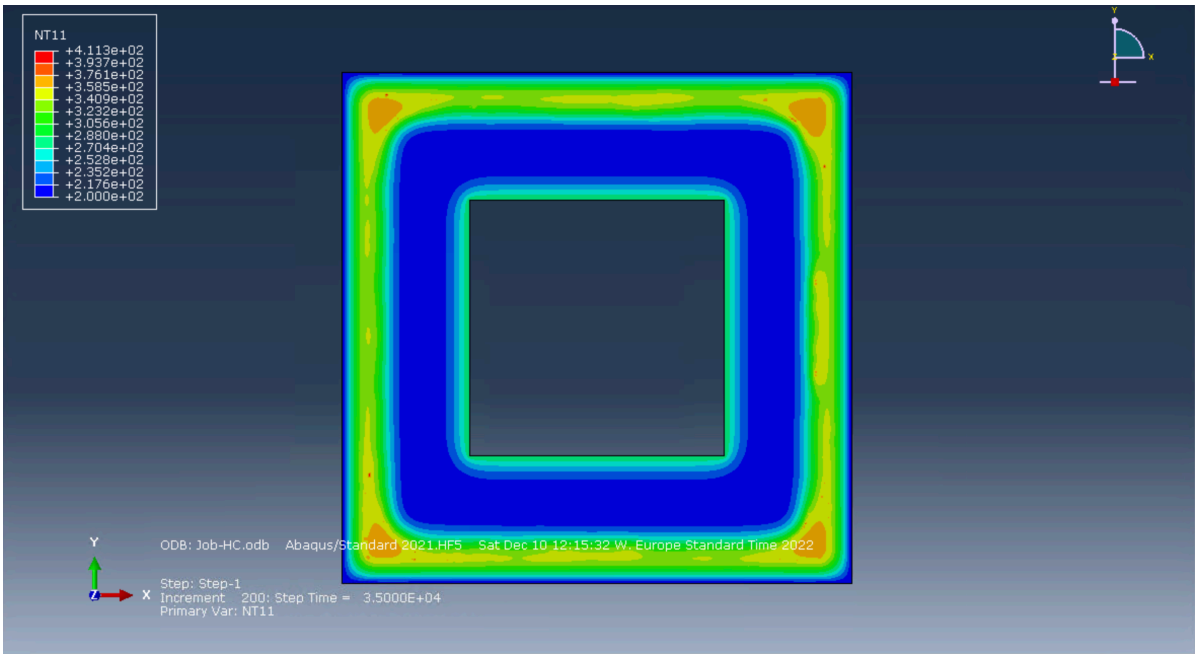

Figure 4.26: Temperature of square MOF-5 walls

UiO-66

Figure 4.27 shows the infeasibility of the square geometry and UiO-66. When the two curves are integrated (area under the curve) and divided by the total simulation time, the thermal power over both boundaries was found to be approximately -63kW/m and 66kW/m for inner and outer boundaries respectively.

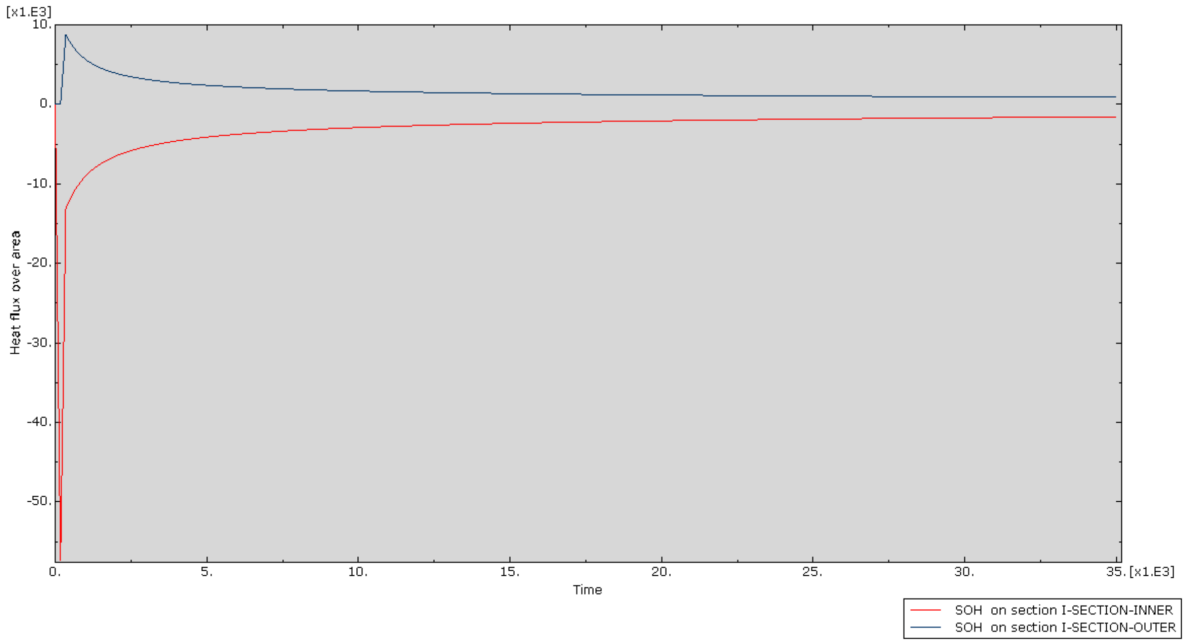

Figure 4.27: Total heat flux leaving the UiO66 from the inner section, and leaving the material from the outer section (positive values are exothermic).

The contours in Figure 4.28 and Figure 4.29 show the main reason why heat is being drained from the room despite over 130kW/m of power being generated by the adsorption process. The average temperatures reach 221, while the average mass fraction was 0.797 (a significant increase from the circular geometry). But once again, heat and CO_2 have not sufficiently diffused through the material to adsorb in sufficient amounts near the inner boundary.

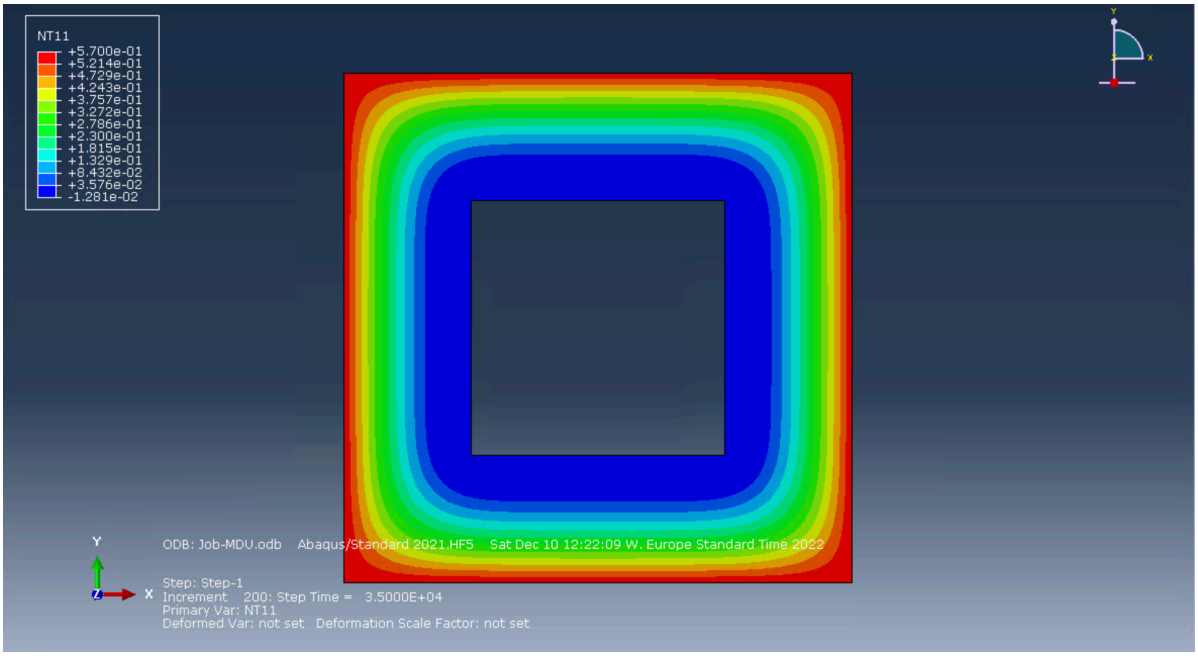

Figure 4.28: Concentration of mobile CO_2 in square UiO-66 walls

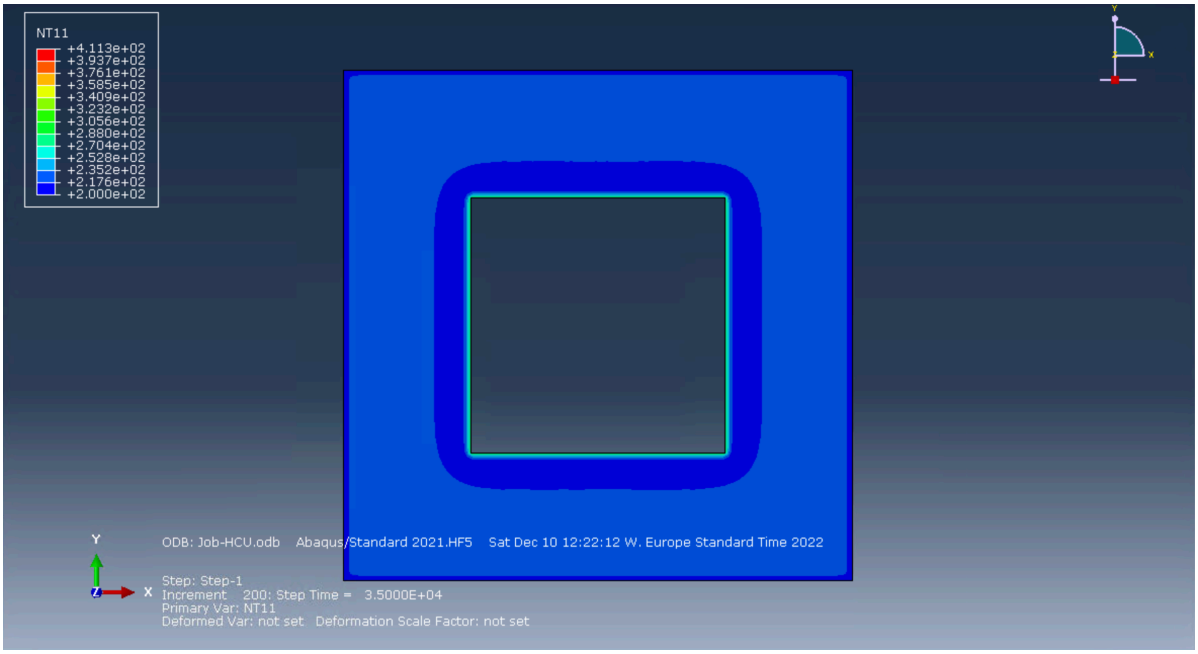

Figure 4.29: Temperature of square UiO-66 walls

Zeolite

Figure 4.30 shows that Zeolite-5A in the square geometric configuration does not meet the requirements needed to keep the room warm. When the two curves are integrated (area under the curve) and divided by the total simulation time, the thermal power over both boundaries was found to be approximately -80kW/m and 263kW/m for inner and outer boundaries respectively.

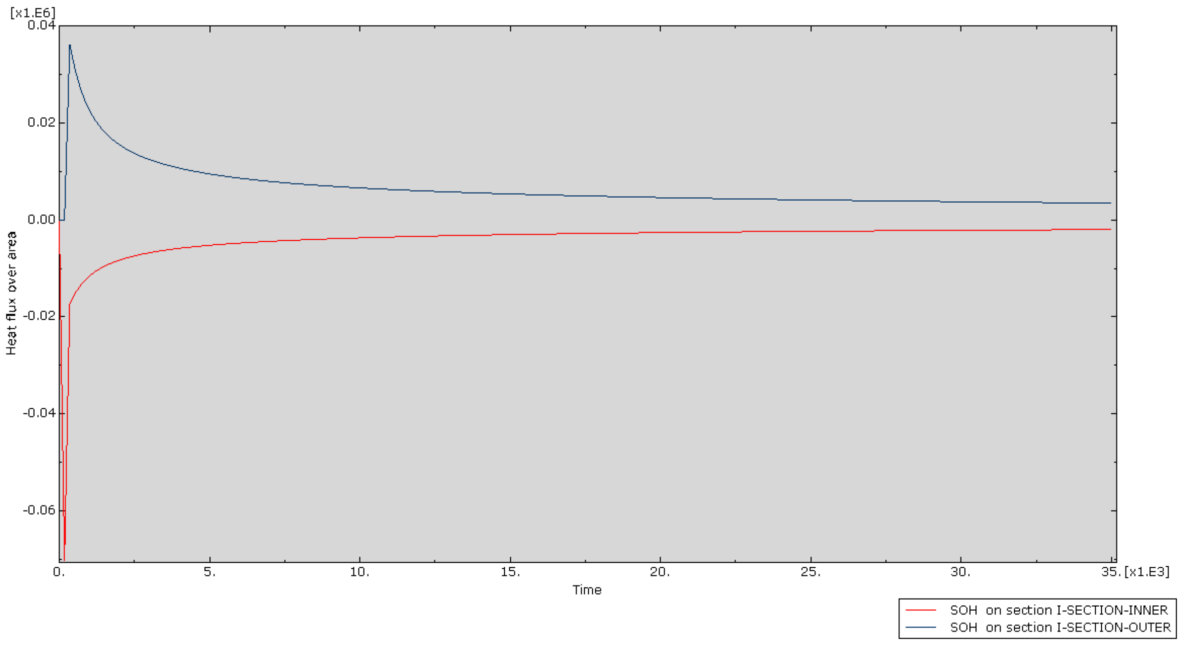

Figure 4.30: Total heat flux leaving the Zeolite-5A from the inner section, and leaving the material from the outer section (positive values are exothermic).

The contours in Figure 4.31 and Figure 4.32 show the main reason why heat is being drained from the room despite over 31kW/m of power being generated by the adsorption process. The average temperatures reaching 239K, while the average mass fraction of was 0.511.

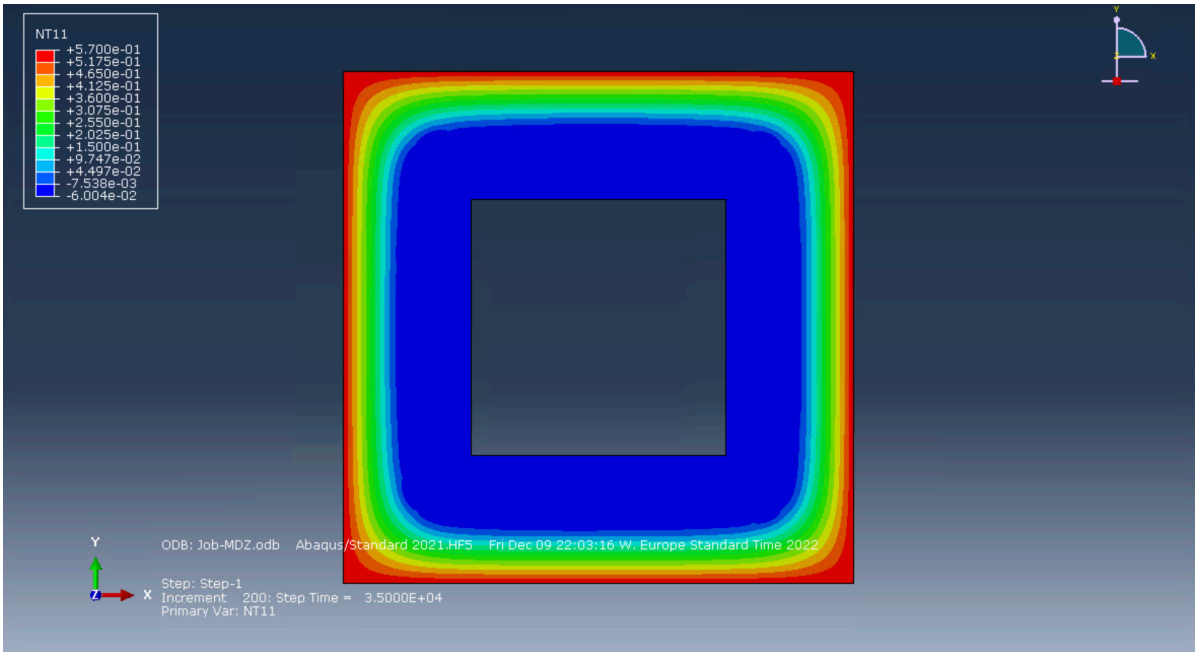

Figure 4.31: Concentration of mobile CO_2 in square Zeolite-5A walls

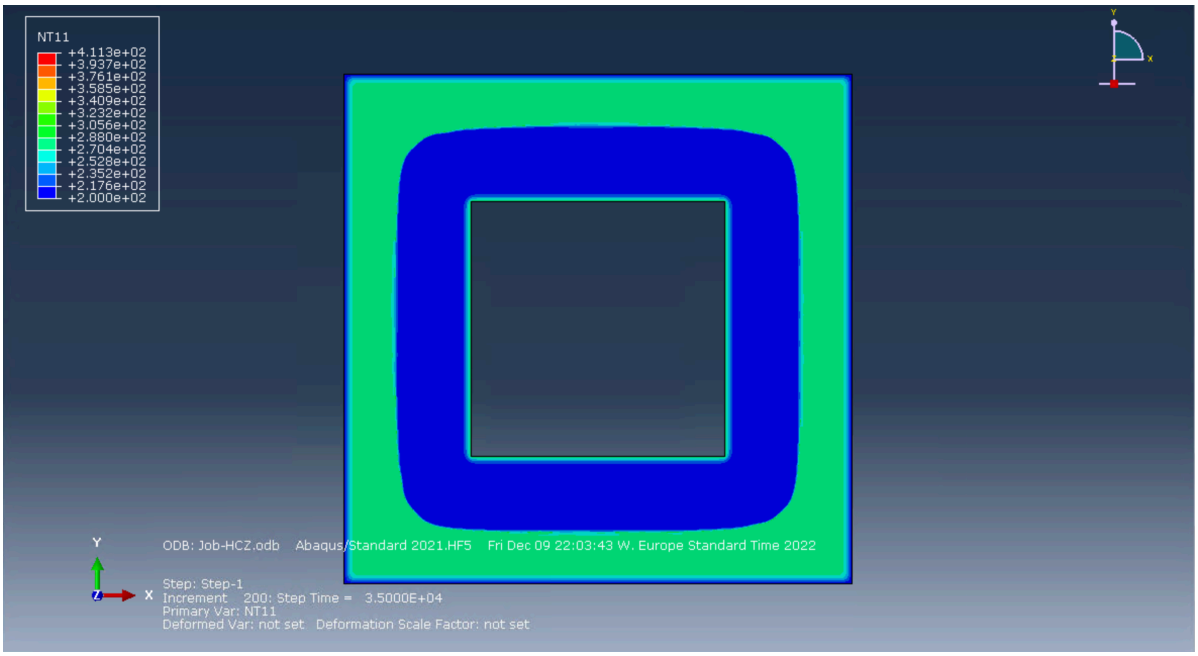

Figure 4.32: Temperature of square Zeolite-5A walls

4.4.5. Desorption

Desorption is the reverse process associated to adsorption. Heat from the ambient atmosphere is used in the endothermic reaction to remove the CO_2 from the material. The kinetics and reaction mechanism was modelled in a similar way as the adsorption process (shown in Equation 3.13 and Equation 3.12):

$$m_{sinkable} = -n \cdot \rho \cdot V_{el} \cdot L \tag{4.1}$$

$$m_{sunk} = -R \cdot n \cdot m_{el} \cdot t_{inc} \tag{4.2}$$

The differences between the adsoprtion and desorption calculations are the negative signs at the start of the equations, and the mass fraction n (instead of $(1-n)$). Both adsorption and desorption behave in the same manner within the DFLUX subroutine, and are therefore the perfect mirror-images of each other. The solution of desorption is driven by the temperature gradient and the CO_2 concentration gradient, in the same way the adsoprtion simulations are. In short, it was found that the desorption simulations were reversed versions of the adsorption simulations seen above and did not provide any further insight into the materials' properties or their feasibility. An example of this can be seen in Figure 4.33.

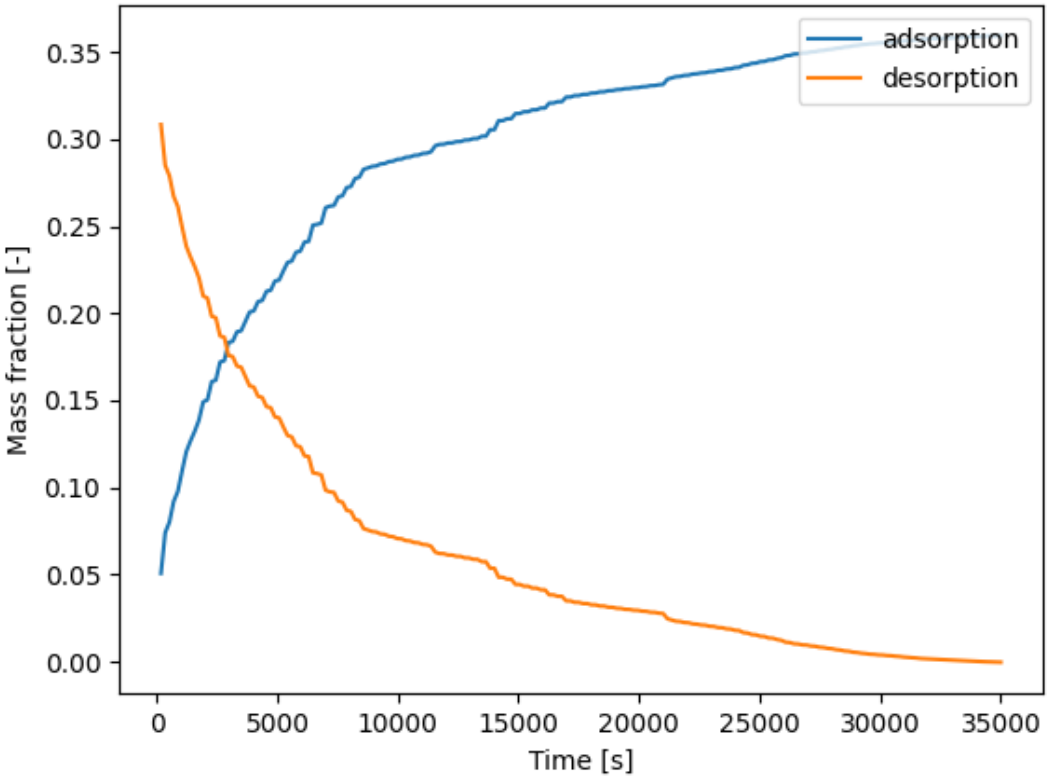

Figure 4.33: Mass fraction of MOF-5 in a square geometry during adsoption (blue) and desorption (orange).

The desorption simulation was run with a starting mass fraction og 0.359 (identical to the mass fraction of the forward adsorption reaction after 35000 seconds). The temperature difference between the inner boundary and outer boundary was kept at 91K; 382K and 291K for the outer and inner boundary respectively. The curves in Figure 4.33 show that the desorption of the material indeed happens in the same manner for all time steps. After inverting the orange curve and comparing its data to the blue curve, the average difference in mass fraction values were found to be approximately 0.00000147.

Furthermore, the desorption occurs during the day, when the temperatures reach approximately 293K (the desired room temperature). During this period, thermal management is not necessary; the sole objective is to remove all the bonded CO_2 from the material, which happens at the same rate as the adsorption reaction and diffusion. The 12 hour window of the desorption to take place is sufficient even with slow mass diffusion coefficients.

4.5. Improving thermal performance

The learning experience from section 4.4 is that the CO_2 diffuses and reacts for hours through the material before getting close enough to supply heat the the Martian home. This means that despite eventually potentially achieving a net zero heat loss to the environment (from the perspective of a

Martian resident), heat is only conducted into the room after 10 hours of time, during which the room had to experience a cooling effect.

One way to achieve this is to change material properties. An obvious solution would be to develop a material like metal-organic frameworks (or zeolite) with lower thermal conductivity and higher mass diffusivity. The results from section 4.4 showed the limitations of of the material, leading to a large volume of space that cools down (due to the external environment) before more CO_2 has permeated and reacted in the material. One can see that UiO-66 and Zeolite-5A have slightly higher diffusion coefficient, which leads to more rapid spikes in heat flow over the inner boundary (human living space). Higher material densities and better diffusion coefficients are the changes that can be made at a material level.

Another way to boost thermal performance is by introducing a new entrance for the CO_2 flow. This is done by creating channels close to the inner boundary, thereby allowing the initial CO_2 to diffuse and react in close proximity to the inner boundary. This is also the initial source of thermal heat generation that acts as a thermal buffer to the outer boundary temperatures. The duration for which the heat source remains close to the inner wall is further amplified by the outer/middle section elements reacting and conducting heat.

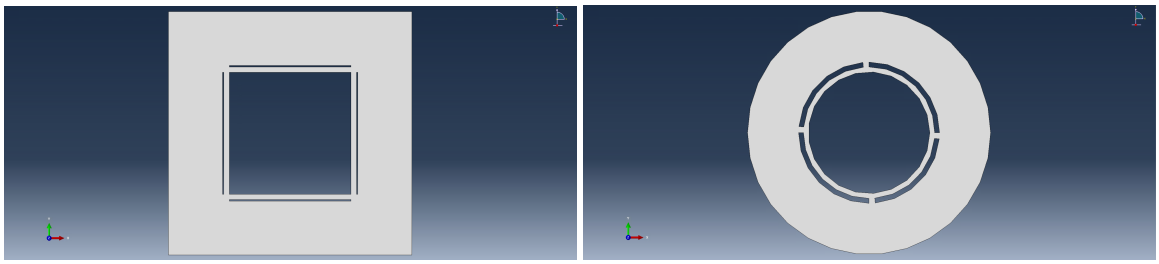

(a) Amended geometry of the square building with CO_2 entrance slots (b) Amended geometry of the circular building with CO_2 entrance slots

Figure 4.34: Adaptation of slotted design for CO_2 introduction close to inner boundary.

As seen in Figure 4.34, the slots were introduced parallel to the inner boundaries, offering the largest relevant surface area. Four slots were created, each with a cutout area of approximately $1.1m^2$. The slots were left unconnected to allow heat and mass transfer between them; the inner rung of material would not be isolated from the rest of the material. The boundary conditions along the 16 faces of the slot geometries were identical to the outer boundary condition Table 4.1: 200K temperature boundary condition and a CO_2 concentration of $0.57kg_{CO_2}/kg_{material}$.

Furthermore, the largest source of heat loss was to the ambient environment through the outer boundary. This could be mitigated by insulating the outer boundary, thereby only allowing the cold CO_2 to enter the material via the slots. This section will focus on four permutations of thermal redesign: slotted square house, slotted circular house, slotted square house with insulated outer boundary, slotted circular house with insulated outer boundary. As before, the other boundary conditions remain identical to the ones stated in Table 4.1, with the exception of the two insulated iterations. Note that due to the thermal advantage and low density, bulk MOF-5 was used for all four iterations.

4.5.1. Slot designs

With the slots added, the model could be run again, this time giving positive results. As seen in Figure 4.35, there is a period of time where heat is flowing from the walls to the room. The point at which the sum (integral under the curve) is zero, is the break-even point for the design. In this case, this occurs after 6.38 hours; it can be surmised that the material is capable of providing passive heating solutions for over six hours.

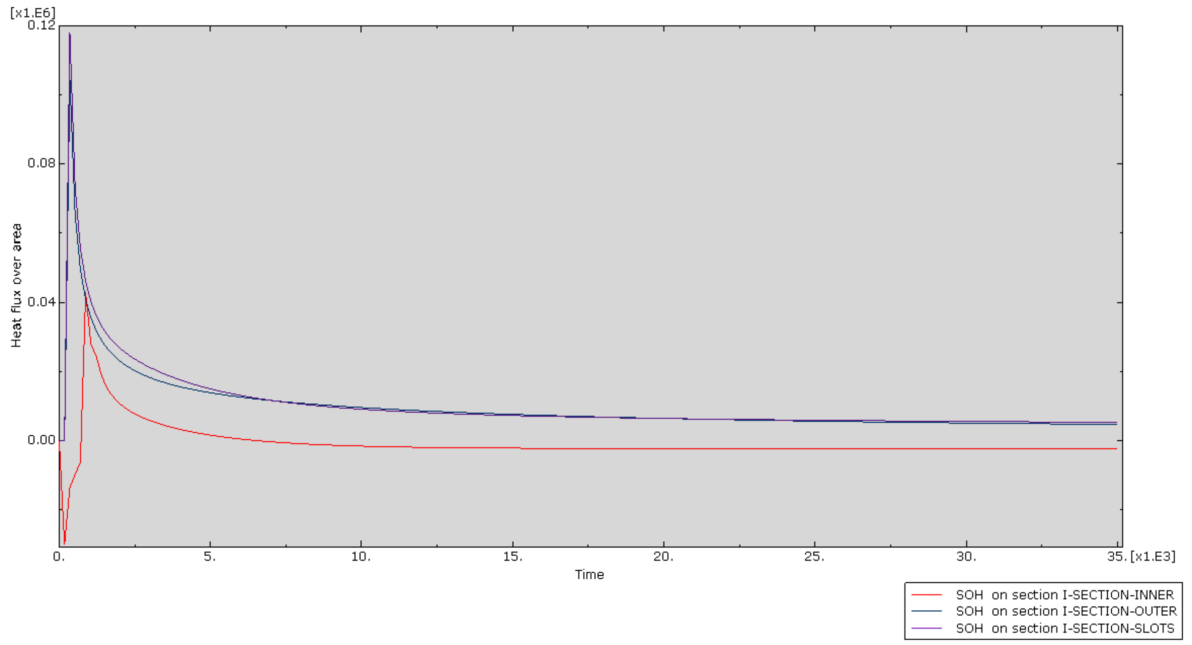

Figure 4.35: Total heat flux leaving the circular slotted geometry from the inner section, outer section, and slot boundaries (positive values are exothermic).

The total heat flux over 35000s seconds for each boundary was -14kW/m, 351kW/m, 388kW/m for inner boundary, outer boundary, and slots respectively. The average temperature reached 283K, with an average mass sunk mass fraction of 0.61. The average temperature is certainly higher than the original circle design, with credit going to 136% increase the mass sunk in the MOF-5. This can be explained in Figure 4.36 and Figure 4.37 below, where the un-reacted portion of the material is a lot smaller and further away from the inner boundary.

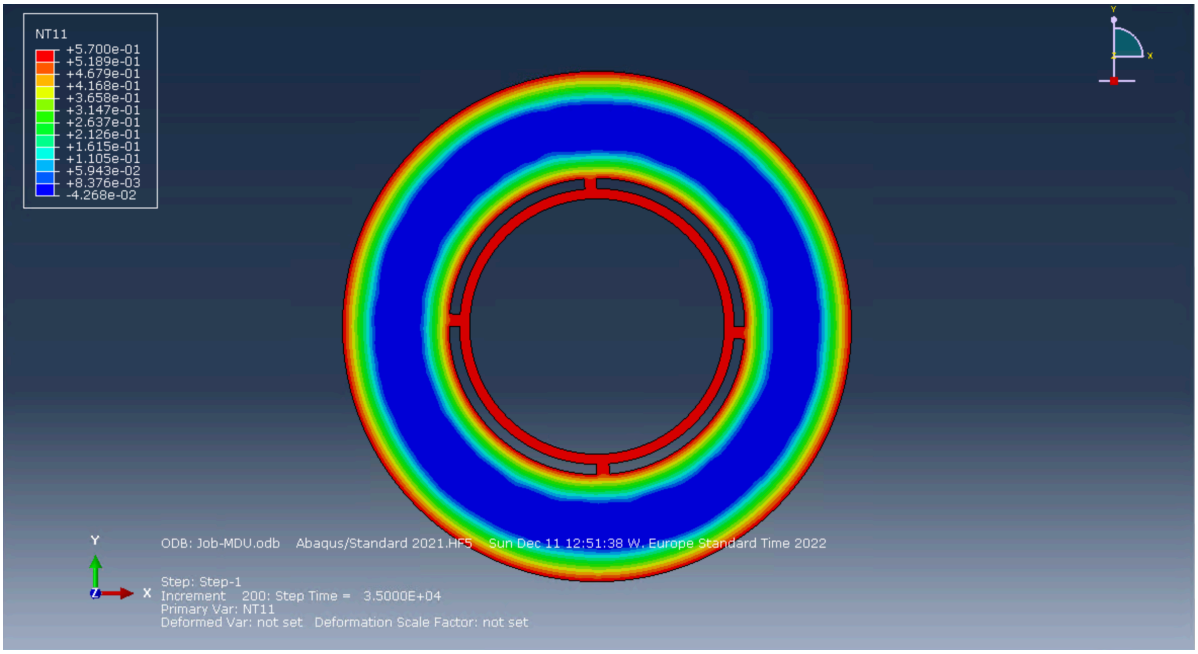

Figure 4.36: Concentration of mobile CO_2 within circular slotted MOF-5 walls.

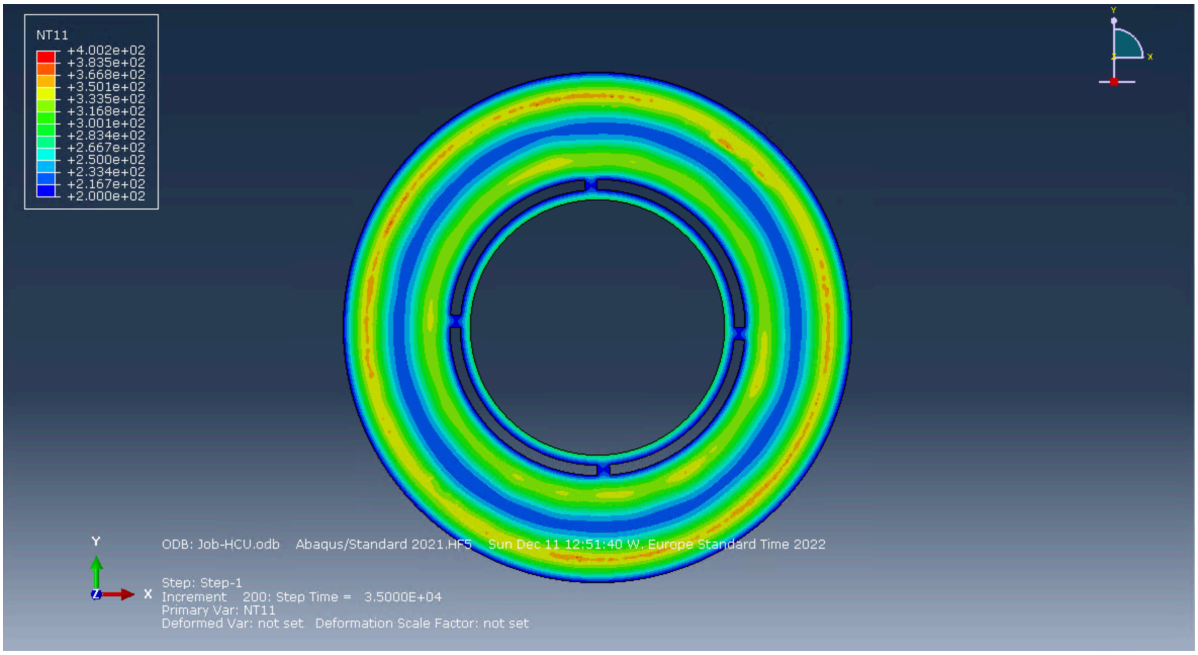

Figure 4.37: Temperature of circular slotted MOF-5 walls

The slotted square design Figure 4.38 also had a period of time where heat flowed from the walls to the room. The break-even point occurs after 6.42 hours; once again proving that the design can be used for Martian thermal solutions.

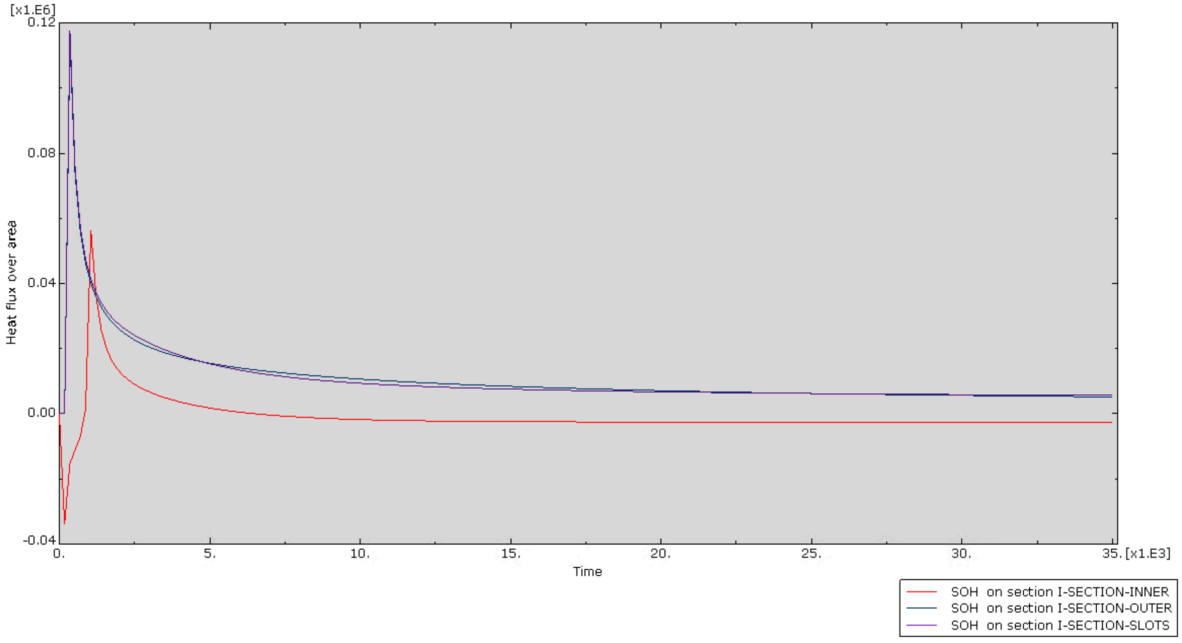

Figure 4.38: Total heat flux leaving the square slotted geometry from the inner section, outer section, and slot boundaries (positive values are exothermic).

The total heat flux over 35000s seconds for each boundary was -18kW/m, 441kW/m, 457kW/m for inner boundary, outer boundary, and slots respectively. The average temperature reached 283K, with an average mass sunk mass fraction of 0.62. The average temperature is certainly higher than the original square design, with credit going to a 72% increase in the mass sunk in the MOF-5. This can be observed in Figure 4.39 and Figure 4.40 below, where the un-reacted portion of the material is a lot

smaller and further away from the inner boundary.

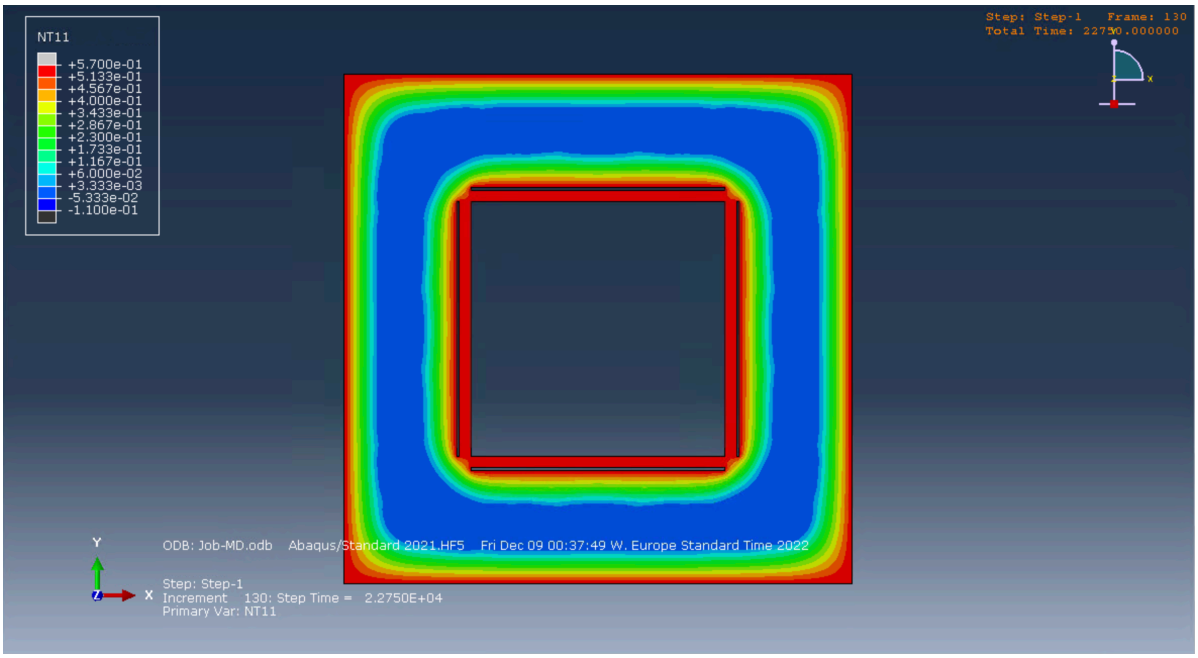

Figure 4.39: Concentration of mobile CO_2 within square slotted MOF-5 walls.

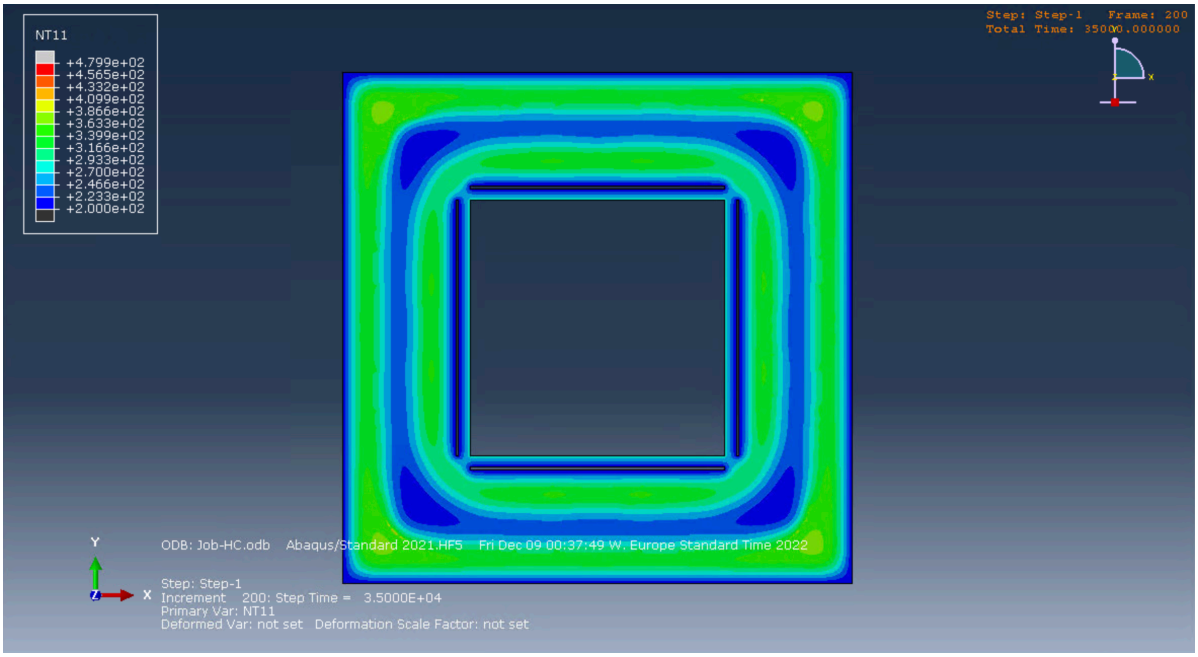

Figure 4.40: Temperature of square slotted MOF-5 walls

4.5.2. Insulated slot designs

The same slot simulations were run, without the thermal and concentration boundary conditions. The only source of CO_2 are the slots, while the slots and inner boundary make up the temperature boundary conditions. Once again, the designs produced positive results. As seen in Figure 4.41, there is a period of time where heat is flowing from the walls to the room. The point at which the sum (integral under the curve) is zero, is the break-even point for the design. In this case, this occurs after 6.38 hours; identical to the original circular slot design.

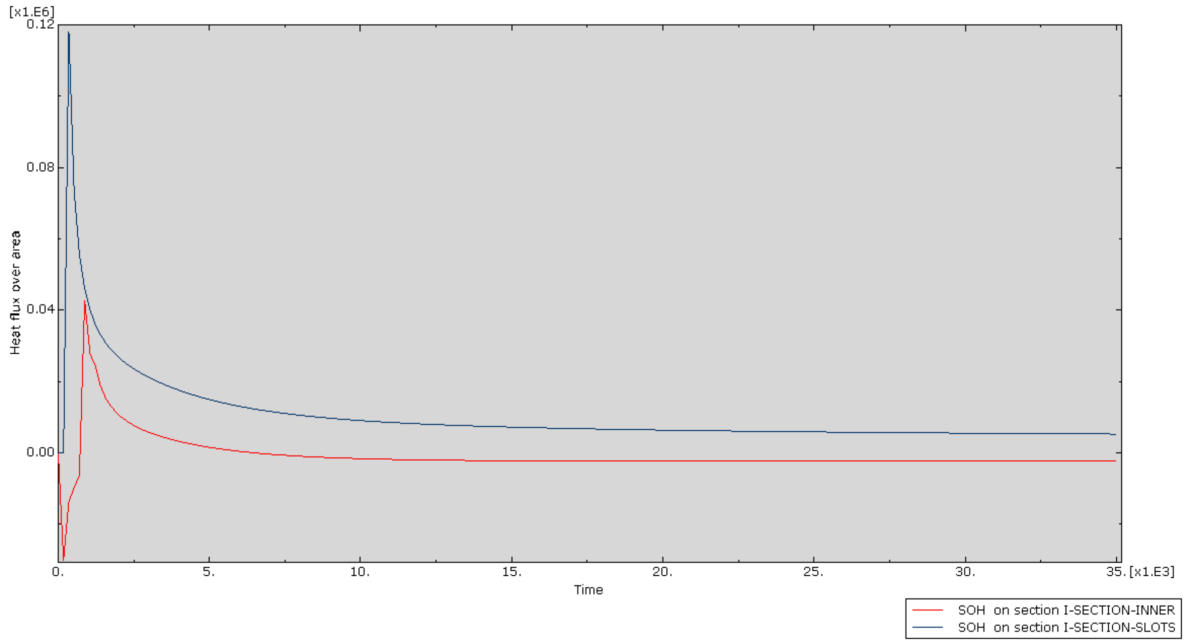

Figure 4.41: Total heat flux leaving the insulated circular slotted geometry from the inner section and slot boundaries (positive values are exothermic).

The total heat flux over 35000s seconds for each boundary was -14kW/m and 388kW/m for inner boundary and slots respectively; this is identical to the original non-insulated circular design. The average temperature reached 241K, with an average mass sunk mass fraction of 0.32. These values are much lower than the original non-insulated circular design, but seem to give the same thermal performance to the Martian room users. This can only mean that the extra mass sunk and higher average temperature occurs at the outer boundary; the insulated outer boundary prevents reactions occurring at the edge of the boundary. Figure 4.42 and Figure 4.43 show that the inner contour regions are almost identical to the non-insulated design, thereby showing that the heat and CO_2 entering from the outer boundary is is negligible.

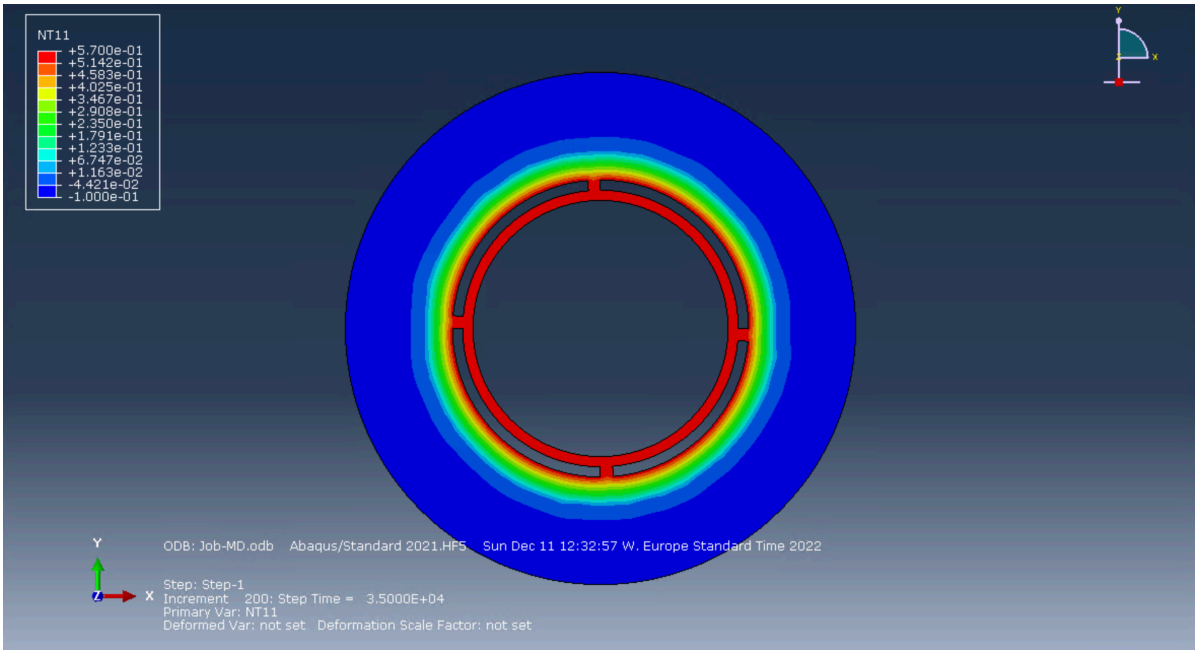

Figure 4.42: Concentration of mobile CO_2 within insulated circular slotted MOF-5 walls.

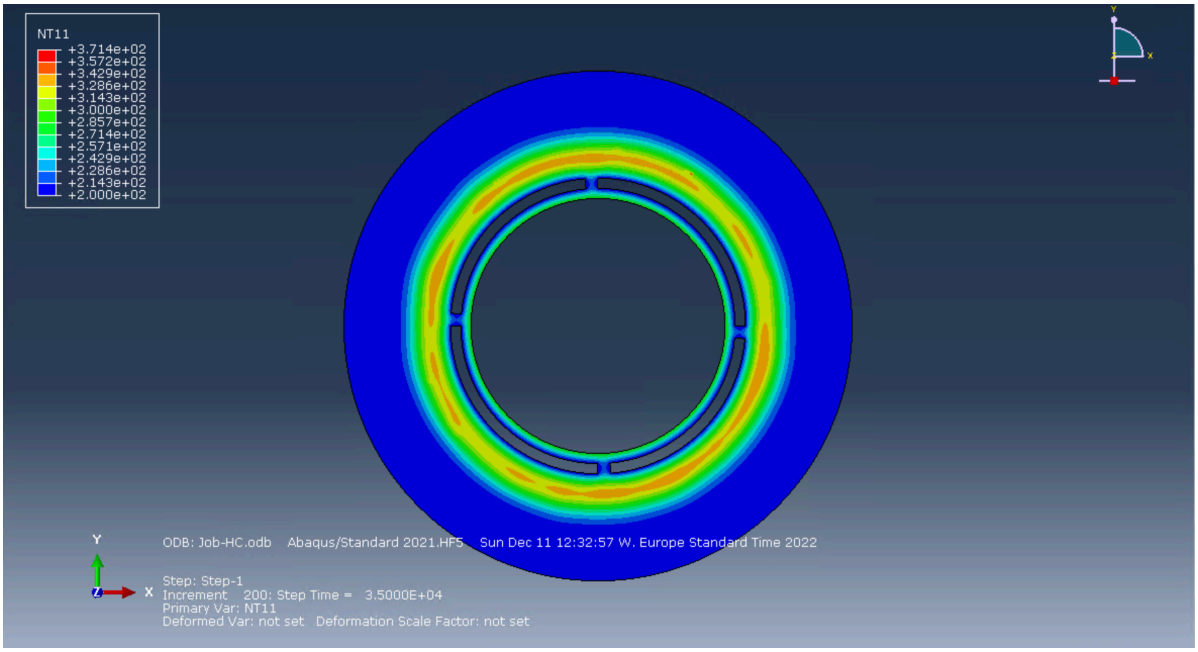

Figure 4.43: Temperature of insulated circular slotted MOF-5 walls

As seen in Figure 4.41, there is a period of time where heat is flowing from the walls to the room. The point at which the sum (integral under the curve) is zero, is the break-even point for the design. In this case, this occurs after 6.42 hours; identical to the original square slot design.

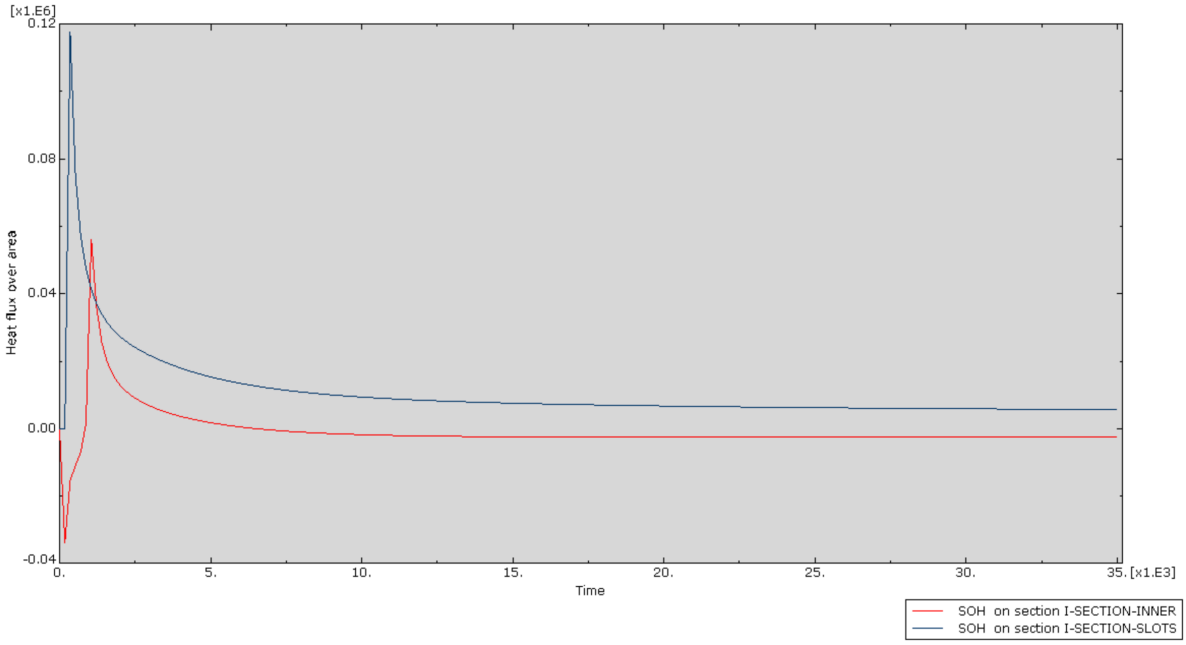

Figure 4.44: Total heat flux leaving the insulated square slotted geometry from the inner section and slot boundaries (positive values are exothermic).

The total heat flux over 35000s seconds for each boundary was -18kW/m and 457kW/m for inner boundary and slots respectively; this is identical to the original non-insulated square design. The average temperature reached 234K, with an average mass sunk mass fraction of 0.27. These values are much lower than the original non-insulated square design, but seem to give the same thermal performance to the Martian room users. The extra mass sunk and higher average temperature occurs

at the outer boundary; the insulated outer boundary prevents reactions occurring at the edge of the boundary. Figure 4.45 and Figure 4.46 show that the inner contour regions are almost identical to the non-insulated design, thereby showing that the heat and CO_2 entering from the outer boundary is is negligible.

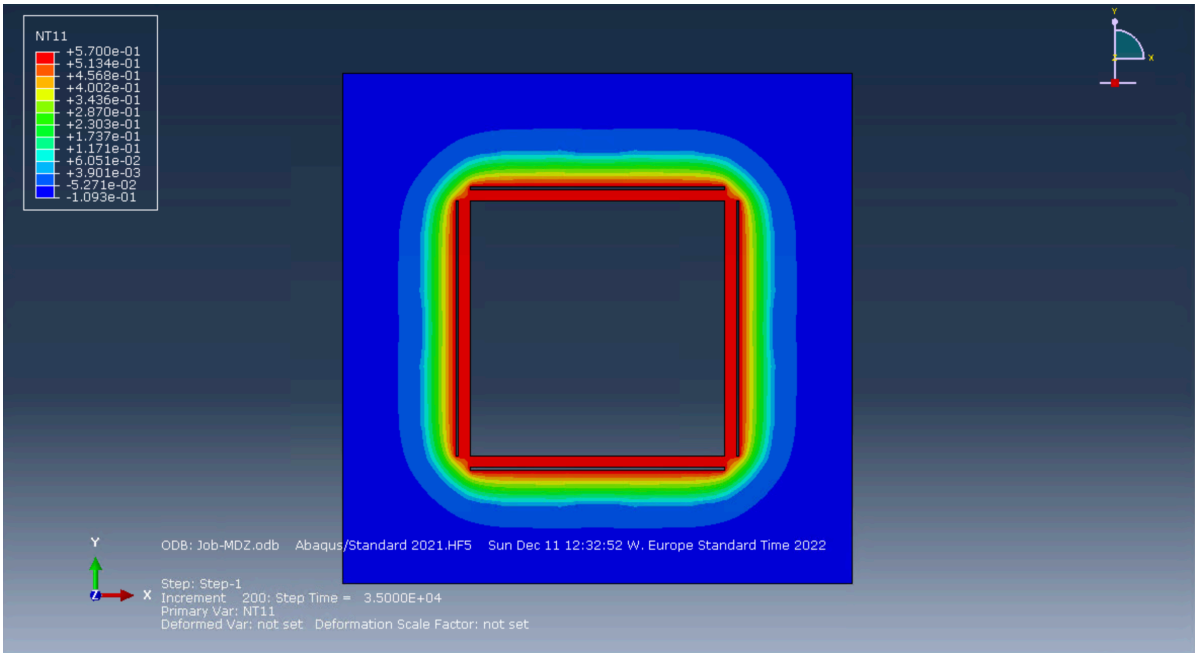

Figure 4.45: Concentration of mobile CO_2 within insulated square slotted MOF-5 walls.

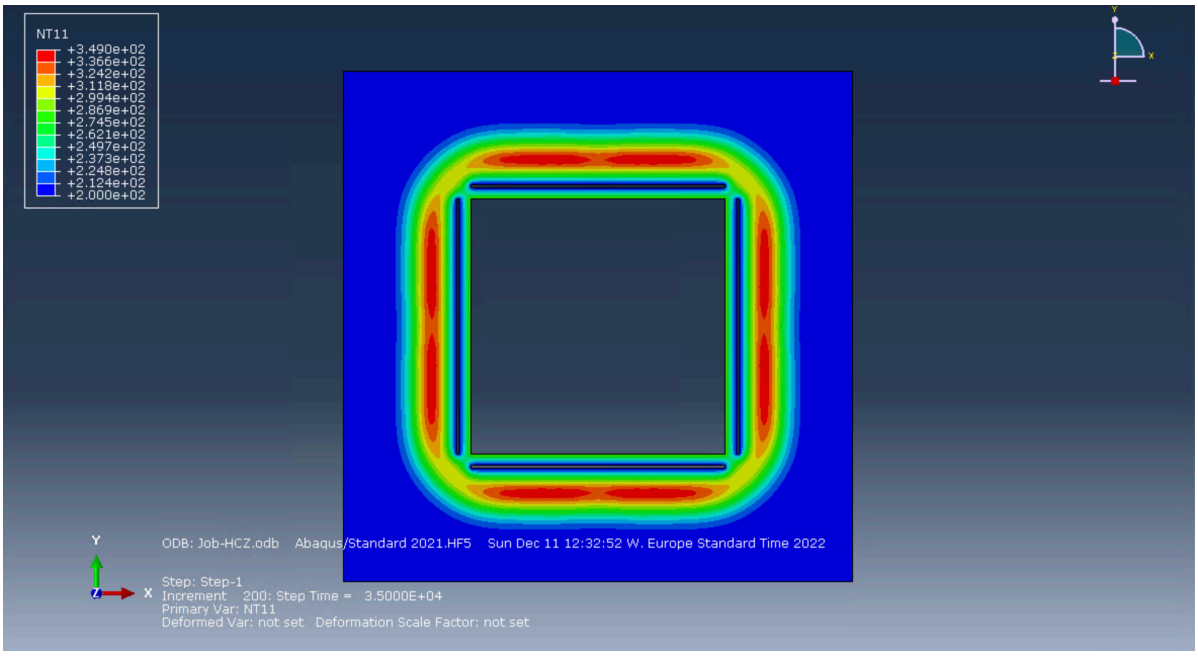

Figure 4.46: Temperature of insulated square slotted MOF-5 walls

4.5.3. 24 hour cycle

The slots gave the inner boundary proximity to the reactions that were taking place in the material. The real test of the material as an autonomous climate control solution is to simulate the material over a full day. Much like Earth, a regular day on Mars is approximately 24 hours, but with an ambient temperature

range of 200-293K. The lowest temperature periods are at midnight, with the highs at noon. The model assumes a linear increase in temperature between the highs and lows. The results can be seen in the figure below. The trigger temperature was at 245K, fixed as a material property, which occurred approximately at the quarter day points (6 and 18 hrs).

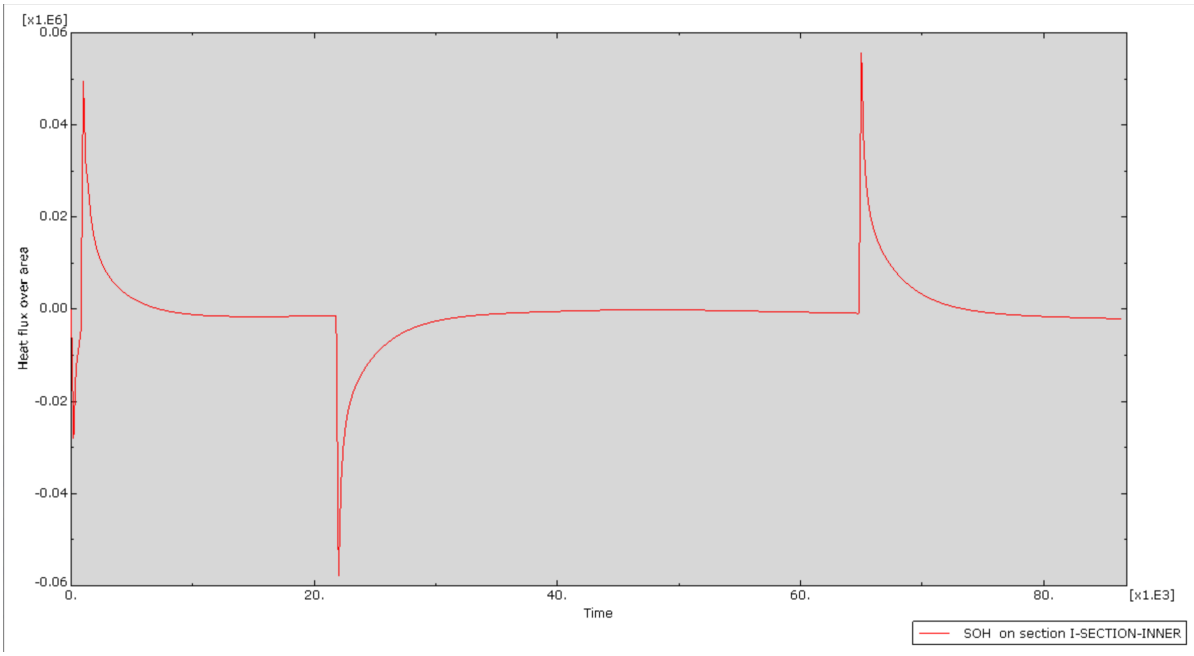

Figure 4.47: Total heat flux leaving the insulated circular slotted geometry from the inner section (positive values are exothermic).

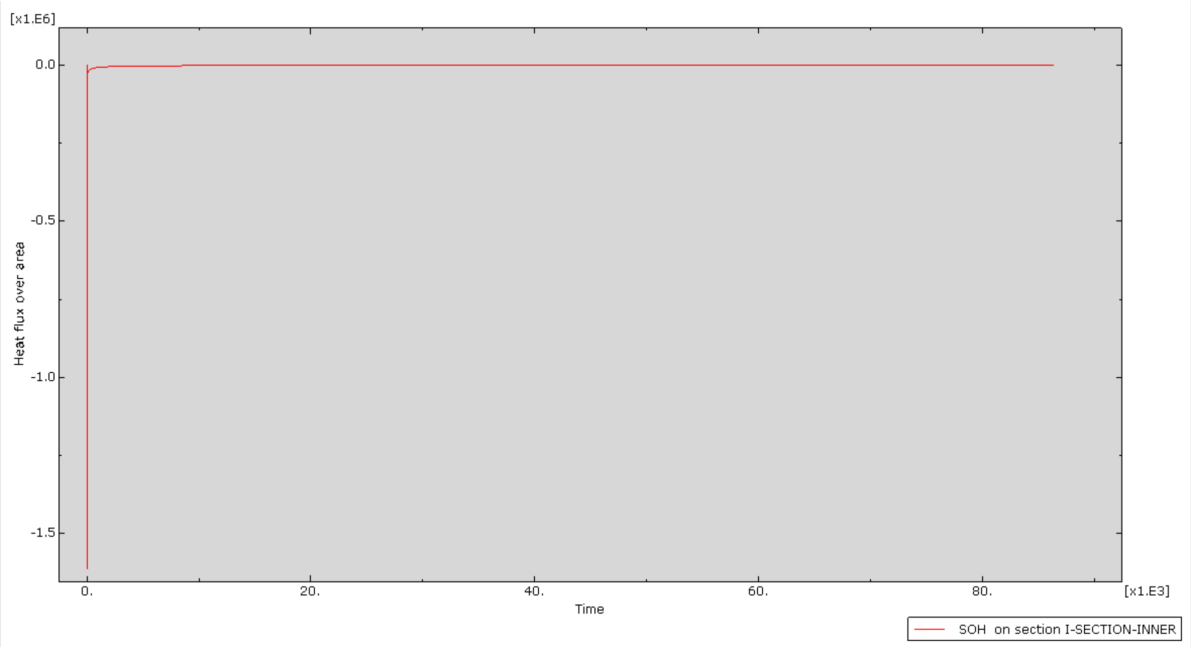

Figure 4.48: Total heat flux leaving the circular slotted geometry from the inner section with concrete walls (positive values are exothermic).

The total heat flux leaving the inner room (as seen in Figure 4.47) over the 24 hour period is approximately -13kW/m. Concurrently, a Martian building built entirely with concrete saps over 528kW/m from the Martian inner room. This value indicates that the MOF-5 eliminates the need of 97.6% of fuel other-

wise needed to heat the Martian homes. Note that the thermal conductivity, specific heat capacity, and density for the concrete walls were 2.25 W/(m K), 880 J/(kg K), and 2400 kg/m^2. A home constructed with pure MOF-5, which undergoes no adsoprtion reactions with CO_2, sees a heat flux of -151kW/m. This once again shows that the adorption reactions are vital to the Martian buildings, providing up to 91.4% of the energy needed to heat the Martian homes built with MOF-5.

Over the course of a day, the material only provides a positive heat flux into the room for the first 6.2 hours of the day. As seen in Figure 4.47, there are three spikes in heat flux. The first spike happens at the beginning, when sufficient CO_2 has permeated through the material and adsorb. Over time, the rate of adsorption reduces as the CO_2 takes a longer to permeate through the material to the outer unreacted material regions.

The second spike (with a negative amplitude) occurs at approximately the six hour mark when the trigger temperature is met. This is when the material no longer adsorbs CO_2 and releases heat; the material releases the stored/bonded CO_2 in an endothermic reaction (heat is taken from the environment and the room). The material becomes extremely cold, while dispelling the CO_2, thereby drawing heat from the inner room. Once again, the heat flux plateaus between the second and third spike as the material is slowly desorbed and CO_2 is released to the ambient environment.

Finally the third spike at approximately the 18-hour mark is when the ambient temperature drops below the trigger temperature and the adsorption process can begin again. Heat is released when CO_2 reacts with the material. Note that the second and third spikes have a significantly steeper gradient due to the availability of free mobile CO_2 in the material.

Is is evident that MOF-5 is capable of supplying approximately 12.5 hours of heat to the room during the day. Approximately 2-3 hours during the peak temperature (noon) requires no heating or cooling. This leaves approximately 7.5 hours of temperature control that the MOF is unable to provide. The metal-organic framework material relies too much on the bulk material regions closest to the inner room, thereby negating the rest of the material's contributions due to the slow mass diffusion coefficient. A way to prevent the second large spike during desorption is to insulate (cut-off) the home from the material during the desorption process. This means that the material would not be able to provide heat to the room during the hours 6-10 and 14-18, but would be a viable solution for the rest of the hours in the day.

4.6. Validation

Verification of the model was completed in section 4.2, to ensure that the model operates in the way it was intended. However, the validation of the model is needed to assess the validity of the computation done in the DFLUX subroutine, and the amount of heat generated by the model. The conventional validation method is to compare the model with experimental data. This is particularly challenging due to the lack of testing done for adsorption in bulk metal-organic framework materials. The few sources available were used to calibrate the rate of reaction (as seen in section 4.1. A comparison between this model and experimental data would therefore have to be done with any material that adsorbs a gas in an exothermic reaction. The paper used for comparison was the experimental measurement of CO_2 adsorption of MOF-74, written by *Long et al.* [28]. Much like the sources used for calibration, the rate of uptake was used to confirm the validity of the results.

The model parameters are summarised in Table 4.2 below. The reference paper showcased the experimental data in the form of a CO_2 uptake graph, which can be seen in Figure 4.49. Note that the maximum mobile concentration was assumed to be 0.57 and the rate of reaction ratio was set to 0.2. For validation purposes, the standard MOF-74 (the blue line (s)) was used.

Table 4.2: MOF-74 material chanracteristics used for validation

Parameter	Value	Units
Material dimensions	0.00125	m
Mass density	1220	kg/m^3
Mass diffusivity	0.0000127	m^2/s
CO_2 uptake	0.35	$kg_{CO_2}/kg_{material}$
Thermal conductivity	0.143	W/(m K)
Adsorption enthalpy	7.72×10^5	J/kg_{CO_2}
Specific heat capacity	722	J/(kg K)
Temperature of MOF-74	298	K
Temperature of CO_2	298	K
Maximum mobile concentration	0.57	$kg_{CO_2}/kg_{material}$
Rate of reaction ratio	0.2	-m

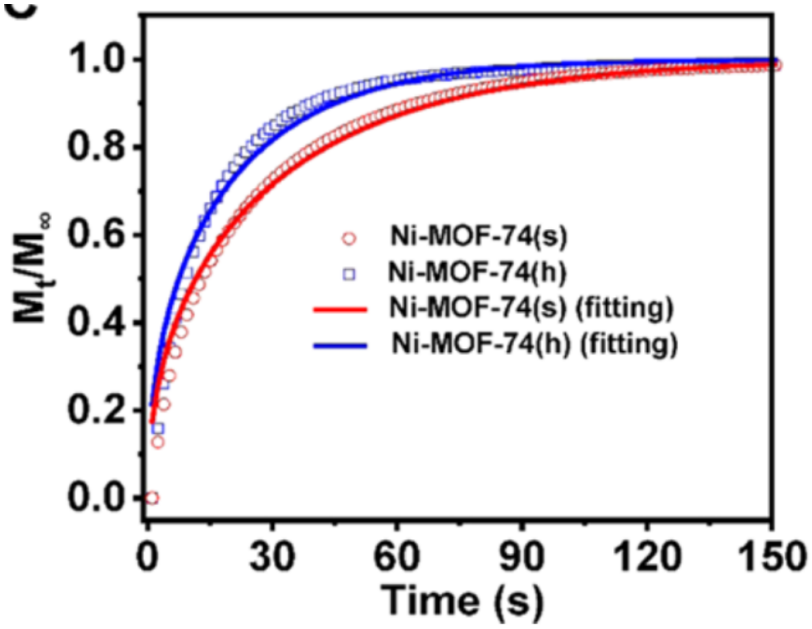

Figure 4.49: CO_2 uptake of MOF-74 crystals over a span of 150 seconds [28].

A square geometry of size 0.00125x0.00125m was created in ABAQUS and assigned the aforementioned material parameters. The temperature and concentration boundary conditions were applied equally at all four edges of the geometry. The model was run for 150 seconds at a time increment of 3 seconds, after which the uptake results were plotted (as seen in Figure 4.50)

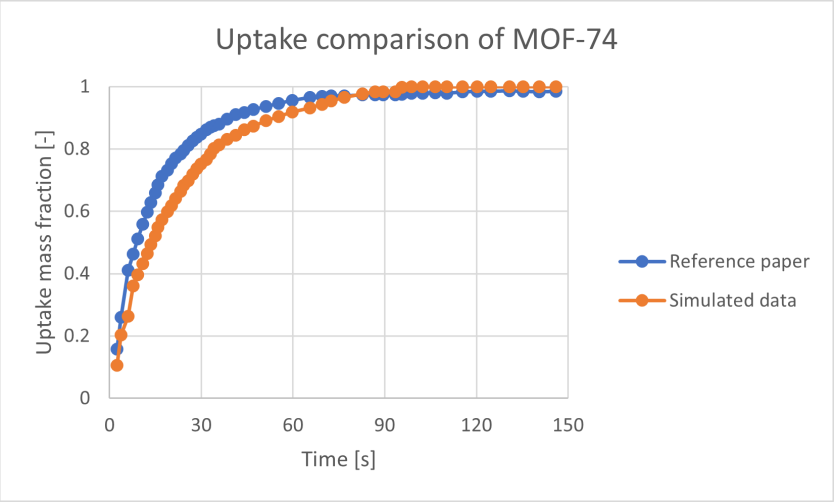

Figure 4.50: CO_2 uptake of MOF-74 crystals over a span of 150 seconds; (blue) reference paper valules, (orange) model output.

The general shape of the curve is extremely similar, especially the transition region between 15-60 seconds. The average percentage difference between the reference values and the ABAQUS simulations were 8.9%.The simulation accurately shows the uptake despite the enormous difference in spatial dimensions, and is considered validated. The temperature of the material was not compared for two reasons: lack of data in the research paper, and trivial calculations. The experimental values kept the temperature controlled at 298K, which was enforced by the fluid entering the system. With such small crystals, the heat was conducted out extremely quickly. Another reason why the temperature fields were not inspected was due to the fact that the heat conduction simulation is derived from the mass diffusion simulation. The mass diffusion simulation calculates the mass sunk, the sink term, the mass fractions, and the rates of reaction; conversely, the heat conduction equation simply multiplies the mass sunk with the enthalpy of reaction. It is for this reason that the validation process, using only the CO_2 uptake values, was chosen.

4.7. Current state and next steps

The three materials have the possibility to provide passive heating to Martian homes for just over six hours during the night (approximately 12 hours during a full day); the materials show the potential to be a long-term solution for Martian infrastructure, but require further design iterations. A large portion of the material was left unreacted even after 35,000 seconds (over 9.72 hours). As a thermal battery, this meant that only 25-70% of the battery was used to heat the room, leaving the rest of the battery as surplus. This is the primary issue with the current design, and is prevalent even with the slotted iterations made.

4.7.1. Material modifications

The materials used, while promising, were the primary cause of inefficient thermal storage. The thermal storage of the material can be enhanced by changing the thermal conductivity and mass diffusivity coefficients. High thermal conductivity was initially sought after, for its ability to distribute heat effectively. This is less important when coupled with a mass diffusion simulation, as the driving forces for heat conduction are the chemical reactions that take place after mass has diffused through the material. On the contrary, it was found that the heat conduction was occurring too quickly, allowing the heat generated by the reactions to be cooled by the environment before more CO_2 has diffused to the site. It is for this reason that lowering the thermal conductivity a couple orders of magnitude (taking it closer to the value of the mass diffusion equation) would prolong the heat flow into the room before being lost to the environment.

Mass diffusivity plays an enormous role in the loading of the material. As seen in all simulations (unmodified, slots, and insulated) the middle section of the walls all had very low temperature and mass concentration. This is because the CO_2 permeated through the materials too slowly, thereby reacting

with the material regions closest to the boundaries. The current mass diffusivities are in the range of 1.1-1.7x10^{-5} m^2/s; with the material area used in the designs and a single slot CO_2 source, it could theoretically take 1400 hours for mass to diffuse to every single part of the material. Lowering the mass diffusivity by an order of magnitude would help with hastening the speed of reactions and loading of the material.

Further research into material degradation is key to deciding the efficacy of metal-organic framework materials in Mars. As previously mentioned, MOF-5 has perfect reversible reactions, which acts like a virgin material after each sorption cycle. Degradation was investigated over 10-209 cycles in most academic sources; with he material requiring hundreds of cycles per year, degradation analysis (and thermal fatigue analysis) are necessary.

In addition to thermal and chemical degradation occurring due to the sorption reactions, the material must also be tested for solar radiation degradation. The Martian atmospheric is significantly weaker than Earth's, leading to significantly more ionising radiation and cosmic radiation observed on the planet's surface. Aside from the lack of oxygen and cold temperatures, this is one of the key challenges humans face on Mars. The radiation could potentially interfere with the chemical reaction and degrade the material, thereby limiting the reversible nature of the sorption reactions.

4.7.2. Geometric modifications

Geometry modifications showed the most promise, after applying slots near the inner boundary, for extracting the full material potential. Further geometric modifications, such as slotted channels in the midsection (like radiator fins) could help increase the uptake of CO_2 of the material. Another geometric modification would be to fully insulate the outer boundary and reduce the thickness of the wall, thereby eliminating the surplus of unused material. This would not lead to a longer heating duration, like the other proposed modifications, but eliminates redundant weight (an important factor to consider for Martian expeditions).

4.7.3. Advanced boundary conditions

The current boundary conditions for the living spaces in the building are constant temperature boundary conditions. This boundary condition ensures a constant temperature of 291K in the room, regardless of the heat flux entering or leaving the system. The results evaluated the cumulative heat flux entering the system. For the scope of this thesis, the constant temperature boundary condition was sufficient.

A variable temperature boundary condition at the inner boundary would add to the accuracy of the model. As of now, the model assumes an infinitely large ”reservoir” of air within the room to keep the temperature at 291K at all times. Having a convective boundary condition at the wall, with a variable inner room temperature, would help create a more accurate representation of the living conditions of Martian humans. This would involve having a coupled computational fluid dynamic simulation that assesses the heat transfer phenomenon between the walls/radiator and the air in the room.

4.7.4. System modification

Insulated boundaries

In addition to insulating certain boundaries, adding more active control over the system can greatly enhance the performance of the material. This thesis investigated the passive uptake of CO_2 due to the scarcity of technology and humans on Mars; a low-maintenance system with next to zero moving parts, leads to fewer points of failure. Nevertheless, actively controlled sub-systems can expand on the efficiencies of the material.

The first type of sub-system would be a sealant. After the desorption of the material during the day, the material must stay pristine and unloaded until the heating process needs to begin. For this paper, a simple trigger temperature was used to signify the turning of day to night. However in reality, its an equilibrium reaction; there will be a small about of CO_2 that might still be reacting at the inlet boundary regions. This is when a sealant in needed, to prevent CO_2 from entering the material until the heating process is required again.

Forced CO_2 transfer

A fluid pump is another sub-system that would benefit the materials. If the material properties cannot be changed, then having a fluid pump to force CO_2 diffusion through the material using a pressure

gradient, would accelerate the loading of the material. This is especially useful when a sudden burst of heating is needed, requiring a much faster heating response time from the material.

This would have to be coupled to a heat exchanger, the third kind of sub-system. The CO_2 that flows through the material due to the pump would be in surplus to the amount of CO_2 the material is capable of adsorbing. The mobile CO_2 would also get heated by the material while it flows out of the system, thereby removing more thermal energy from the material. A heat exchanger would recover the heat lost of the fluid and use it for the Martian home.

Alternative use: boiler

The MOF is currently used as a construction material and as a passive heating solution for the Martian buildings. The effects of the reactions in the MOF are directly felt by the residents in the house because of how close to the MOF the people actually are. Another way the MOF material can be used for Martian building heating solutions is as a boiler. In most Dutch homes, the boiler used for central heating heats the heat transfer fluid (i.e., water). The water is heated by burning natural gas (the most common method) or using electricity, while the heat is transferred from the water to the household via radiators.

The water-radiator process can remain unchanged on Mars, but the boiler can be replaced by MOFs. This process allows the MOF to directly transfer the heat to the water, but prevents the heat to be radiated from the walls (an unpleasant user experience). Furthermore, the central heating system can facilitate two ”boilers” in one large loop. During the 12-15 hours for which the MOF material can sufficiently provide heat, the second traditional boiler can be turned off and disconnected from the line. During the other others hours when the MOF cannot be the sole heating solution (e.g., during the MOF desorption period), the MOF can be disconnected from the heating line and the traditional boiler can provide consistent heating to the building.

This involves the MOF used in a thermal battery capacity rather than an all-in-one heating solution. At peak charge (i.e., a material with no CO_2 bonded), the MOF can be relied upon to provide thermal energy to the Martian households. During the re-charging process (i.e., desorption of the CO_2 from the material), the MOF must be disconnected from the home. Much like an empty powerbank, it must be disconnected from the device it is charging, otherwise it would lead to a charge drain from the electrical devices. A method to couple and decouple the MOF from the central heating loop is key to making the MOF work as a thermal battery/boiler.

5

Conclusion

Energy scarcity is not just a future possibility on Earth, but a likely possibility in the near future during inter-planetary travel/colonisation. The idea of space colonisation is currently infeasible due to a variety of reasons, one of them being a stable source of energy. Thermal energy storage is a material-based storage mechanism that stores energy intrinsically. Conventional storage methods (i.e. batteries) are expensive to manufacture, have low efficiencies, and are difficult to transport. Batteries are not likely the sole solution to the global energy demand, due to their use of rare earth metals and toxicity. Thus, the need for diversifying energy storage methods is so important. Thermal energy storage offers the possibility of controlling internal environments, without the use of conventional fuels, which is a necessary step towards colonising/inhabiting Mars to some extent.

The adsorption processes used by metal-organic framework materials (and zeolite) are reversible chemical reactions. The materials have have high thermal storage density, but cannot be used right out of the box as building material. Three materials were investigated (MOF-5, UiO-66, and Zeolite-5A), each with their own unique material properties and adsorption kinetics. An ABAQUS model was created, using two parallel ABAQUS simulations, to simulate the adsorption characteristics at a macro-scale. This model explored the feasibility of using metal-organ framework materials as bulk wall material. Each of the two parallel simulations had individually operating user-subroutines that amended the governing diffusion/conduction equations and customised the solution accordingly. The simulations stored the temperature and mass fraction fields respectively, thereby allowing the other simulation to cross-read data between simulations.

The materials themselves had imperfect characteristics, namely the thermal conductivity and the mass diffusivity. Unaltered metal-organic framework materials in the wall are all but entirely wasted and do not offer a heating solution to the Martian buildings. After making some geometric enhancements, such as adding inlet slots near the centre of the material, the material was able to provide 12-15 hours of required heat as the sole thermal energy provider of the Martian building. Previously developed models used active solutions to maximise the amount of CO_2 stored in the material, which makes this research unique in its passive process. When compared to an equivalent building made out of conventional construction concrete and un-reactive MOF-5 (both needed external heat sources), the reactive MOF-5 walls supplied approximately 97.6% and 91.4% of the necessary thermal energy to the home respectively. Despite not entirely achieving the goal of creating a singular passive thermal control material solution for Martian buildings, MOF-5 is able to reduce the required energy significantly. It opens up the possibilities for potentially using metal-organic framework materials in buildings on Earth to aid in the global energy crisis and emissions crisis.

The future of Martian thermal management must continue to look at metal-organic framework materials if Martian colonisation is to be a realistic goal. The biggest obstacle is the synthesis of the material and transportation to Mars, which would also be an issue for conventional fossil fuel solutions. The passive thermal management is the key to the technology being viable, which is what this report has deemed largely possible. Further uses of metal-organic frmework materials could be to store fuels (such as hydrogen or methane) via the adsorption process, while transported to Mars, and then used as a thermal battery once the fuels have been unloaded in Mars. Chemical sorption reactions have

the possibility to make real waves in the world of sustainable energy, and metal-organic framework materials could be the forerunners in the global development drive.

Bibliography

[1] I. Sarbu and C. Sebarchievici, “Thermal Energy Storage,” in *Solar Heating and Cooling Systems*, Elsevier, Jan. 2017, pp. 99–138. DOI: 10.1016/B978-0-12-811662-3.00004-9. [Online]. Available: https://linkinghub.elsevier.com/retrieve/pii/B9780128116623000049.

[2] L. F. Cabeza, I. Martorell, L. Miró, A. I. Fernández, and C. Barreneche, “Introduction to thermal energy storage (TES) systems,” in *Advances in Thermal Energy Storage Systems: Methods and Applications*, Elsevier Inc., Jan. 2015, pp. 1–28, ISBN: 9781782420965. DOI: 10.1533/9781782420965.1.

[3] K. Pielichowska and K. Pielichowski, “Phase change materials for thermal energy storage,” *Progress in Materials Science*, vol. 65, pp. 67–123, Aug. 2014, ISSN: 00796425. DOI: 10.1016/j.pmatsci.2014.03.005.

[4] A. Al-Ahmed, A. Sarı, M. A. J. Mazumder, G. Hekimoğlu, F. A. Al-Sulaiman, and Inamuddin, “Thermal energy storage and thermal conductivity properties of Octadecanol-MWCNT composite PCMs as promising organic heat storage materials,” *Scientific Reports*, vol. 10, no. 1, pp. 1–15, Dec. 2020, ISSN: 20452322. DOI: 10.1038/s41598-020-64149-3. [Online]. Available: https://doi.org/10.1038/s41598-020-64149-3.

[5] A. Sharma, V. V. Tyagi, C. R. Chen, and D. Buddhi, “Review on thermal energy storage with phase change materials and applications,” *Renewable and Sustainable Energy Reviews*, vol. 13, no. 2, pp. 318–345, Feb. 2009, ISSN: 13640321. DOI: 10.1016/j.rser.2007.10.005.

[6] H. Kerskes, “Thermochemical Energy Storage,” in *Storing Energy: With Special Reference to Renewable Energy Sources*, Elsevier Inc., Apr. 2016, pp. 345–372, ISBN: 9780128034408. DOI: 10.1016/B978-0-12-803440-8.00017-8.

[7] I. Fujii, K. Tsuchiya, M. Higano, and J. Yamada, “Studies of an energy storage system by use of the reversible chemical reaction: CaO + H2O □ Ca(OH)2,” *Solar Energy*, vol. 34, no. 4-5, pp. 367–377, Jan. 1985, ISSN: 0038092X. DOI: 10.1016/0038-092X(85)90049-0.

[8] S. Kalaiselvam and R. Parameshwaran, “Thermochemical Energy Storage,” in *Thermal Energy Storage Technologies for Sustainability*, Elsevier, Jan. 2014, pp. 127–144. DOI: 10.1016/B978-0-12-417291-3.00006-2. [Online]. Available: https://linkinghub.elsevier.com/retrieve/pii/B9780124172913000062.

[9] M. Mohammadi, S. R. Shadizadeh, A. K. Manshad, and A. H. Mohammadi, “Experimental study of the relationship between porosity and surface area of carbonate reservoir rocks,” *Journal of Petroleum Exploration and Production Technology 2020 10:5*, vol. 10, no. 5, pp. 1817–1834, Feb. 2020, ISSN: 2190-0566. DOI: 10.1007/S13202-020-00838-Z. [Online]. Available: https://link.springer.com/article/10.1007/s13202-020-00838-z.

[10] D. Jaehnig, R. Hausner, W. Wagner, and C. Isaksson, “THERMO-CHEMICAL STORAGE FOR SOLAR SPACE HEATING IN A SINGLE-FAMILY HOUSE,” AEE - Institute for Sustainable Technologies, Gleisdorf, Tech. Rep. [Online]. Available: https://www.aee-intec.at/0uploads/dateien336.pdf.

[11] M. Berger, *What is a MOF (metal organic framework)?* DOI: 10.1038/46248. [Online]. Available: https://www.nanowerk.com/mof-metal-organic-framework.php.

[12] H. Li, M. Eddaoudi, M. O’Keeffe, and O. M. Yaghi, “Design and synthesis of an exceptionally stable and highly porous metal- organic framework,” *Nature*, vol. 402, no. 6759, pp. 276–279, Nov. 1999, ISSN: 00280836. DOI: 10.1038/46248. [Online]. Available: www.nature.com.

[13] S. E. M. Elhenawy, M. Khraisheh, F. Almomani, and G. Walker, *Metal-organic frameworks as a platform for CO2 capture and chemical processes: Adsorption, membrane separation, catalytic-conversion, and electrochemical reduction of CO2*, Nov. 2020. DOI: 10.3390/catal10111293.

[14] W. Kukulka, K. Cendrowski, B. Michalkiewicz, and E. Mijowska, “MOF-5 derived carbon as material for CO 2 absorption,” *RSC Advances*, vol. 9, no. 32, pp. 18 527–18 537, Jun. 2019, ISSN: 20462069. DOI: 10.1039/C9RA01786K. [Online]. Available: https://pubs-rsc-org.tudelft.idm.oclc.org/en/content/articlehtml/2019/ra/c9ra01786k%20https://pubs-rsc-org.tudelft.idm.oclc.org/en/content/articlelanding/2019/ra/c9ra01786k.

[15] Z. Zhao, Z. Li, and Y. S. Lin, “Adsorption and diffusion of carbon dioxide on metal-organic framework (MOF-5),” *Industrial and Engineering Chemistry Research*, vol. 48, no. 22, pp. 10 015–10 020, 2009, ISSN: 08885885. DOI: 10.1021/IE900665F/ASSET/IMAGES/LARGE/IE-2009-00665F{_}0009.JPEG. [Online]. Available: https://pubs-acs-org.tudelft.idm.oclc.org/doi/full/10.1021/ie900665f.

[16] D. Wu, J. J. Gassensmith, D. Gouvê, *et al.*, “Direct Calorimetric Measurement of Enthalpy of Adsorption of Carbon Dioxide on CD-MOF-2, a Green Metal−Organic Framework,” 2013. DOI: 10.1021/ja402315d.

[17] J. Huang, X. Xia, X. Hu, S. Li, and K. Liu, “A general method for measuring the thermal conductivity of MOF crystals,” *International Journal of Heat and Mass Transfer*, vol. 138, pp. 11–16, Aug. 2019, ISSN: 0017-9310. DOI: 10.1016/J.IJHEATMASSTRANSFER.2019.04.018.

[18] V. N. Le, T. K. Vo, K. S. Yoo, and J. Kim, “Enhanced CO2 adsorption performance on amino-defective UiO-66 with 4-amino benzoic acid as the defective linker,” *Separation and Purification Technology*, vol. 274, p. 119 079, Nov. 2021, ISSN: 1383-5866. DOI: 10.1016/J.SEPPUR.2021.119079.

[19] M. Duquesne, J. Toutain, A. Sempey, S. Ginestet, and E. Palomo Del Barrio, “Modeling of a non-linear thermochemical energy storage by adsorption on zeolites,” *Applied Thermal Engineering*, vol. 71, no. 1, pp. 469–480, Oct. 2014, ISSN: 1359-4311. DOI: 10.1016/J.APPLTHERMALENG.2014.07.002. [Online]. Available: https://www-sciencedirect-com.tudelft.idm.oclc.org/science/article/pii/S135943111400550X?via%3Dihub.

[20] Q. Wang and S. Tang, “Energy storage analysis of R125 in UIO-66 and MOF-5 nanoparticles: A molecular simulation study,” *Open Chemistry*, vol. 17, no. 1, pp. 229–234, Jan. 2019, ISSN: 23915420. DOI: 10.1515/CHEM-2019-0026/MACHINEREADABLECITATION/RIS. [Online]. Available: https://www-degruyter-com.tudelft.idm.oclc.org/document/doi/10.1515/chem-2019-0026/html?lang=en.

[21] J. Wieme, S. Vandenbrande, A. Lamaire, V. Kapil, L. Vanduyfhuys, and V. Van Speybroeck, “Thermal Engineering of Metal-Organic Frameworks for Adsorption Applications: A Molecular Simulation Perspective,” *ACS Applied Materials and Interfaces*, vol. 11, no. 42, pp. 38 697–38 707, Oct. 2019, ISSN: 19448252. DOI: 10.1021/ACSAMI.9B12533/ASSET/IMAGES/MEDIUM/AM9B12533{_}M009.GIF. [Online]. Available: https://pubs-acs-org.tudelft.idm.oclc.org/doi/full/10.1021/acsami.9b12533.

[22] T. S. Hille, S. Turteltaub, and A. S. Suiker, “Oxide growth and damage evolution in thermal barrier coatings,” *Engineering Fracture Mechanics*, vol. 78, no. 10, pp. 2139–2152, Jul. 2011, ISSN: 00137944. DOI: 10.1016/j.engfracmech.2011.04.003.

[23] M. R. Armstrong, B. Shan, Z. Cheng, D. Wang, J. Liu, and B. Mu, “Adsorption and diffusion of carbon dioxide on the metal-organic framework CuBTB,” *Chemical Engineering Science*, vol. 167, pp. 10–17, Aug. 2017, ISSN: 0009-2509. DOI: 10.1016/J.CES.2017.03.049.

[24] F. Salles, D. I. Kolokolov, H. Jobic, *et al.*, “Adsorption and diffusion of H2 in the MOF type systems MIL-47(V) and mil-53(cr): A combination of microcalorimetry and qens experiments with molecular simulations,” *Journal of Physical Chemistry C*, vol. 113, no. 18, pp. 7802–7812, May 2009, ISSN: 19327455. DOI: 10.1021/JP811190G.

[25] S. Zhuang, R. Cheng, and J. Wang, “Adsorption of diclofenac from aqueous solution using UiO-66-type metal-organic frameworks,” *Chemical Engineering Journal*, vol. 359, pp. 354–362, Mar. 2019, ISSN: 1385-8947. DOI: 10.1016/J.CEJ.2018.11.150.

[26] M. Antonio-Abdu Sami and V. Eliseo, “Performance analysis of a pressure swing adsorption unit in removing biogas impurities using zeolite 13X,” in *MATEC Web of Conferences*, vol. 192, EDP Sciences, Aug. 2018. DOI: 10.1051/matecconf/201819203029.

[27] Ajay Harish, *What is Convergence in Finite Element Analysis?* Nov. 2022.

[28] C. Wu, L. Y. Chou, L. Long, *et al.*, “Structural Control of Uniform MOF-74 Microcrystals for the Study of Adsorption Kinetics,” *ACS Applied Materials and Interfaces*, vol. 11, no. 39, pp. 35 820–35 826, Oct. 2019, ISSN: 19448252. DOI: 10.1021/acsami.9b13965.